Title
Turning Autophagy On and Off through the Class III PI-3 Kinase

Author
Young, Lindsey Nicole

Publication Date
2019

Peer reviewed|Thesis/dissertation

Turning Autophagy On and Off through the Class III PI-3 Kinase

By

Lindsey N. Young

A dissertation submitted in partial satisfaction

Of the requirements for the degree of

Doctor of Philosophy

In

Molecular and Cellular Biology

In the Graduate Division

Of the

University of California, Berkeley

Committee in charge:

Professor James H. Hurley, Chair

Professor Eva Nogales

Professor Roberto Zoncu

Professor James Olzmann

Spring 2019

ABSTRACT

Turning Autophagy On and Off through the Class III PI-3 Kinase

By

Lindsey N. Young

Doctor of Philosophy in Molecular and Cellular Biology
University of California, Berkeley

Professor James H. Hurley, Chair

Autophagy (self-eating) is an essential process for cellular self-renewal. The class III phosphatidylinositol 3-kinase complex I (PI3KC3-C1) is central to autophagy initiation. The V-shaped architecture of the four-subunit version of PI3KC3-C1 consists of VPS34, VPS15, BECN1, and ATG14. Chapter 2 shows that a putative fifth subunit, NRBF2, is a tightly-bound component of the complex that profoundly affects its activity and architecture. NRBF2 enhances the lipid kinase activity of the catalytic subunit, VPS34. We used hydrogen-deuterium exchange coupled to mass spectrometry (HDX-MS) and negative stain electron microscopy to map NRBF2 to the base of the V-shaped complex. NRBF2 interacts primarily with the N-termini of ATG14 and BECN1 and activates VPS34 through its N-terminal MIT domain.

The ability of NRBF2 to activate the lipid kinase of VPS34 via an allosteric mechanism had not been determined. Chapter 3 shows precisely where the MIT domain of NRBF2 binds to PI3KC3-C1, that one copy of the MIT domain is insufficient for activation, and that full activation requires a second copy of the MIT domain. Dimeric NRBF2 cinches around the conformational flexible catalytic arm of the complex and stabilizes the lipid kinase domain of VPS34 and the putative kinase domain of VPS15.

Membrane targeting of the BECN1-containing class III PI 3-kinase (PI3KC3) complexes is pivotal to the regulation of autophagy. Chapter 4 describes how a cryptic membrane binding site within BECN1 was identified. First, the interaction of PI3KC3 complex II and its ubiquitously expressed inhibitor, Rubicon, was mapped to the first β sheet of the BECN1 BARA domain by hydrogen-deuterium exchange and cryo-EM. The interaction determinants were confirmed in cell-based assays of PI3KC3 activity and autophagy. These data suggested that BARA β sheet-1 unfolds to directly engage the membrane. This mechanism was confirmed using protein engineering, giant unilamellar vesicle assays, and molecular simulations. Using this mechanism, a BECN1 β sheet-1-derived peptide activates both PI3KC3 complexes I and II, while HIV-1 Nef inhibits complex II. These data reveal how BECN1 switches on and off PI3KC3 binding to membranes. The observations explain how PI3KC3 inhibition by Rubicon, activation by autophagy-inducing BECN1 peptides, and inhibition by HIV-1 Nef, are mediated by the switchable ability of the BECN1 BARA domain to partially unfold and insert into membrane.

ACKNOWLEDGEMENTS

To my mentor, Jim Hurley, thank you for everything. Thank you for creating a wonderful research environment. You have a unique “let’s try ” approach to very challenging projects, it’s been incredible to see what your lab, my colleagues have accomplished over the years. I am so grateful for every opportunity, big and small. Thank you for all the encouragement, for being genuinely excited about my progress, for all your thoughtful advice and scientific input. My post-doc search was tough in part because you are a lot of measure up to! I will miss you.

In addition, thank you to all the faculty that have assisted me along the way, especially my thesis committee, Dr. Eva Nogales, Dr. Roberto Zoncu, and Dr. James Olzmann.

To everyone I have overlapped with in the lab, wow, you are superstars to me. To Dr. Kyle Morris, you are one of a kind, thank you for creating our EM environment. I wouldn’t be where I am without you, all your advice, support, and encouragement when I needed it helped immensely. To Dr. Chunmei Chang, your transition from cell biologist to biochemical reconstitution expert has been truly inspiring. I really enjoyed working with you and hearing your “can-do” attitude day-after-day. To Felix Goerdeler, thank you for helping to revive the NRBF2 project. I had no idea we would get so much done or become such close friends in such a short time period. I miss you all the time! To Dr. Xuefeng (Snow) Ren, you are everything, an Olympian-level structural biologist, the Bobby Fischer of AP biology, the Mother Theresa of our lab, keeping it running and helping everyone when needed. To all my labmates, thanks for being supportive, for creating a fun place to do science. To the EM community and the Bay Area Cryo-EM consortium- Dr. Eva Nogales, Dr. Dan Toso, Dr. Patricia Grob, thank you for all your contributions to the EM community at Berkeley.

To my friends, Rosalie, Elise, Laura, Shion, Charlotte, thank you for the camping trips, the climbing adventures, the time spent at beer gardens, yoga classes, dinner parties, three Thanksgivings, it truly kept me sane. To my college roommate, Kate, I could not have been luckier that you moved to the Bay Area, you are such a grounding force, the time I spend in your company is always too short. Tess, Linh, and Tao, I love your little family, thank you for calling me up whenever you are free. To my friends who scattered around the world, Kaitlin, Kathleen, Agne, Alice, Alyson, Nina, Sarah, Erinn, I love you all to pieces.

To Max Goodman, grad school has been so much more fun since you came into my life. I sometimes still can’t believe how much care, kindness, and love you possess. There are a few days I want to relive in my life, a lot of them are moments of scientific discovery, but many of them are days we spent rock climbing, bike riding, hiking, cooking outside, skiing, scuba diving, traveling. You make me so happy, I love you.

To my parents, thank you for being proud of me. I promise I will always make time to tell you what I do all day.

DEDICATION

To all the public institutions I have attended, particularly New College of Florida, I am so grateful. I think my career in basic research is entirely attributed to all the independent studies and research opportunities I was offered.

TABLE OF CONTENTS

List of Figures

Chapter 1
Mechanisms of Autophagy Initiation

These contents here were published in a review article by Hurley, J. H. and Young, L. N. (2017) *Mechanisms of autophagy initiation*, *Annual Review of Biochemistry*. doi: 10.1146/annurev-biochem-061516-044820.

1 Mechanisms of Autophagy Initiation

1.1 Summary

Autophagy is the process of cellular self-eating by a double-membrane organelle, the autophagosome. A range of signaling processes converge on two protein complexes to initiate autophagy: the ULK1 protein kinase complex and the PI3KC3-C1 lipid kinase complex. Some 90% of the mass of these large protein complexes consists on non-catalytic domains and subunits, and the ULK1 complex has been shown to have essential non-catalytic activities. Structural studies of these complexes have shed increasing light on the regulation of their catalytic and non-catalytic activities in autophagy initiation. The autophagosome is thought to nucleate from vesicles containing the integral membrane protein Atg9, COPII vesicles, and possibly other sources. In the wake of reconstitution and superresolution imaging studies, we are beginning to understand how the ULK1 and PI3KC3-C1 complexes might coordinate the nucleation and fusion of Atg9 and COPII vesicles at the start of autophagosome biogenesis.

1.2 Introduction

Macroautophagy (hereafter “autophagy”) is the main mechanism used by eukaryotic cells to degrade cargoes that are larger than individual proteins. It is also the main mechanism for eukaryotic cells to replenish pools of biosynthetic precursors and energy sources by recycling cytosolic contents during starvation. Both the process of autophagy and its machinery is c*onserved from yeasts (S. c*erevisiae and S. pombe) to mammals (Bento et al. 2016). Autophagy can be either selective or non-selective (“bulk”). Selective autophagy removes and recycles harmful or simply unneeded materials from the cell. These include protein aggregates, damaged mitochondria, unneeded peroxisomes, excess ribosomes, ER and endosomes, lipid droplets, and intracellular pathogens (Shaid et al. 2013; Zaffagnini and Martens 2016). Failure to control the accumulation of any of these types of materials can lead to disease in humans.

Bulk autophagy is triggered by starvation, and is critical for maintaining a cellular supply of lipids, amino acids, carbohydrates, and nucleotides. Selective and bulk autophagy are triggered by different signals. Yet, these diverse signals are thought to funnel into a single pathway that initiates the mechanical events and membrane remodeling needed to create the autophagosome. This review will focus on the conserved and common events that initiate both selective and bulk autophagy. Far more is known about bulk autophagy initiation. The review will focus on data from bulk autophagy research, with the understanding that most of the findings probably apply to selective autophagy.

Autophagy is initiated in yeast at a punctate structure called the Phagophore Assembly Site (K. Suzuki et al. 2001) (PAS, also sometimes called the pre-autophagosomal structure. In mammals, initiation is associated with an endoplasmic reticulum (ER) subdomain enriched for the lipid phosphatidylinositol 3-phosphate (PI(3)P), known as the omegasome. From its inception at the PAS or omegasome (Axe et al. 2008), the phagophore elongates into a cup-shaped structure and begins to engulf cellular material. The membrane supply for

phagophore growth can apparently be sourced to a variety of cellular reservoirs (Klionsky 2007). In selective autophagy, the cargo itself templates the size and shape of the phagophore (Zaffagnini and Martens 2016; Sawa-Makarska et al. 2014; Wurzer et al. 2015). In bulk autophagy, it is less clear how this occurs, but the actin cytoskeleton is involved (Mi et al. 2015). Finally, the cup closes upon itself. The narrow gap at the tip of the cup fuses, leading to the complete sequestration of the material inside. The outer membrane of the autophagosome then fuses with the lysosome (vacuole in yeast or plants) to form a structure known as the autolysosome. At this stage, the inner membrane and all of its contents are degraded. This review will focus on the earliest steps in the process: the formation of the PAS, and the initial nucleation of the phagophore at the PAS.

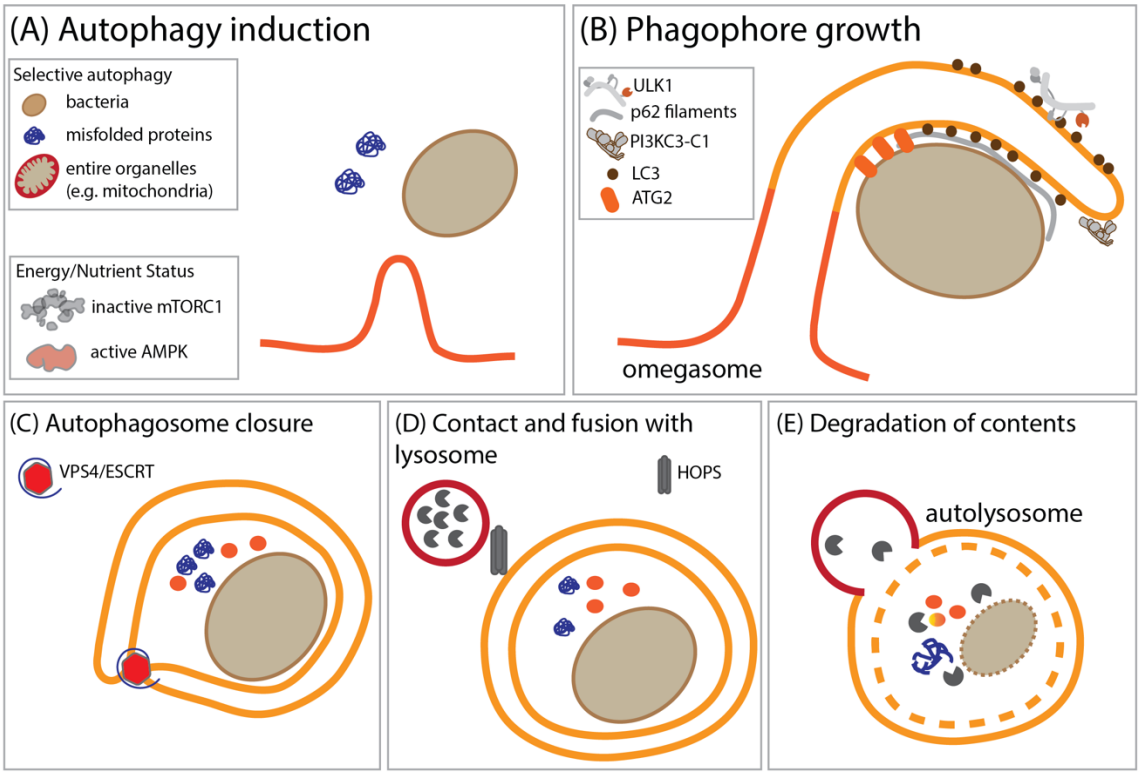

Figure 1.1 Autophagy initiation
(A) Autophagy induction begins at subdomains of the ER, either ER-exit sites or the ERGIC. (B) The Pre-Autophagosome Structure (PAS) grows out of the omegasome, forming the double-membrane phagophore. Elongation takes place at the tips of the phagophore where PI(3)P is generated by PI3KC3-C1. (C) Autophagosome closure requires the ESCRTs. (D) The HOPS complex facilitates lysosome fusion. (E) The resulting autolysosome degrades the internal contents.

The conserved machinery for autophagosome formation (Mizushima and Komatsu 2011; H. Suzuki et al. 2017; James H. Hurley and Schulman 2014) contains two major initiation complexes that are a central focus of this review: the ULK1 complex (known as the Atg1 complex in yeast) and the class III PI 3-kinase complex I (PI3KC3-C1) (Table 1). The sole conserved transmembrane protein in the core machinery, Atg9, is also closely connected to initiation. The PI3P binding WIPI 1-4 proteins and the Atg8-family and Atg12 conjugation systems

(Atg3, Atg4, Atg5, Atg7, Atg10, Atg12, Atg16, LC3s, and GABARAPs; Table 1) function downstream and drive phagophore elongation. Conjugation of Atg8/LC3 family proteins to phosphatidylethanolamine, known as “LC3 lipidation” for short, is the hallmark downstream reaction driven by these proteins. These Atg proteins were discovered for their roles in autophagy and are primarily dedicated to this function, although “moonlighting” roles in non-autophagic functions have been reported (Joo et al. 2016). Multipurpose membrane trafficking factors also have essential roles in the pathway. In many cases, these roles are also conserved from yeast to humans. These factors include the coat complexes COPI and COPII, the vesicle- and organelle-identifying RAB GTPases, and SNARE proteins of vesicle fusion (Nair et al. 2011). In selective autophagy, a variety of adaptor proteins link cargoes to the autophagy machinery, including p62, Optineurin (OPTN), and NPD52 (Shaid et al. 2013; Zaffagnini and Martens 2016).

Autophagy complex	Mammals	Function	Yeast	Function	Protein interactors
ULK1/Atg1 complex	ULK1	S/T kinase	Atg1	S/T kinase	Atg13/ATG13 HORMA domain binds Atg9/ATG9 Atg1/ULK1 has Atg8/LC3 interacting motif (AIM/LIR) Atg1 is recruited by Ytp1 (TRAPPIII)
	ATG13	Regulatory subunit	Atg13	Regulatory subunit	
	FIP200	Scaffold	Atg17, Atg11	Scaffold	
	ATG101	Regulatory			
			Atg29	Budding yeast specific	
			Atg31	Budding yeast specific	
Class III PI3-kinase complex I	VPS34	PI kinase	Vps34	PI kinase	BECN1 interacts with BH3 domain–containing proteins, AMBRA1
	VPS15	Scaffold	Vps15	Scaffold	
	BECN1	Regulatory subunit	Atg6/Vps30	Regulatory subunit	
	ATG14L	PAS targeting	Atg14	PAS targeting	
	NRBF2	Activator	Atg38	Activator	
ATG9	ATG9	Transmembrane protein localizes to small vesicles	Atg9	Transmembrane protein localizes to small vesicles	Yeast Atg13 binds Atg9
Rab1	Rab1	Rab GTPase	Ypt1	Rab GTPase	Ypt1 recruits Atg1
TRAPPIII	TRAPPC8	PAS targeting	Trs85	PAS targeting	TRAPPIII complexes bind COPII vesicles (Sec 23)
UBL-like molecules	LC3A–D, GABARAPs	Autophagosome marker	Atg8	Autophagosome marker	Atg1/ULK1, selective autophagy adaptors

Table 1 Autophagy genes associated with autophagosome initiation (from J.H. Hurley & Young, 2017)

1.3 The ULK1 Complex

Autophagy initiation starts with the activation of the ULK1 complex (Atg1 complex in yeast) (Lin and Hurley 2016; Papinski and Kraft 2016). ULK1 is part of a family of kinases ULK1-4 in humans. Isoform ULK1 is the most important of these in autophagy. In some cells lines it is necessary to block both ULK1 and ULK2 to completely shut down autophagy, however ULK2 is less characterized and will not be discussed further. The ULK1 complex consists of ULK1 itself, and the non-catalytic subunits FIP200, Atg13, and Atg101 (Ganley et al. 2009; Hosokawa et al. 2008; Jung et al. 2008) (Figure 1.2). FIP200 is a large predicted coiled coil

protein involved in scaffolding. Atg13 and Atg101 contain HORMA (Hop/Rev7/Mad2) (Jao et al. 2013) domains which heterodimerize with each another (H. Suzuki et al. 2015; Michel et al. 2015; Qi et al. 2015). Atg13 contains a long IDR (intrinsically disordered region) following the HORMA domain, and the C-terminal part of its IDR contains motifs that bind to the C-terminal EAT/tMIT domain of ULK1 (Fujioka et al. 2014). The budding yeasts have a uniquely complicated version of the ULK1 complex, known as the Atg1 complex. Atg1 contains the active kinase domain. Atg13 is conserved, but Atg101 is absent from budding yeasts. FIP200 is replaced by two scaffolding subunits: Atg11, which functions in selective autophagy (Yorimitsu and Klionsky 2005), and Atg17, which functions in bulk autophagy. Atg17 in turn co-assembles with two smaller subunits, Atg29 and Atg31 (Kabeya et al. 2004; Kirisako et al. 2000) (Figure 1.2).

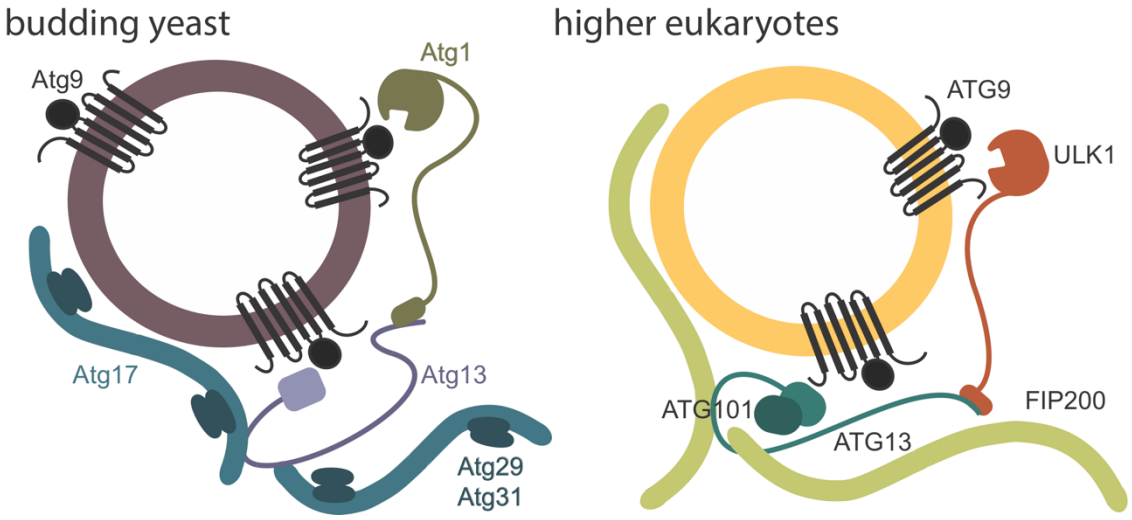

Figure 1.2 Model of the autophagy initiation complex in yeast and mammals
Small vesicles containing Atg9 interact with the autophagy initiation complex- the Serine/Threonine kinase Atg1, the HORMA domain containing Atg13, the S-shaped Atg17, bound to the yeast specific proteins Atg29, Atg31. Based on yeast observations, it is proposed that small vesicles containing ATG9 interact with the autophagy initiation complex- the Serine/Threonine kinase ULK1, the HORMA domain containing ATG13 forms a heterodimer with the HORMA domain of ATG101, FIP200 is modeled on Atg17. However, the yeast interaction site in Atg9 is not conserved in humans.

The large scaffolding subunits Atg11 and FIP200, whose structures are unknown, are similar to each other in size and predicted helical content. Their C-terminal are homologous, suggesting a common function. Atg17 is smaller than Atg11 and FIP200, and aside from a similar helical content, has little sequence similarity with Atg11 and FIP200. It is often stated in the literature that Atg17 and FIP200 are orthologs. It is important to bear in mind that this inference, while reasonable, is based on functional parallelism, not detailed sequence or structural similarity.

1.4 ULK1 kinase activation and inactivation

ULK1 is activated in at least three ways upon autophagy induction, and all three are essential. Protein kinase activity needs to be switched on, the active kinase needs to be recruited to the PAS, and essential – though still vaguely defined– non-catalytic scaffolding activities must be turned on. Autophosphorylation of the kinase domain's activation loop at Thr180 of ULK1 (Bach et al. 2011; Lazarus, Novotny, and Shokat 2015). Thr226 in yeast Atg1; is essential for activation. Autophosphorylation is promoted by conditions that induce autophagy and by co-assembly with other subunits of the complex (Kamber, Shoemaker, & Denic, 2015; Yamamoto et al., 2016; Yeh, Wrasman, & Herman, 2010). This co-assembly in turn increases the local concentration of Atg1 molecules and promotes their mutual autophosphorylation. This can occur both in selective autophagy under nutrient-rich conditions (Kamber, Shoemaker, and Denic 2015) and in starvation (Yamamoto et al., 2016). Following activation, ULK1 (and PI3KC3-C1) can be ubiquitinated by the Cul3-KLHL20 ligase complex and degraded (Liu et al. 2016), thereby switching off the autophagy initiating signal.

How does starvation trigger Thr180 phosphorylation of ULK1? Autophosphorylation is usually promoted by the dimerization or higher-order oligomerization of kinases. The C-terminal EAT domain of yeast ULK1 dimerizes in isolation (Yamamoto et al. 2016; Ragusa, Stanley, and Hurley 2012; Stjepanovic et al. 2014), however, full-length ULK1 is reportedly a monomer in the absence of other subunits (Rao et al. 2015). It is currently not clear whether ULK1 undergoes regulated dimerization via its EAT domain under some conditions. ULK1 is bridged by Atg13 to the scaffolding subunit FIP200 (Ganley et al. 2009; Hosokawa et al. 2008; Jung et al. 2008). In yeast, Atg13 bridges to Atg11 (Ohsumi 2000) and Atg17 (Cheong et al. 2005) in yeast. While the oligomeric state of FIP200 and Atg11 is unknown, Atg17 is a constitutive dimer (Ragusa, Stanley, and Hurley 2012). The recruitment of ULK1 to FIP200 via the intermediation of Atg13 could in principle be a mechanism for ULK1 trans-autophosphorylation.

Whether and how starvation regulates formation of the ULK1 complex has been intensively investigated, yet consensus has been elusive. mTORC1 is a master regulator of cell growth and metabolism, and its inactivation in response to amino acid depletion is a major trigger for autophagy (Bar-Peled and Sabatini 2014). In the canonical model of the process, Atg13 is phosphorylated by mTORC1 under non-starved conditions (Kamada et al. 2010). The extensive phosphorylation sites inhibit the assembly of Atg13 with both ULK1 and Atg17 by introducing steric and electrostatic repulsion into the binding sites on ULK1 and Atg17 (Fujioka et al. 2014). On the other hand, it has also been reported that the ULK1 complex is assembled constitutively in both nutrient-rich and starved conditions (Kraft et al. 2012). Of 51 reported phosphorylation sites within Atg13, six fall within the crystallographically defined ULK1-binding site. Mutation of all of these sites from Ser to the phosphomimetic Asp only reduces ULK1 binding by a factor of three (Fujioka et al. 2014). The effect of Atg13 phosphorylation on Atg17 binding may be larger. Two of the 51 reported phosphorylation sites occur in the

Atg17 binding site of Atg13. Although not quantitated, phosphomimetic mutations in these two residues substantially disrupt binding (Fujioka et al. 2014). Phosphoregulation at the level of the Atg17-Atg13 interaction thus seems to lead to bigger affinity changes than for the Atg1-Atg13 interaction. FIP200 and Atg11 are less tractable biochemically than Atg17, and little is known at the quantitative and structural level about how ULK1 association with these scaffolds is regulated. It is often stated that ULK1 is assembled constitutively in mammalian cells (Ganley et al. 2009; Hosokawa et al. 2008; Jung et al. 2008), yet on the other hand, the mammalian Atg13-Atg101 subcomplex appears to have autophagic functions that are independent of the ULK1 complex (Heike et al. 2015).

Other regulatory mechanisms function in parallel to, or even antagonize mTORC1 regulation (Figure 1.3). AMPK (AMP-activated protein kinase) upregulates autophagy in response to energy depletion as detected by an increase in cytosolic AMP. AMPK directly phosphorylates ULK1 at multiple sites in its central IDR, leading to its activation (Egan et al. 2015; J. Kim et al. 2011; Shang et al. 2011; Mack et al. 2012). The details of how these IDR phosphorylation sites communicate with the catalytic domain remain to be elucidated. In selective autophagy, ULK1 must be locally active even under fed conditions when mTORC1 is also active. Relatively little is known about how the ULK1 complex is sheltered from inactivation under these conditions. Huntingtin, the protein product of the gene mutated in Huntington's disease, interacts with ULK1 and has been proposed to have such an ULK1-shielding function (Rui et al. 2015).

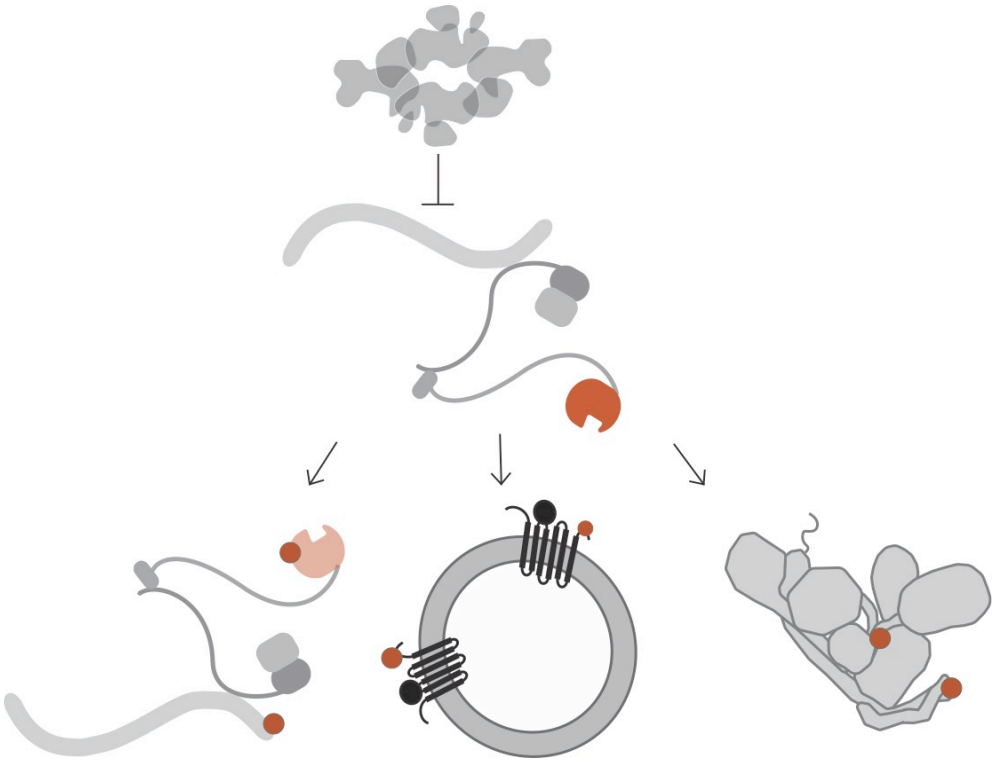

Figure 1.3 Phosphoregulation of core autophagy machinery
ULK1 is inhibited by mTORC1. When mTORC1 is inactivated, ULK1 becomes activated, thereby leading to autophosphorylation within (1) ULK1, ATG13, ATG101 and FIP200. Multiple phosphorylation sites occur within ATG13, one is shown for clarity (2) the phosphorylation of ATG9, and (3) the phosphorylation of PI3KC3-C1- at the N-terminus of BECN1 and within the C2 domain of VPS34.

1.5 ULK1 recruitment to initiation sites

Recruitment of the ULK1 complex to sites of autophagy initiation is the second regulated step in its activation. In bulk autophagy in yeast, PAS recruitment is regulated at the level of Atg13 phosphorylation. Atg17, along with its accessory proteins Atg29 and Atg31, is the first protein to arrive at the PAS is yeast (K. Suzuki et al. 2007), which set the stage for the recruitment of Atg13 and Atg1 as described above. The EAT domain of ULK1, the locus for Atg13 binding, is essential for its recruitment to the PAS in human cells (Chan et al. 2008). This suggests that the principles for recruitment are similar in this respect in yeast and mammals. The concept that the mammalian ULK1 complex is constitutively assembled, however, is hard to reconcile with a yeast-like mechanism.

A number of other protein-protein interactions influence ULK1 localization to the PAS. The LC3 family proteins bind to LIR/AIM motifs in both human and yeast ULK1/Atg1 (Kraft et al. 2012; Alemu et al. 2012) and in human Atg13 (Alemu et al. 2012). LC3 conjugation is thought to occur downstream of ULK1 activation, however, and the LIR/AIM motifs seem likely to be involved in later events in autophagosome biogenesis. The yeast Atg1 complex binds to Atg9 through a direct interaction between the HORMA domain of Atg13 and the N-terminal soluble domain of Atg9 (S. W. Suzuki et al., 2015), and perhaps also

through Atg17 (Rao et al. 2015; Sekito et al. 2009). Yeast Rab1 (Ypt1) is a small G-protein better known as a regulator of ER-Golgi and intra-Golgi traffic, binds to Atg1 and helps recruit it to the PAS (J. Wang et al. 2013). Ypt1 is activated and recruited to the PAS by the TRAPPIII complex, which binds to Atg9 (Kakuta et al. 2012) and Atg17 (J. Wang et al. 2013). TRAPIII is also implicated in mammalian autophagy (Lamb et al. 2016). C9orf72 is mutated in the most common hereditary forms of amyotrophic lateral sclerosis (ALS) and frontotemporal dementia (FTD), and was recently shown to be important for the RAB1A dependent recruitment of ULK1 to the PAS in human cells (Webster et al. 2016). C9orf72 contains a DENN domain, and in many cases DENN domain proteins act as RAB guanine nucleotide exchange factors (GEFs). Apparently the C9orf72 DENN binds to RAB1A but lacks GEF activity, making C9orf72 a RAB1A effector rather than a RAB1A GEF. It has been proposed that impairment of ULK1 recruitment to the PAS in C9orf72 mutants is responsible for their disease phenotype (Webster et al. 2016). Thus, a circuit involving ATG9, RAB1, and TRAPPIII appears to be important for the recruitment of ULK1 to the PAS.

1.6 ULK1 substrates

The ULK1 kinase transduces pro-autophagic signals by phosphorylating many substrate proteins (Papinski and Kraft 2016). The ULK1 consensus site is characterized by a preference for hydrophobic residues surrounding the serine phosphoacceptor (Papinski and Kraft 2016; Egan et al. 2015). This is not a rare sequence, and the numerous substrates of ULK1 include itself and other subunits of the ULK1 complex; other elements of the core autophagy machinery, including PI3KC3-C1 subunits and Atg9; and other proteins whose connections to autophagy are understood to varying extents (Papinski et al. 2014; Papinski and Kraft 2016). Within the ULK1 complex, there are phosphorylation sites in ATG101 and multiple sites in FIP200 and ATG13 (Egan et al. 2015). The ATG101 phosphorylation sites, Ser11 and Ser203, are at the start of the ATG101 HORMA domain, and in a flexible region just past the end of the HORMA domain, respectively.

The PI3KC3-C1 complex, another pivotal autophagy initiating complex, is one of the most important and best understood targets of ULK1 phosphorylation. ULK1 phosphorylates Ser15 and other sites in BECN1, activating the PI3KC3 complex and promoting autophagy (Egan et al. 2015; Russell et al. 2013). The PI3KC3-C1 catalytic subunit VPS34 contains a major ULK1 phosphorylation site at Ser249 (Egan et al. 2015). The consequences of these phosphorylations are discussed further in the PI3KC3-C1 section. The massive PI3KC3-C1-associated IDR protein AMBRA1 is another ULK1 substrate (Di Bartolomeo et al. 2010). In yeast, Atg2 and Atg9 are important substrates for Atg1 (Papinski et al. 2014) Atg9 phosphorylation is important for its recycling, although not for its initial translocation to the PAS, as discussed below in the section on Atg9 vesicles. ULK1 is critical for selective as well as bulk autophagy. It phosphorylates the cargo adaptor protein p62, increasing the binding affinity of p62 for ubiquitin (Lim et al. 2015). ULK1 also phosphorylates FUNDC1 to promote mitophagy (Wu et al. 2014). Many of these phosphorylations, including those of ULK1 and PI3KC3-

C1 subunits, seem to be very important in autophagy initiation, while in other cases such as Atg9, the effect is further downstream.

1.7 Non-catalytic functions of the ULK1 complex

ULK1 probably regulates autophagy induction at a third level, through its non-catalytic activities. These are essential for autophagy initiation, at least in yeast (Abeliovich et al. 2003). Some 90% of the mass of the ULK1 complex consists of non-catalytic domains (Lin and Hurley 2016). We will enumerate some of the non-catalytic functions imputed to these domains. The ULK1 EAT domain dimerizes and is capable of tethering high curvature lipid vesicles in vitro (Ragusa, Stanley, and Hurley 2012), which could be relevant to vesicle clustering at the PAS. The dimeric Atg17 subunit of the yeast Atg1 complex has a double crescent shape (Ragusa, Stanley, and Hurley 2012) that suggests it could not just tether vesicles, but scaffold them rigidly into a specific geometry preceding cup formation. The combination of Atg1 and Atg17 dimers provides a mechanism for higher-order assembly of daisy-chained or branched assemblies of Atg1 complexes at the PAS (Köfinger et al. 2014). Moreover, the C-terminal intrinsically disordered region (IDR) of Atg13 has at least two Atg17 binding sites, located such that they must bridge different Atg17 dimers (Yamamoto et al. 2016). Taken together, the dimerization data and the crosslinking ability of Atg13 suggests a meshwork model for organization of the PAS (Figure 1.4)

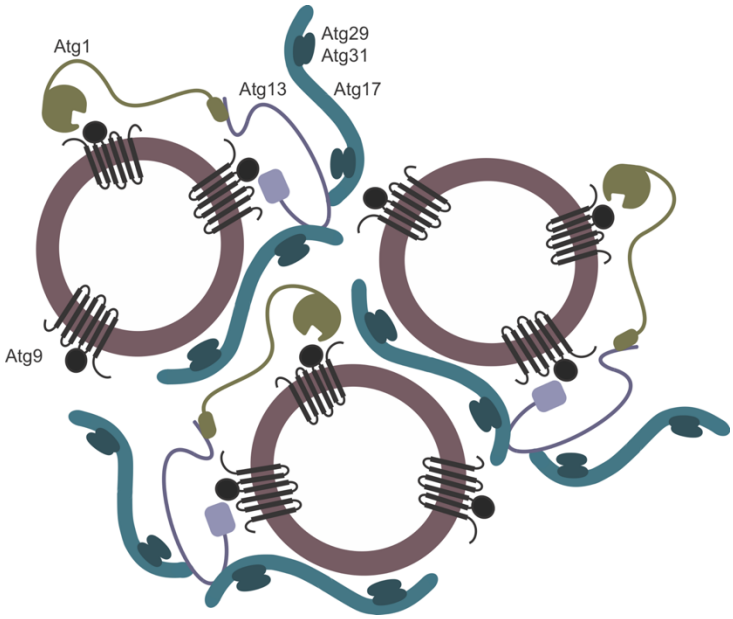

Figure 1.4 Meshwork model
From research in yeast model systems, the Intrinsically Disordered Regions (IDRs) within Atg1 and Atg13 as well as the position of Atg13-Atg17 contacts lead a proposed mechanism in which ATG proteins form a “meshwork.”

Mammalian Atg13 and Atg101 form a heterodimeric subcomplex consisting of the HORMA domains of the two proteins. Atg101 has a hydrophobic binding site revealed by the crystal structures that has been dubbed the “WF finger” (S. W. Suzuki et al. 2015a). The binding partner of the WF finger is not known, however it is clear that the Atg13, Atg101 and FIP200 have functions in autophagy that are fundamentally important and independent of the ULK1 (and ULK2) kinases (Heike et al. 2015; Alers et al. 2011).

1.8 The PI3KC3-C1 Complex

The class III Phosphatidylinositol 3-kinase Complex (PI3KC3) phosphorylates the lipid head group of phosphatiylinositol to generate phosphatidylinositol 3-phosphate (PI(3)P) (Herman and Emr 1990). Formation of PI(3)P is an essential early event in autophagy initiation, occurring just downstream of ULK1 (Kihara et al. 2001). PI3KC3 forms at least two distinct complexes, known as complexes–I and II (Itakura et al. 2008). Both complexes contain the catalytic subunit VPS34, the putative protein kinase VPS15, and BECN1. Complex I (PI3KC3-C1) contains ATG14 (Itakura et al. 2008), which directs the complex to the PAS. PI3KC3-C1 facilitates elongation while complex II containing UVRAG directs endosome and autophagosome maturation (Jonathan M Backer 2008).

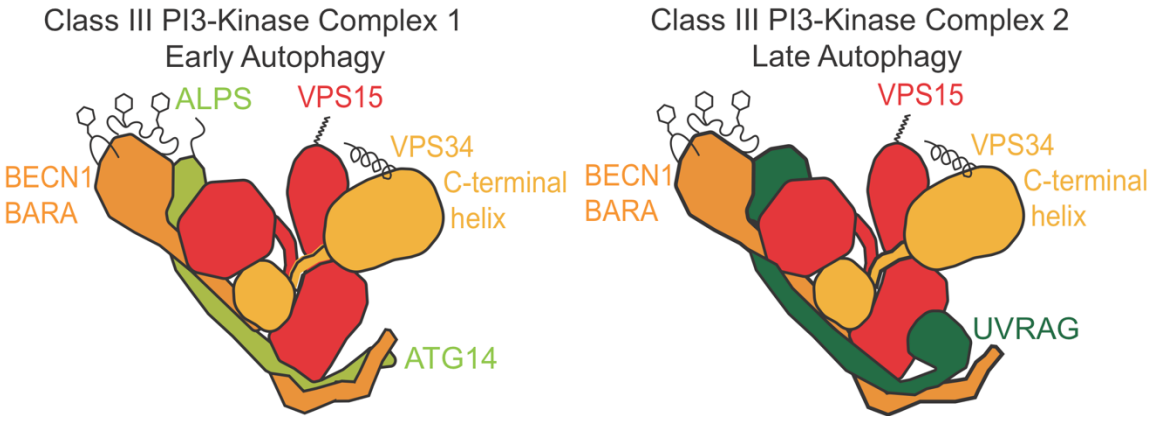

Figure 1.5 Architecture of Class III PI3-Kinases

Known membrane binding sites are noted on the subunits of PI3KC3-C1 and -C2. VPS34 has a C-terminal helix that embeds itself into a membrane and facilitates the phosphorylation of phosphatidylinositol 3-phosphate from phosphatidylinositol. VPS15 has an N-terminal myristoylation site. The BARA domain of BECN1 has a number of aromatic residues required for membrane binding. ATG14 possesses a C-terminal amphipathetic helix. C2 domains are noted for their membrane binding abilities, the C2 of VPS34 is instead a site of multiple protein-protein interactions. Whether the C2 of UVRAG plays a structural role or if binds membrane remains to be determined.

For many years, progress in understanding the structure of PI3KC3-C1 was gradual and fragmentary. Structures of the VPS34 catalytic and associated helical domain (Miller et al. 2010), the central coiled coil (Huang et al. 2012), and C-terminal BARA domain (N. N. Noda et al. 2012; Huang et al. 2012) of Vps30/BECN1, and the WD40 domain of Vps15 (Heenan et al. 2009) were all solved separately. More recently, the structure of the complete human complex I was solved by electron microscopy (Baskaran et al. 2014), revealing a V-shaped architecture. The x-ray crystal structure of yeast complex II showed a conserved architecture and domain placement (Rostislavleva et al. 2015) and added new information, including the presence of a BARA-like domain in Vps38 (yeast UVRAG). The left hand side of the complex (as seen in the canonical view, Figure 1.5) includes the central coiled coils and C-terminal domains of BECN1 and ATG14. The N-termini of BECN1 and ATG14 are at the base of the V. A

number of regulatory signals, described below, converge on these sites. On the right hand side is the catalytic subunit VPS34 and the protein kinase domain of VPS15. VPS15 bridges the left and right arms of the complex. Its WD40 domain is part of the left arm, and serves as a docking site for BECN1 and ATG14, while its HEAT domain spans the two arms. Similar to the situation with the ULK1 complex, the catalytic domain of VPS34 comprises just ~10 % of the mass of the PI3KC3-C1 complex. Its placement within the context of the rest of the much larger V-shaped complex highlights the likely importance of the regulatory and scaffolding roles of the non-catalytic ~90%.

1.9 PI3KC3-C1 recruitment to the PAS

The functioning of PI3KC3-C1 in autophagy requires its translocation to the PAS, which is driven by its unique Atg14 subunit (Itakura et al. 2008). A cysteine-rich domain near the N-terminus of Atg14 is essential for its starvation-induced translocation to the PAS (Matsunaga et al. 2009). The structure of this domain is unknown, as is its putative interaction partner at the PAS. A C-terminal amphiphatic helix deemed the BATS domain (Barkor/ATG14L Autophagosome Targeting Sequence) (Fan, Nassiri, and Zhong 2011), which is an example of the larger class of amphipathic lipid packing sensor (ALPS) motifs (Drin et al. 2007), is also important for targeting. This is thought to be due to its ability to bind high-curvature lipids, although it is important to note that ALPS motifs can also bind loosely packed low curvature membranes such as are found at the ER (Vanni et al. 2013).

In addition to the complex I- and autophagy-specific PAS- and ER-targeting motifs in Atg14, other regions of the PI3KC3 complexes have been implicated in binding less specifically to membranes. The C-terminal BARA domain of BECN1, at the tip of the left arm, is proposed to insert into membranes via an aromatic finger (Huang et al. 2012). An additional membrane binding site with the BECN1 BARA domain is within a beta-sheet that flips out to bind membranes via two phenylalanines (Chang et al. 2019), see chapter 4. On the opposite side of the V-shape is VPS34, whose final kα12 helix must bind membranes in order for lipid phosphorylation to take place (Miller et al. 2010). On the other hand, although it had been expected that the C2 domain of VPS34 would binds membranes, the structure of complex II suggests that the C2 domain is only involved in protein-protein interactions. Finally, the N- myristoylation of VPS15 provides one more membrane contact (Stack et al. 1993). The actual geometry of PI3KC3 docking on membranes through the various known and putative anchoring motifs is still unknown, and will be important to clarify.

1.10 PI3KC3-C1 regulatory proteins

The kinase activity of PI3KC3-C1 is regulated through post-translational modifications and a variety of protein-protein interactions. The cast of players that interact with PI3KC3 complexes is extensive and leads to the suggestion that the “two-complex” model is an oversimplification. PI3KC3-C1 associates tightly with a fifth subunit, known as NRBF2 (Nuclear Receptor Binding Factor 2) (Cao et al. 2014; Ma et al. 2017; Lu et al. 2014; Y. Zhong et al. 2014) in

mammals and Atg38 (Araki et al. 2013) in yeast. NRBF2/Atg38 contain an N-terminal three-helix bundle MIT (Microtubule-Interacting and Trafficking) domain and a coiled-coil-containing domain at the C-terminus (Ohashi et al. 2016; L. N. Young et al. 2016) that induces dimerization. NRBF2 binds to the base of complex I through interactions with the N-terminus of ATG14L and BECN1, enhances kinase activity in vitro and leads to the dimerization of human complex I (L. N. Young et al. 2016; Ohashi et al. 2016). Although yeast Atg38 is dimeric as well, it does not facilitate yeast PI3KC3-C1 dimerization (Ohashi et al. 2016). Mammalian PI3KC3-C1 dimerization and kinase activation by NRBF2 seem to be completely decoupled from one another (L. N. Young et al. 2016). Since kinase dimerization is not required for its enzymatic activation, both the mechanism of allosteric activation and the biological function of dimerization remain to be clarified.

The anti-apoptotic factor Bcl-2 (B-Cell lymphoma 2) binds to the BH3 (Bcl-2 Homology domain) of BECN1 (Oberstein, Jeffrey, and Shi 2007), which places its location in the complex close to, and perhaps even overlapping, with the NRBF2 binding site (L. N. Young et al. 2016). The affinity of Bcl-2 is fifty time lower than that of NRBF2 (L. N. Young et al. 2016). Unlike NRBF2, Bcl-2 rapidly exchanges on and off PI3KC3-C1 (L. N. Young et al. 2016). Bcl-2 binding to BECN1 inhibits VPS34 kinase activity and antagonizes autophagy (Pattingre et al. 2005). Because the binding site is remote from the lipid kinase domain, the mechanism for this inhibition is unknown, but presumably must involve long-range allosteric communication. Additionally, BECN1 is capable of binding with other anti-apoptotic Bcl-2 family members (Bcl-XL, Bcl-w, Mcl-l) through its BH3 domain (Oberstein, Jeffrey, and Shi 2007). Only ER-localized Bcl-2 is capable of inhibiting autophagy, and mitochondrial Bcl-2 was not (Pattingre et al. 2005).

AMBRA1 (Autophagy And Beclin 1 Regulator 1) binds to PI3KC3 in cells and promotes autophagy (Fimia et al. 2007). A full biochemical characterization with recombinant proteins is still lacking, as the size of this IDR protein makes it challenging to study. AMBRA1 is phosphorylated by ULK1 as described above, which is proposed to activate PI3KC3-C1 by releasing it from microtubules (Di Bartolomeo et al. 2010). The most recent addition to the family of PI3KC3-C1 interactors is PAQR3 (progestin and adipoQ receptor 3), a Golgi localized multipass transmembrane protein that has been proposed to promote autophagy by helping to assemble PI3KC3-C1 (Xu et al. 2016). The degree to which PI3KC3-C1 assembly (as opposed to the better-studied topics of the acute regulation of its enzyme activity and localization) is a regulated step has been relatively little explored as yet.

1.11 PI3KC3-C1 phosphoregulation

BECN1 is phosphoregulated by at least five kinases: ULK1, MAPKAP2 (mitogen-activated protein kinase-activated protein kinase 2), AMPK, and DAPK (death-associated protein kinase) that promote autophagy activation while EGFR lead to autophagy suppression. ULK1 activates PI3KC3-C1 by phosphorylating BECN1 at Ser15 (Russell et al. 2013). Upon stress, the kinases MAPKAPK2/3 phosphorylate BECN1 at Ser90, leading to autophagy activation (Wei et al.

2015). Upon glucose starvation, AMPK enhances autophagy by phosphorylating BECN1 at Ser90 and Ser94 Kim 2013. Ser90 phosphorylation is reversed by protein phosphatase 2A (PP2A) (Fujiwara et al. 2016), which is upregulated by starvation (Wong et al. 2015). Ser15, Ser90, and Ser94 are all located in the flexible N-terminal portion of BENC1, and it is still unknown how these signals are communicated to the catalytic domain.

DAPK phosphorylates BECN1 at Thr119, which is located within the BH3 domain, and thereby inhibits binding of Bcl-2 and Bcl-X-L (Zalckvar et al. 2009). AMPK, which is generally pro-autophagic, seems to selectively suppresses the activity of the non-autophagic PI3KC3 complex by phosphorylating Thr163 and Ser165 in VPS34 (J. Kim et al. 2013). EGFR suppresses autophagy through phosphorylation of BECN1 at Tyr229, Tyr233, Tyr352 (Wei et al. 2013), which might, in principle, regulate assembly of the coiled-coil complex. Additionally, autophagy suppression can occur through phosphorylation at the C-terminus of ATG14L by mTORC1 (mechanistic Target Of Rapamycin Complex 1) at positions Ser223, Ser233, Ser383, and Ser440 (Yuan et al. 2013). Phosphatases that remove these signals have not been reported, however it has been reported that the Cul3-KLHL20 ligase complex promotes the ubiquitination of BECN1 and VPS34, thereby targeting PI3KC3-C1 for degradation (Liu et al. 2016). It is still difficult to rationalize many of these effects at the structural level. This will require obtaining structures at higher resolution and comparison of phosphorylated and dephosphorylated states at the structural level.

1.12 Role of vesicles in autophagy initiation

In yeast, a growing body of evidence suggests that the autophagosome is nucleated by the coalescence of Atg9 and COPII vesicles (Mari et al. 2010). In yeast, Atg9 vesicles are derived from the trans-Golgi network (TGN) (Mari et al. 2010), while COPII vesicles emerge from ER exit sites (ERES) (Brandizzi and Barlowe 2013). Both Atg9 and COPII vesicles seem to have central roles in autophagy initiation in mammals, as well. In mammals, the phagophore begins at a tubular outgrowth Hayashi-Nishino 2009 of the PI(3)P-positive domain of the ER known as the omegasome (Axe et al. 2008). The relationship between the tubular outgrowth and the pool of COPII vesicles is still unclear. Here we focus on recent advances in understanding the roles of the vesicles themselves in initiating autophagy.

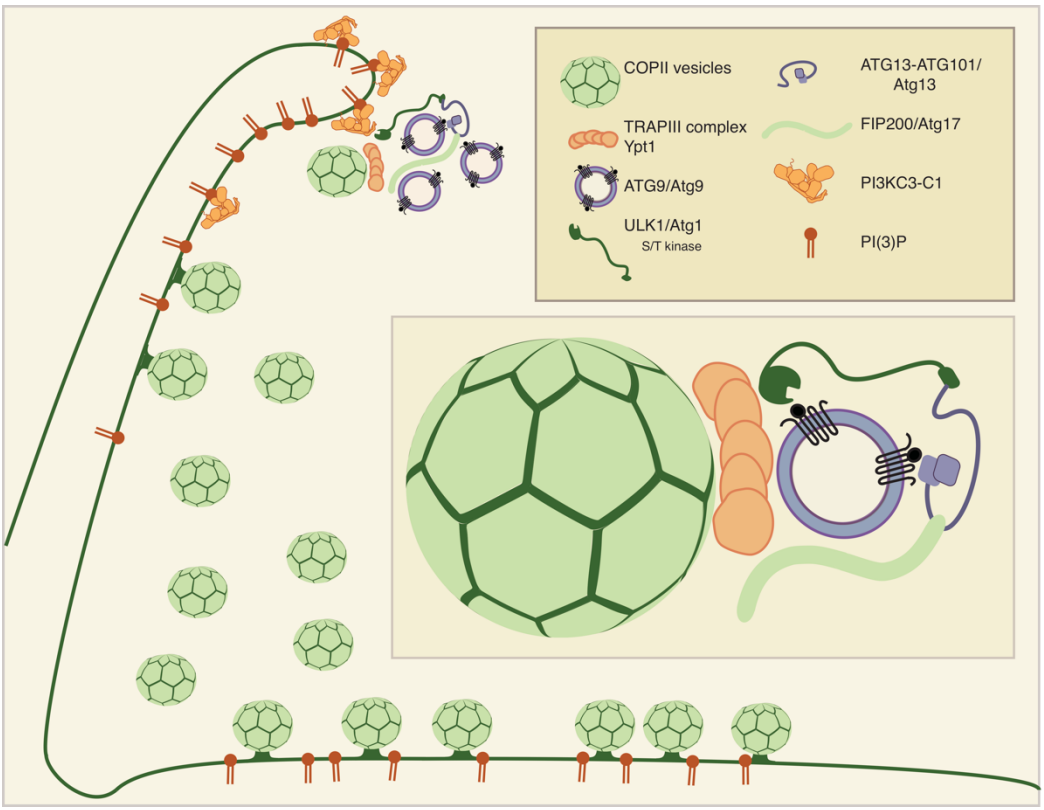

Figure 1.6 Role of COPII and ATG9 vesicles in autophagy initiation at the omegosome

1.13 Atg9 vesicles

Atg9 is the only integral membrane protein that is essential for autophagy (Lang et al. 2000; T. Noda et al. 2000). This large protein (997 residues in yeast) contains six predicted transmembrane helices spread through its central region, and has large cytosolic IDRs in its N- and C-terminal regions. Atg9 self-associates within membranes into a higher-order assembly (He et al. 2008). Atg9 is incorporated in small vesicles- diameter of 30-40 nm (Mari et al. 2010) or 30-60 nm (Yamamoto et al. 2012b). While other Atg proteins are often diffusely distributed in the cytosol under fed conditions, as a membrane protein, Atg9 vesicles must reside in a vesicular reservoir (Puri et al. 2014). Atg9 vesicles are generated and transported from the Golgi (Fulvio Reggiori et al. 2004; A. R. J. Young et al. 2006). In yeast, the process depends on Atg23 and Atg27 (Fulvio Reggiori et al. 2004) and the Rab/RabGEF pair Sec4 and Sec2 (Geng et al. 2010). In nutrient rich conditions, Atg9 localizes to the trans-Golgi network and early and late post-Golgi endosomes (Shirahama-Noda et al. 2013).

In starvation, Atg9 vesicles are mobilized to the PAS by TRAPPIII (Lamb et al. 2016; Shirahama-Noda et al. 2013; Yamamoto et al. 2012) and, in yeast (Suzuki et al. 2015) but not mammals Itaka 2015, by the ULK1 complex. Specifically, the yeast Atg13 HORMA domain binds to the N-terminus of Atg9, which is poorly conserved in mammals. In one estimate, three Atg9 vesicles containing ~27 molecules of Atg9 each assemble at the yeast PAS (Yamamoto et al. 2012). In yeast, Atg9 is important for recruiting Atg2 (Shintani et al. 2002;

C. W. Wang et al. 2001) and facilitates the recruitment of PI3KC3-C1 (Suzuki et al. 2015) to the PAS. The amount of Atg9 expressed in cells appears to control the frequency of autophagosome formation (Jin and Klionsky 2014). Phosphorylation of the N-terminal domain of Atg9 by an unknown kinase upregulates the recruitment of Atg9 to the PAS and its ability to initiate autophagy (Feng et al. 2016). Clearly, the bulk lipid contributed by such a small number of vesicles is a miniscule fraction of what is needed to generate an autophagosome. Consistent with this idea, mammalian ATG9A is not a bulk component of autophagosomes (Orsi et al. 2012), but rather seems to recycle out of the phagophore prior to closure. Thus, the importance of Atg9 seems to more as an organizing center for the initial nucleation of the phagophore.

1.14 COPII vesicles in autophagy

The COPII coat consists of the Sar1 GTPase, the inner membrane- and cargo-binding Sec23 and Sec24 subunits, and the outer cage-forming Sec13 and Sec31 subunits (Faini et al. 2013). COPII vesicles have a long-established role, unrelated to autophagy, as the initial carriers of secretory cargo out of the ER (Brandizzi and Barlowe 2013). COPII was first implicated in autophagosome biogenesis when mutants in Sec23 and Sec24 and in the COPII associated ERES proteins Sec12 and Sec16 were shown to be defective in autophagy (Ishihara et al. 2001). COPII was subsequently found to be physically connected to other core elements of autophagy initiation in yeast, including the Atg1 and PI3K complexes (Graef et al. 2013). In yeast, the Rab1 ortholog Ypt1 activates the casein kinase 1 (CK1) ortholog Hrr25 to phosphorylate Sec23, which is required for COPII vesicle sorting to the PAS (J. Wang et al. 2015). COPII vesicles are targeted for membrane fusion in autophagy by the ER SNARE protein Ufe1, which is a Q(a) SNARE and a member of the syntaxin family (Lemus et al. 2016). The COPII vesicle tethering TRAPPIII complex is implicated in autophagy initiation in both yeast (Shirahama-Noda et al. 2013; Lynch-Day et al. 2010; Tan et al. 2013) and mammals (Lamb et al. 2016; Behrends et al. 2010).

In mammals, most of the output of ERES is directed to the cis-Golgi via the ER-Golgi intermediate compartment (ERGIC) (Brandizzi and Barlowe 2013). The ERGIC is the depot for sorting by both the COPI and COPII coats in mammals (Brandizzi and Barlowe 2013). ERGIC membranes support LC3 lipidation in a cell-free system Ge 2013, Ge 2014. In human cells, the ERES protein tectonin β-propeller containing protein 2 (TECPR2), which is mutated in a hereditary spastic paraplegia, connects the COPII subunit SEC24D to LC3C (Stadel et al. 2015). Super-resolution imaging of the mammalian PAS shows that Atg9 vesicles and the ULK1 complex subunit Atg13 coalesce with ERGIC components COPI, COPII, and ERGIC53 (Karanasios et al. 2013). Collectively, these data provide compelling evidence that COPII vesicles have a conserved role in autophagy initiation. The ER is closely associated with autophagosome biogenesis, and COPII vesicle production provides an appealing mechanism for the exchange of membrane from the ER to the phagophore. In contrast to the situation with Atg9 vesicles, COPII vesicles can be formed in large amounts and so could

presumably account for the bulk membrane needed for autophagosome biogenesis, but this has yet to be confirmed quantitatively.

1.15 Conclusion

The “parts list” of autophagy initiation is becoming increasingly well defined. Building on the identification of the key initiating proteins in yeast (Wen and Klionsky 2016; Mizushima and Komatsu 2011), proteomics and mammalian cell biology have fleshed out many additional components (Mizushima and Komatsu 2011; Behrends et al. 2010). With the parts list approaching, perhaps, completion, the big question is how all these parts work together to create the phagophore de novo. As with many other complex processes of cells, the mechanics of how Atg proteins come together with vesicles to create phagophores occurs on the nanoscale, i.e., the length scale of 10s on nm. In the recent past, the dominant experimental approaches in autophagy research have centered on diffraction-limited fluorescence microscopy, co-immunoprecipitation, and protein phosphorylation. These more traditional approaches have yielded many important discoveries, yet they will not be able to break through to resolving the nanoscale mechanisms involved in phagophore initiation. Super-resolution and cryo-electron microscopy methodologies are advancing quickly, and the advances are quickly being adopted in autophagy research. The imaging approaches are being to generate more insights that can be contemplated on the structural scale, and the structural biology studies are expanding in scope to approach the size scales reachable by superresolution imaging. Thus far the insights generated by cell imaging and structural biology have yet to truly converge. Yet it seems that such a convergence will be inevitable. At that point, the rate-limiting step may change from technical challenges to the conceptual challenge of embracing the complexity that these methods are bound to reveal.

CHAPTER 2

Dynamics and Architecture of the NRBF2-Containing Phosphatidylinositol 3-Kinase Complex I of Autophagy

This chapter was published as the following article by Young, Lindsey N., Cho, Kelvin, Lawrence, Rosalie, Zoncu, Roberto. and Hurley, James H. (2016) 'Dynamics and architecture of the NRBF2-containing phosphatidylinositol 3-kinase complex I of autophagy', *Proceedings of the National Academy of Sciences*. doi: 10.1073/pnas.1603650113.

The contributions are as follows: Lindsey Young performed designed and conceived all experiments, Fluorescence Recovery After Photobleaching experiment was performed and analyzed with the help of Kelvin Cho, Rosalie Lawrence, and Roberto Zoncu. Lindsey Young and Jim Hurley wrote the manuscript, with input from all authors.

Chapter 2 : Dynamics and Architecture of the NRBF2-Containing Phosphatidylinositol 3-Kinase Complex I of Autophagy

2.1 Summary

Autophagy (self-eating) is an essential process for cellular self-renewal. The class III phosphatidylinositol 3-kinase complex I (PI3KC3-C1) is central to autophagy initiation. We previously reported the V-shaped architecture of the four-subunit version of PI3KC3-C1 consisting of VPS34, VPS15, BECN1, and ATG14. Here we show that a putative fifth subunit, NRBF2, is a tightly-bound component of the complex that profoundly affects its activity and architecture. NRBF2 enhances the lipid kinase activity of the catalytic subunit, VPS34, by roughly ten-fold. We used hydrogen-deuterium exchange coupled to mass spectrometry (HDX-MS) and negative stain electron microscopy to map NRBF2 to the base of the V-shaped complex. NRBF2 interacts primarily with the N-termini of ATG14 and BECN1. We show that NRBF2 is a homodimer and drives the dimerization of the larger PI3KC3-C1 complex, with implications for the higher-order organization of the preautophagosomal structure.

2.2 Introduction

Autophagy is a pathway of subcellular engulfment and lysosomal transport that is conserved throughout eukaryotes (Mizushima, Yoshimori, and Ohsumi 2011). Survival during starvation is probably the primordial function of autophagy (F. Reggiori and Klionsky 2013). Most current research focuses on a growing array of selective autophagy pathways in human cells (Shaid et al. 2013). These include autophagy of mitochondria (mitophagy), endoplasmic reticulum (ER-phagy), and intracellular microbes (xenophagy). Autophagy is generally considered protective against a range of diseases, including several neurodegenerative diseases (Nixon 2013), microbial infections, and cancer (Galluzzi et al. 2015). Autophagy can also promote tumor growth in late stages of cancer, and therefore agonists and antagonists of autophagy are of interest as potential therapeutics (Galluzzi et al. 2015). The centrality of autophagy to both basic cell processes and human health has leant urgency to understanding its underlying molecular mechanisms.

Bulk and selective autophagy share common machinery for the initiation and growth of the double-membrane sheet known as the phagophore. The phagophore matures and closes to form the autophagosome. The proteins dedicated to autophagy number ~41 in yeast and more in humans. They include the ULK1 protein kinase complex (Atg1 complex in yeast), the phosphatidylinositol 3-kinase complexes I and II (PI3KC3-C1 and –C2), the integral membrane protein ATG9, the WIPIs as PI(3P) receptors, and the ubiquitin-like LC3 protein family and their conjugation pathway. PI3KC3-C1 functions in autophagy initiation (Yun Zhong et al. 2009b; Matsunaga et al. 2010), while PI3KC3-C2 is important for autolysosome formation at a later step in autophagy (C. Liang et al. 2006). The two PI3KC3 complexes share three subunits in common: the lipid kinase subunit VPS34, and the regulatory subunits BECN1 and VPS15. PI3KC3-C2 contains the unique subunit UVRAG, which is

involved in regulating the fusion of autophagosomes to lysosomes (Y.-M. Kim et al. 2015). PI3KC3-C1 is targeted to sites of autophagy initiation (known as the phagophore assembly site (PAS) in yeast) by its unique ATG14 subunit (Itakura et al. 2008; Sun et al. 2008).

The structure of the four-subunit human PI3KC3-C1 assembly was determined at low resolution by our group by negative stain EM, and revealed an overall V-shaped architecture (Baskaran et al. 2014). One arm of the V contains the VPS34 lipid kinase and VPS15 pseudokinase domains, while the other includes BECN1, ATG14, and the WD40 domain of VPS15. The N-termini of BECN1 and ATG14, and the HEAT repeat domain of VPS15 reside near the base of the V. A higher resolution crystal structure of yeast PI3KC3-C2 confirmed these features, with the exception that Vps38 was present instead of ATG14 (Rostislavleva et al. 2015). The complex undergoes at least two large-scale structural movements. The V is capable of opening and closing to the extent of about 45^{o}, and the VPS34 lipid kinase undergoes dislodging from the rest of the complex (Baskaran et al. 2014).

Recently a putative fifth subunit of the PI3KC3-C1 complex was identified in yeast and named Atg38 (Araki et al. 2013). Atg38 consists of an N-terminal MIT (microtubule interaction and transport) domain and a C-terminal coiled coil, together with connecting linkers. Atg38 dimerizes via its coiled coil (Araki et al. 2013). In *atg38Δ* cells, autophagic function is reduced, and the PI3KC3-C1 complex tends to dissociate into subcomplexes consisting of Vps15-Vps34 and Atg6-Atg14. The human ortholog of Atg38 is NRBF2 (Nuclear Receptor Binding Factor 2). In parallel with the observations for Atg38 and yeast PI3KC3-C1, NRBF2 is an interactor and/or component of the mammalian PI3KC3-C1 complex (Lu et al. 2014; Cao et al. 2014; Zhong et al. 2014). Cells from NRBF2 knockout mice show reduced autophagy, reduced PI3KC3 activity, and reduced stability of PI3KC3-C1 (Lu et al. 2014). Knockdown of NRBF2 with shRNA resulted in similar effects (Cao et al. 2014). A third report also concluded that NRBF2 was associated with PI3KC3-C1, however, siRNA knockdown of NRBF2 led to an increase in autophagy in this report (Y. Zhong et al. 2014).

The observations that PI3KC3-C1 contains and/or is regulated by Atg38 in yeast and NRBF2 in mammals suggests a conserved and fundamental role for this protein in autophagy (Levine et al. 2016). We set out to understand the role of NRBF2 in the assembly, activity, architecture, and dynamics of PI3KC3-C1. We found that NRBF2 binds to the four-subunit PI3KC3-C1 with a K_d of 40 nM, and its dissociation from the complex was immeasurably slow. NRBF2 activates the lipid kinase activity of PI3KC3-C1 in vitro. NRBF2 is a dimer and drives the dimerization of the larger PI3KC3-C1 complex, yet its activation of the lipid kinase is equally efficient with the monomeric MIT domain fragment. We probed the effect of NRBF2 on PI3KC3-C1 dynamics by hydrogen-deuterium exchange (HDX), and found that parts of the N-termini of ATG14 and BECN1, and parts of the VPS15 HEAT repeat domain underwent changes. The largest changes mapped to the BH3 domain of BECN1, the binding site for Bcl-2 family members. By electron microscopy, the binding site of the NRBF2 MIT domain responsible for activation was mapped to the based of the V-shaped PI3KC3-C1 structure,

close to the ATG14 and BECN1 N-termini. These data portray the predominant active form of PI3KC3-C1, as it functions in autophagy, as a homodimer of heteropentamers. This new conceptualization of PI3KC3-C1 architecture has significant implications for the membrane interactions, activity, and regulation of PI3KC3-C1 in autophagy induction.

2.3 Results

2.3.1. NRBF2 is a tightly bound subunit of PI3KC3-C1

To investigate whether NRBF2 is an exchangeable vs. permanent subunit of PI3KC3-C1, we performed Fluorescence Recovery After Photobleaching (FRAP). PI3KC3-C1 was immobilized on streptavidin resin through tags containing the streptavidin binding peptide. Purified recombinant GFP-NRBF2 was incubated with these beads for 10 min. The beads were imaged and regions of the streptavidin bead were photobleached while recording fluorescence recovery. After photobleaching via a high intensity laser pulse, GFP-NRBF2 exhibited neglibible fluorescence recovery during 450 seconds of measurement (Fig. 2.1). The anti-apoptotic factor Bcl-2 (B-cell CLL/lymphoma 2) binds the BH3 domain of BECN1, and is considered a negative regulator of autophagy (Pattingre et al. 2005; Siddiqui, Ahad, and Ahsan 2015), but not a permanent subunit of PI3KC3-C1. The Bcl-2 isoform Bcl-X_L binds BECN1 with an affinity of 2.3 μM (Oberstein, Jeffrey, and Shi 2007). As a control, a soluble version of Bcl-X_L lacking its transmembrane domain was purified and exchange of GFP- Bcl-$X_L^{\Delta TM}$ was monitored following the same procedure as for GFP-NRBF2. GFP-Bcl-$X_L^{\Delta TM}$ exhibits steady fluorescence recovery over the same 450 s interval (Figure 2.2).

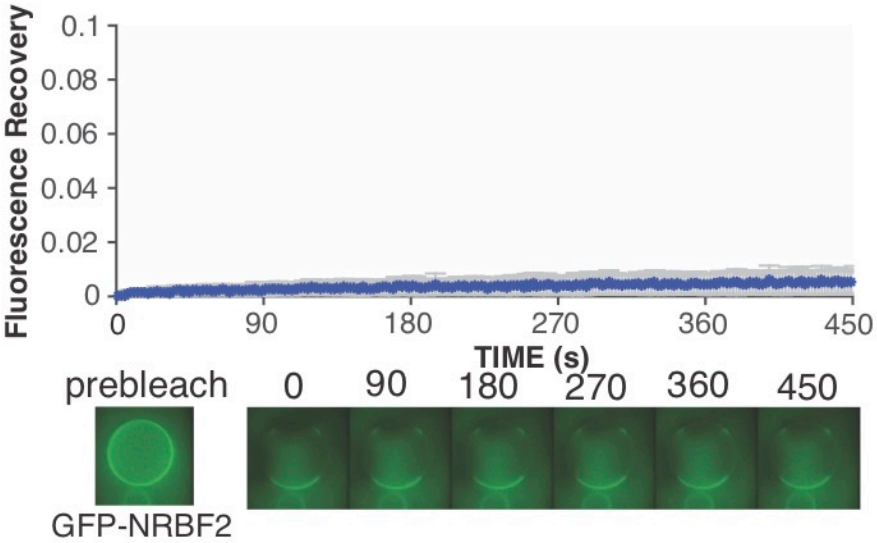

Figure 2.1: NRBF2 is a tightly bound subunit of PI3KC3-C1.
Quantitation of Fluorescence Recovery After Photobleaching (FRAP) of GFP-NRBF2 bound to PI3KC3-C1. Recovery was monitored at 2-second intervals for 450 seconds. PI3KC3-C1 is bound to StrepTactin resin through streptavidin protein binding (SPB) tags on PI3KC3-C1. Averages and SD of three replicates are shown.

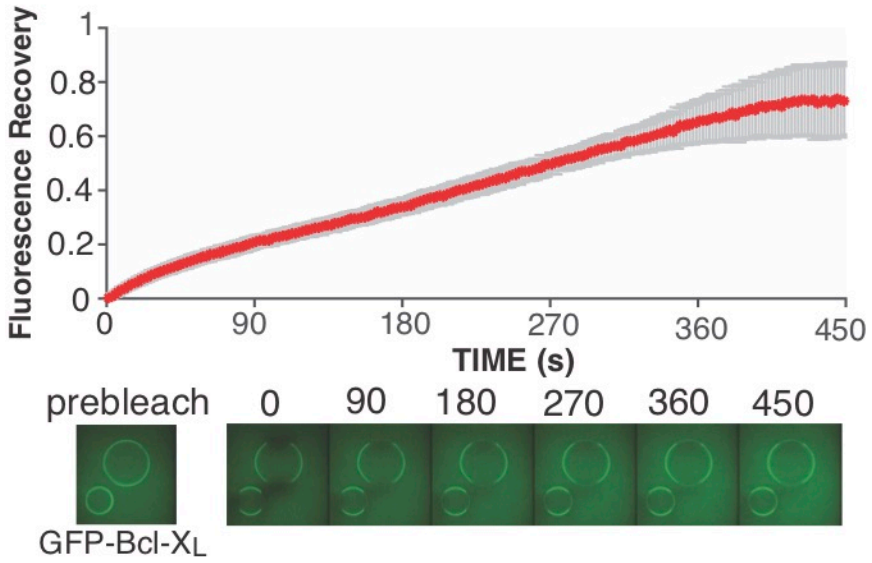

Figure 2.2 Bcl-XL is not tightly associated to PI3KC3-C1.
Quantitation of Fluorescence Recovery After Photobleaching of GFP- Bcl-$X_L^{\Delta TM}$ bound to SBP-PI3KC3-C1, recovery was monitored for 450 seconds. PI3KC3-C1 is bound to Strep-Tactin resin through streptavidin protein binding (SPB) tags on PI3KC3-C1. Averages and SD of three replicates are shown.

To determine the affinity of the interaction between full length NRBF2 and PI3KC3-C1, pull-down experiments were performed by titrating NRBF2 onto PI3KC3-C1-bound beads. PI3KC3-C1 was immobilized on streptavidin resin through streptavidin-binding peptides located on PI3KC3-C1 subunits (BECN1, VPS34, VPS15), and the amount of NRBF2 retained was measured through densitometry of an SDS-PAGE gel. On the basis of fits to these data, NRBF2 binds to complex I with a dissociation constant of 40 nM (Figure 2.3). The 50-fold higher affinity compared to Bcl-$X_L^{\Delta TM}$ was consistent with the inability of NRBF2 to exchange from PI3KC3-C1 containing beads in FRAP experiments.

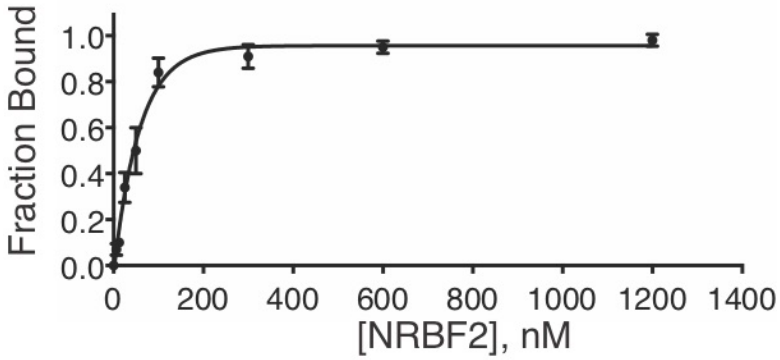

Figure 2.3: NRBF2 binds to PI3KC3-C1 with 40 nM affinity
Binding curve of the average of three independent binding assays, displayed with the standard error of the mean (SEM) shows the binding affinity to be 40 nM.

2.3.2 NRBF2 dimerizes PI3KC3-C1

Size Exclusion Chromatography (SEC) with full length NRBF2 and PI3KC3-C1 indicates that it dimerizes in solution. This is consistent with the finding that Atg38, the *S. cerevisiae* homolog of NRBF2, is a homodimer on the basis of analytical ultracentrifugation (Araki et al. 2013). The central and C-terminal region must be responsible for dimerization, as a truncation of NRBF2 at residue 159 NRBF2$^{\Delta CC}$ was monomeric in solution on the basis of MALS analysis (Figure 2.5). When PI3KC3-C1 is mixed with NRBF2 and subject to size exclusion chromatography, the elution peak shifts from 13.6 ml, consistent with molecular weight standard of 440 kDa to 11.2 ml, which is larger than the 669 kDa molecular weight standard (Figure 2.4). This indicates that the presence of NRBF2 leads to formation of a larger complex.

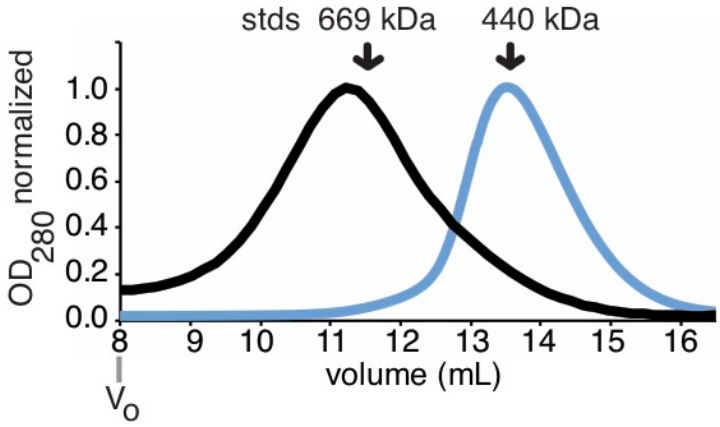

Figure 2.4 NRBF2 can dimerize PI3KC3-C1

Size-exclusion chromatography with PI3KC3-C1+NRBF2 (black trace) and PI3KC3-C1 (blue trace). The peak shifts from 13.6 ml to 11.2 ml on a Superose 6 10/30 column. Molecular weight standards are indicated.

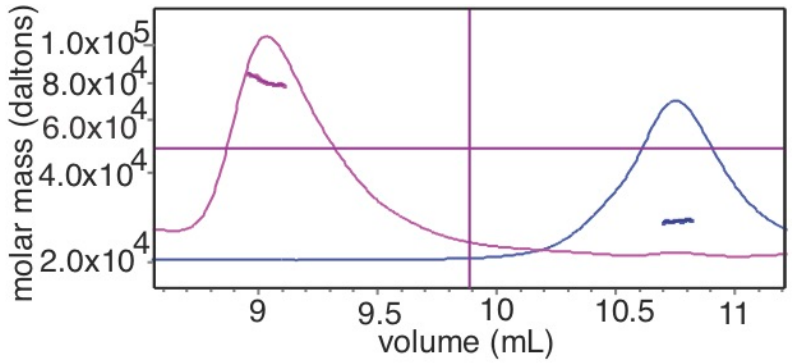

Figure 2.5 NRBF2 is a dimer

Multi-angle Light Scattering (MALS) of full length NRBF2 (pink trace) and NRBF2$^{\Delta CC}$ (blue trace). Full length NRBF2 is 78 kDa and NRBF2$^{\Delta CC}$ is 27 kDa.

2.3.3 NRBF2 enhances PI3KC3-C1 kinase activity

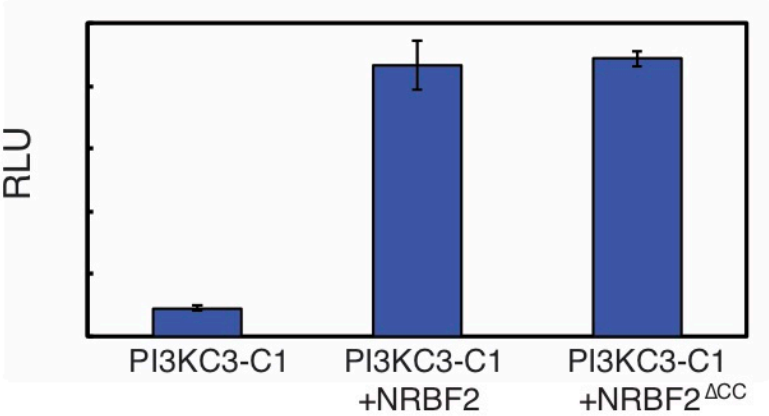

Figure 2.6 MIT domain of NRBF2 enhances PI3KC3-C1 kinase activity
In vitro activity assay using sonicated liposomes containing phosphatidylinositol with PI3KC3-C1 and, where indicated, NRBF2 or NRBF2$^{\Delta CC}$. RLU refers to relative light units.

NRBF2 contains an N-terminal Microtubule Interacting and Trafficking (MIT) domain and a central coiled coil. The MIT domain spans residues 1-80, and the coiled coil spans residues 160-210. MIT domains are three-helix bundles, first well-studied in proteins of the ESCRT pathway, notably Vps4 (James H Hurley and Yang 2008). To determine if NRBF2 affects the catalytic activity of PI3KC3-C1, recombinant NRBF2 was incubated with purified PI3KC3-C1. The activity was assessed on sonicated liposomes (approximately 50-100 nm) containing 22 μM substrate phosphatidylinositol (PI). Addition of NRBF2 enhanced the catalytic activity of PI3KC3-C1 ten-fold in the presence of saturating amounts of NRBF2 (Fig. 2.6). A monomeric version of NRBF2 without its coiled-coil domain was equally capable of activating the complex, indicating the MIT domain is sufficient for activation (Fig 2.6). The activating effect of NRBF2 is thus separate from its ability to dimerize PI3KC3-C1. These *in vitro* data are in agreement with a previous report that found that the coiled-coil was dispensable for the interaction between NRBF2 and PI3KC3-C1 in cells by immuno-precipitation (Lu et al. 2014). The data show that NRBF2-MIT is necessary and sufficient for activation of PI3KC3-C1.

2.3.4 Mapping binding sites via Hydrogen-Deuterium Exchange Mass Spectrometry

To probe the location of the NRBF2 subunit within PI3KC3-C1, and its effects on conformation and dynamics, HDX-MS experiments were performed on PI3KC3-C1 and on the complete PI3KC3-C1 including NRBF2. Peptide coverage was obtained for the majority of the 390 kDa PI3KC3-C1 complex. The peptide coverages for each subunit were VPS15 (81%), VPS34 (75%), BECN1 (62%), and ATG14 (51%) (Figure 2.7).

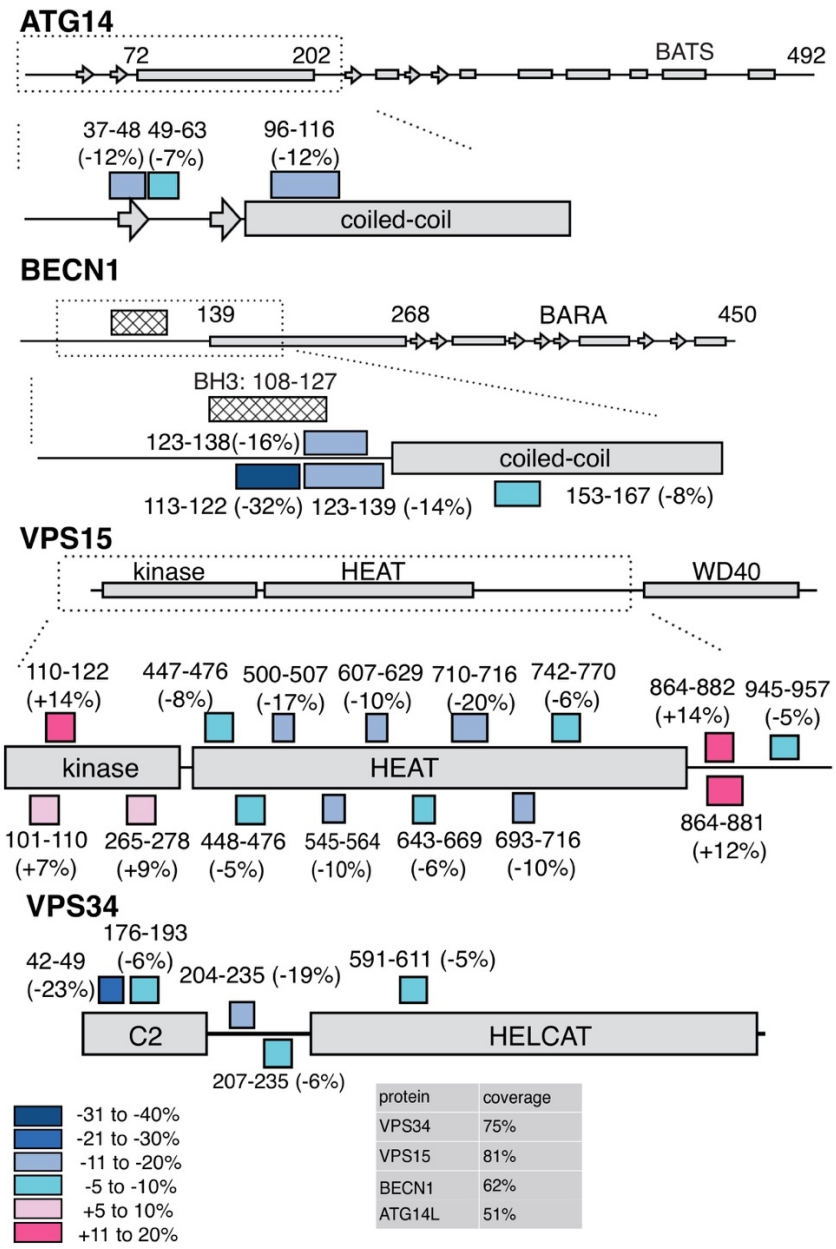

Figure 2.7 Global mapping of dynamics changes in the presence of NRBF2.
Hydrogen-Deuterium Exchange Mass Spectrometry (HDX-MS) was performed on PI3KC3-C1 and PI3KC3-C1+NRBF2 for 10 seconds and peptides showing a difference in exchange are noted on the secondary structure elements.

HDX labeling reactions proceeded for 10 seconds, which is sufficient to deuterate fully solvated amides (Molday, Englander, and Kallen 1972; Pantazatos et al. 2004). High quality peptides were analyzed, clearly separated from other peptides and inspected individually. HDX-MS analysis of PI3KC3-C1 is largely consistent with our previous analysis of VPS34 and VPS15 (Baskaran et al. 2014). All four subunits contained at least one peptide for which the percent hydrogen exchange changed by more than 10% in the presence of NRBF2

(Figure 2.7), indicating that inclusion of NRBF2 has wide-ranging consequences for the flexibility of PI3KC3-C1.

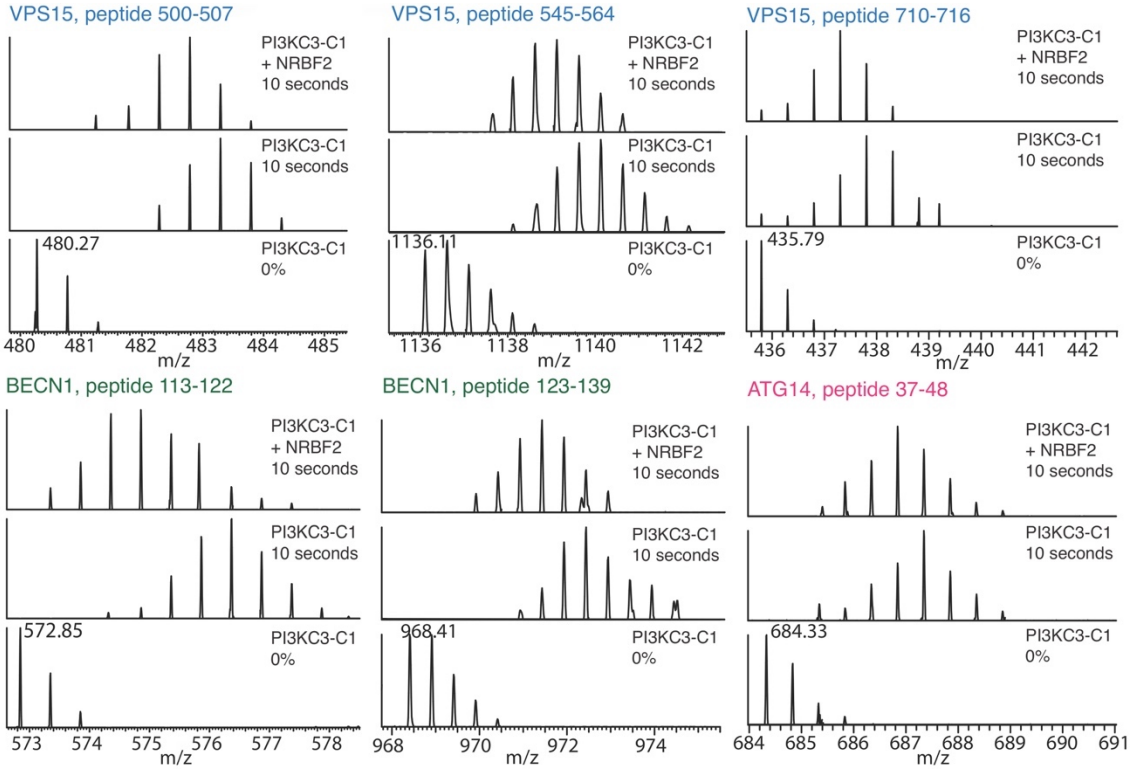

Figure 2.8 Sample peptides
Sample peptides from BECN1, VPS15, ATG14 showing a protection due to the presence of NRBF2. Bottom: PI3KC3-C1 0% control, middle: PI3KC3-C1 10 seconds D_2O, top: PI3KC3-C1+NRBF2 10 seconds D_2O.

While previous reports have established that Atg38/NRBF2's MIT domain binds to Atg14/ATG14 (Araki et al. 2013; Lu et al. 2014), the precise location was unknown. Atg14 has a central-coiled domain, but little is known about structure at either termini. The C-terminal membrane targeting region of ATG14 (Barkor/Atg14 autophagosome targeting sequence or BATS) is required for recruitment of PI3KC3-C1 to the autophagosomal membrane (Fan, Nassiri, and Zhong 2011). The following ATG14 peptides showed a reduction in exchange: N-terminus 38-48 (-12%), 49-63 (-7%), and coiled-coil domain: 98-116 (-12%). Multiple overlapping peptides from BECN1's coiled-coil domain showed a decrease in exchange due to NRBF2: 113-122 (-32%), 123-138 (-16%), 123-139 (-14%), 153-167 (-8%). ATG14 and BECN1 have a parallel orientation with respect to their coiled-coil domains, and both N-termini reside at the base of complex I (Baskaran et al. 2014). These large changes in the N-terminal regions of both ATG14 and BECN1 are consistent with a major effect on the dynamics of the base of the V-shaped complex when NRBF2 is present.
and the relative percent exchange are stated.

VPS15 contains an N-terminal serine/threonine protein kinase-homology domain, an alpha-helical HEAT repeat and a C-terminal WD40 domain (Heenan et al. 2009). The region that showed the most exchange within VPS15 is within the HEAT repeat, which serves as a scaffold to bridge the left regulatory arm (BECN1 and ATG14) and the right catalytic arm (kinase domains of VPS34 and VPS15; Fig. 2.8). Multiple peptides within the central HEAT repeat of VPS15 showed decreased deuterium incorporation in the presence of NRBF2: 447-476 (-8%), 448-476 (-5%), 501-507 (-17%), 545-564 (-10%), 607-629 (-10%), 643-669 (-6%), 693-716 (-10%), 710-716 (-20%), 742-770 (-6%) (Fig. 2, Fig. 3B, C). These peptides map to regions of the HEAT repeat found in the base of PI3KC3-C1. This indicates that the HEAT repeat of VPS15 becomes more protected in the presence of NRBF2 (Fig. 2.8).

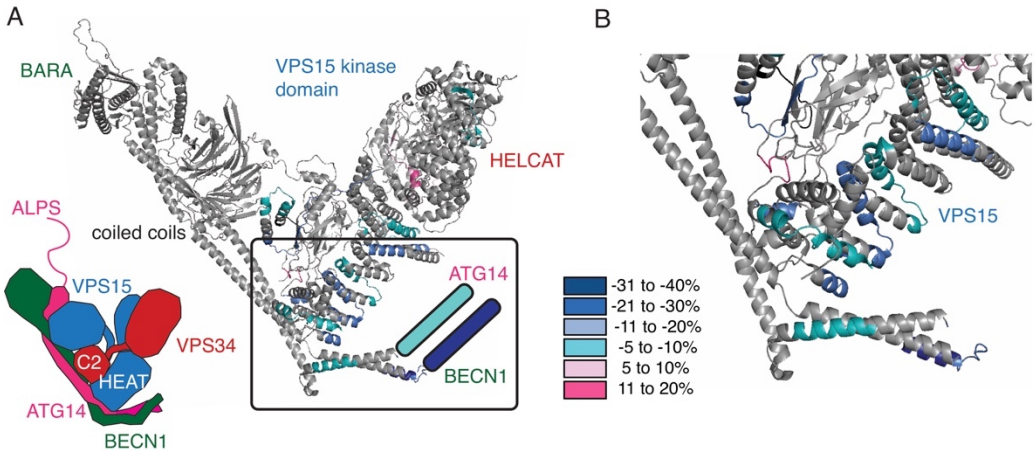

Figure 2.9 Mapping peptide changes to the base of the V.
(A) Peptides from PI3KC3-C1 showing a difference in exchange due to the presence of NRBF2 has been mapped onto the *S. cerevisiae* crystal structure of PI3KC3-C2. (B) Protection converges at the base of PI3KC3-C1.

The VPS15 kinase domain showed an increase in exchange in the following peptides: 102-110 (+7%), 101-109 (+5%) and 111-122 (+14%), these changes have been mapped to peptides that surround the VPS15 catalytic loop and activation loop (Fig. 2.9). The VPS15 HEAT-WD40 linker region shows differences in HD exchange: 864-881 (+12%), 864-882 (+14%), 945-957 (-5%). The corresponding peptides were not ordered in the yeast crystal structure and could not be mapped.

Finally, the catalytic subunit VPS34 showed differences in exchange. In the extreme N-terminus, there was an increase in exchange for peptide 13-39 (+18%). VPS34 contains an N-terminal C2 domain that, along with the HEAT repeats of VPS15, helps bridge the two arms of the complex. We observed changes in deuterium exchange in two VPS34-C2 peptides: 42-49 (-23%), and 176-193 (-6%). Two more peptides in the C2-HELCAT linker region decreased in exchange 204-235 (-19%) and 207-235 (-6%).

Within the lipid kinase domain, there was a decrease in exchange for a single peptide: 591-611 (-5%). This peptide lies on a distal face of the VPS34

kinase domain, facing away from the VPS15 kinase domain. The rest of the HELCAT was well-covered and peptides analyzed did not show differences in HD exchange greater than 5% either way.

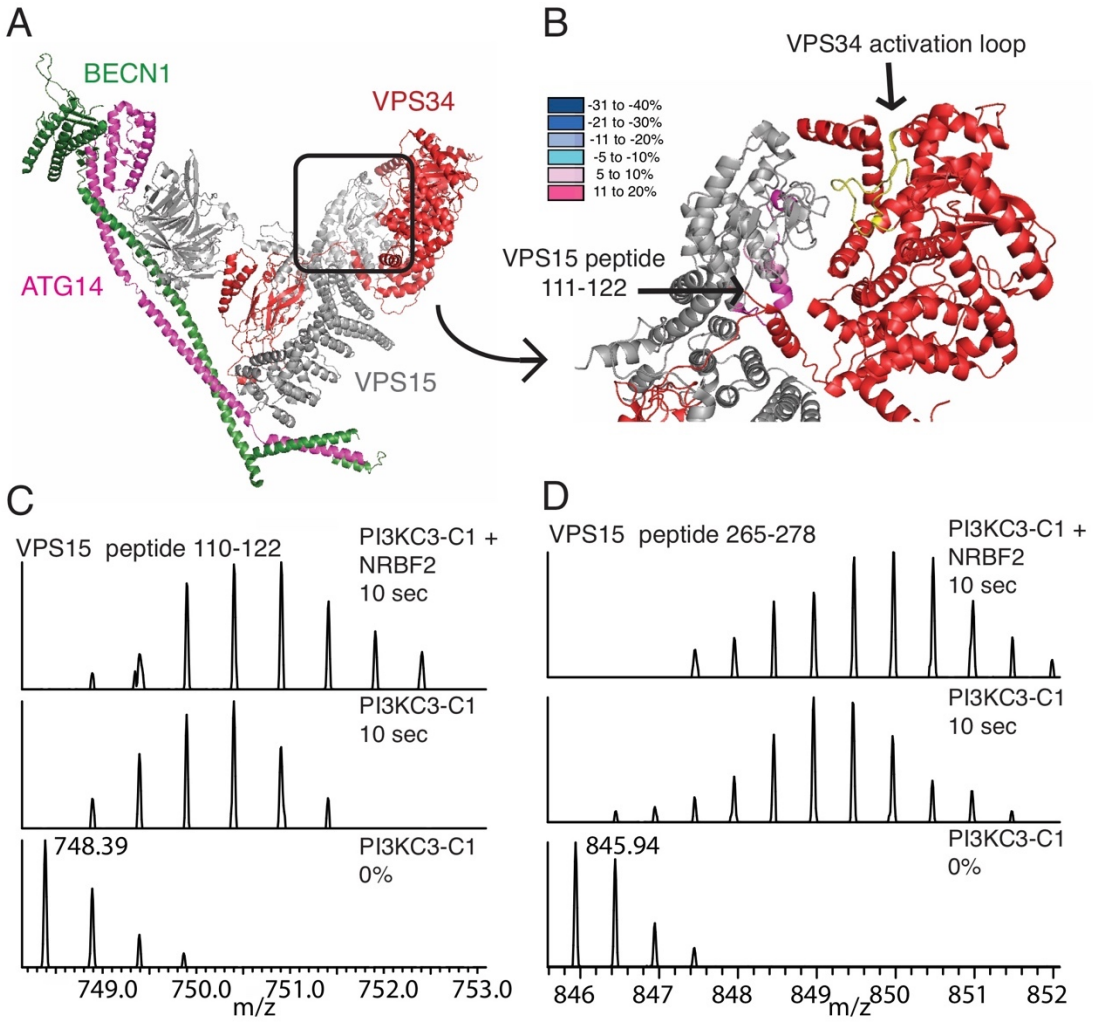

Figure 2.10 Dynamics changes in kinase domains.
(A) Crystal structure colored according to subunit, VPS15 (grey), VPS34 (red), BECN1 (green), ATG14 (pink). (B) Kinase domain of VPS15 (grey), kinase domain of VPS34 (red), activation loop of VPS34 (yellow) and peptides showing a decrease in protection due to NRBF2 (light pink and pink). (C) VPS15 peptide 110-122 (corresponds to yeast 110-120), bottom: PI3KC3-C1 0% control, middle: PI3KC3-C1 10 seconds D_2O, top: PI3KC3-C1+NRBF2 10 seconds D_2O. (D) VPS15 peptide 265-278 (corresponds to yeast 249-262) bottom: PI3KC3-C1 0% control, middle: PI3KC3-C1 10 seconds D_2O, top: PI3KC3-C1+NRBF2 10 seconds D_2O.

Overall, the base of the complex showed the greatest changes in exchange (Figure 2.7, 2.8). These data are strongly suggestive that NRBF2 binds at the base of PI3KC3-C1, but taken by themselves, they do not rule out that NRBF2 could bind elsewhere and allosterically trigger these changes. These experiments were carried out with full-length NRBF2 and therefore do not rule

out the possibility that these changes in exchange are due to PI3KC3-C1 dimerization.

2.3.5 Single particle EM reveals that NRBF2 is part of the base of PI3KC3-C1

Single particle negative stain electron microscopy (EM) was used to directly visualize the location of NRBF2 within the complex. In order to simplify the analysis, the monomeric construct NRBF2$^{\Delta CC}$ (Figure 2.11), which is necessary and sufficient for incorporation into the complex, was used. An N-terminal Maltose Binding Protein (MBP) tag genetically fused to NRBF2$^{\Delta CC}$ to aid in its identification. PI3KC3-C1 was used as a reference for 2D classification.

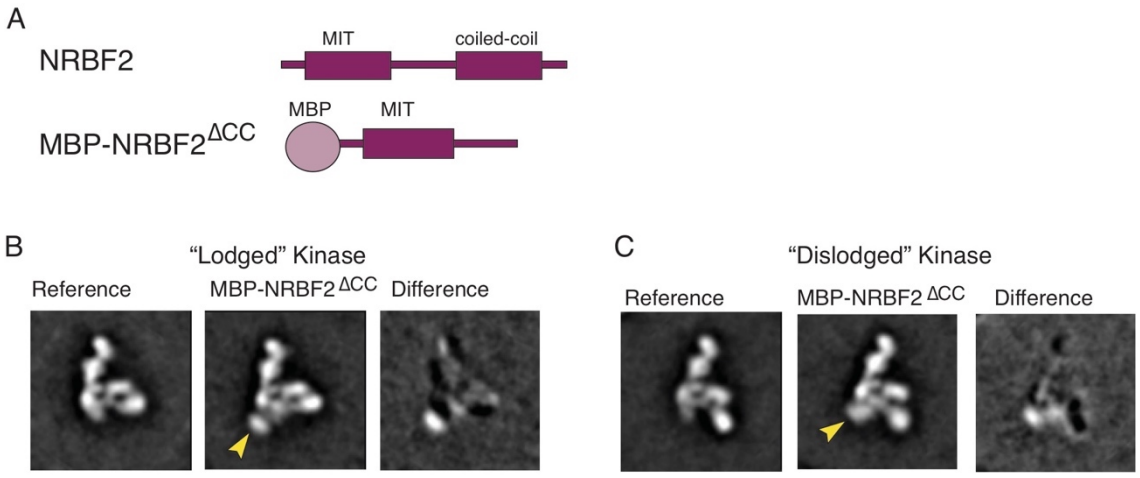

Figure 2.11 Negative stain EM mapping of the NRBF2 binding site.
(A) Cartoon of full-length NRBF2 and cartoon of MBP-tagged NRBF2$^{\Delta CC}$. (B) Left: Electron microscopy 2D reference projection group of PI3KC3-C1 with kinase domain of VPS34 in the lodged position. Middle: 2D projection groups of PI3KC3-C1 with MBP-NRBF2$^{\Delta CC}$ bound. Arrows indicate additional density Right: 2D difference maps showing density for MBP-NRBF2$^{\Delta CC}$. (C) Left: Electron microscopy 2D reference projection group of PI3KC3-C1 with kinase domain of VPS34 in the dislodged position. Middle: 2D projection groups of PI3KC3-C1 with MBP-NRBF2$^{\Delta CC}$ bound. Arrows indicate additional density Right: 2D difference maps showing density for MBP-NRBF2$^{\Delta CC}$.

Of the 49,339 particles were picked, 18,398 particles (37%) contained extra density corresponding to the globular MBP tag (Fig. 2.11). A difference map was calculated by subtracting the unlabeled reference group (PI3KC3-C1) from the labeled group (PI3KC3-C1+MBP-NRBF2$^{\Delta CC}$) to localize additional density attributed for the MBP tag. Two-dimensional projections showed when NRBF2$^{\Delta CC}$ is bound, the VPS34 kinase domain can adopt both the lodged and dislodged conformations (Fig. 2.11), as previously seen for PI3KC3-C1 (Baskaran et al. 2014).

2.4 Discussion

We found that NRBF2 binds with very high affinity to the rest of the PI3KC3-C1. Once bound, NRBF2 is non-exchangeable on the time scale of our experiment. This is consistent with the concept, from cell-based studies, that NRBF2 is a fifth core subunit of the active form of mammalian PI3KC3-C1 (Lu et al. 2014; Cao et al. 2014; Y. Zhong et al. 2014), as found also for yeast Atg38 (Araki et al. 2013). In vitro, we find that NRBF2 potently activates the lipid kinase activity of PI3KC3-C1. This is also consistent with the loss-of-function phenotype seen in *atg38Δ* yeast cells (Araki et al. 2013), NRBF2$^{-/-}$ MEFs (Lu et al. 2014), and NRBF2-siRNA-treated HEK293T cells (Cao et al. 2014).

Both direct observation by negative stain EM, and the selective localization of dynamic changes from HDX, map the NRBF2 binding site to the base of the PI3KC3-C1. The large changes in hydrogen exchange in the N-termini of both BECN1 and ATG14 suggest that both are involved in direct contacts with NRBF2. It is interesting that the C2 domain of UVRAG (or Vps38 in yeast) occupies essentially the same location in the overall architecture (Baskaran et al. 2014; Rostislavleva et al. 2015). Perhaps there could be some redundancy in the roles of the NRBF2 MIT domain and the UVRAG C2 domain. The largest of all of the changes in HDX protection correspond to the BH3 region of BECN1, the binding site for Bcl-2 (Oberstein, Jeffrey, and Shi 2007). It remains to be determined to what extent there is interplay between the binding of Bcl-2 family members and NRBF2 isoforms.

Outside of the immediate vicinity of the NRBF2 binding site, the largest changes in dynamics occur in the VPS15 kinase domain. The most affected portion of the VPS15 kinase domain is close to the VPS34 HELCAT domain and forms an interface that includes the activation loop and catalytic site of the VPS34 lipid kinase domain. This suggests an attractive mechanism for NRBF2 enhancement of kinase activity via modulation of the VPS15-VPS34 interface. However, we did not observe changes in HDX protection in the VPS34 lipid kinase domain above the 5% threshold. The regions of VPS34 involved in catalysis were covered in the study. The structural basis for the increased activity of the NRBF2-containing PI3KC3-C1 complex remains to be elucidated.

Probably the clearest and most significant implication of these results is that PI3KC3-C1 functions as a decamer (dimer of pentamers). Dimerization has important consequences for the mode with which PI3KC3-C1 can interact with membranes. For example, oligomers of the ATG14 subunit have been proposed for tether vesicles (Diao et al. 2015). However the monomeric four-subunit PI3KC3-C1 has not been shown to have this property, and direct evidence for the existence of functional endogenous ATG14 homooligomers has been lacking. The discovery that the complete PI3KC3-C1 does in fact contains two copies of ATG14 suggests how tethering could in principle occur in the context of the fully assembled decameric complex (Fig. 2.12).

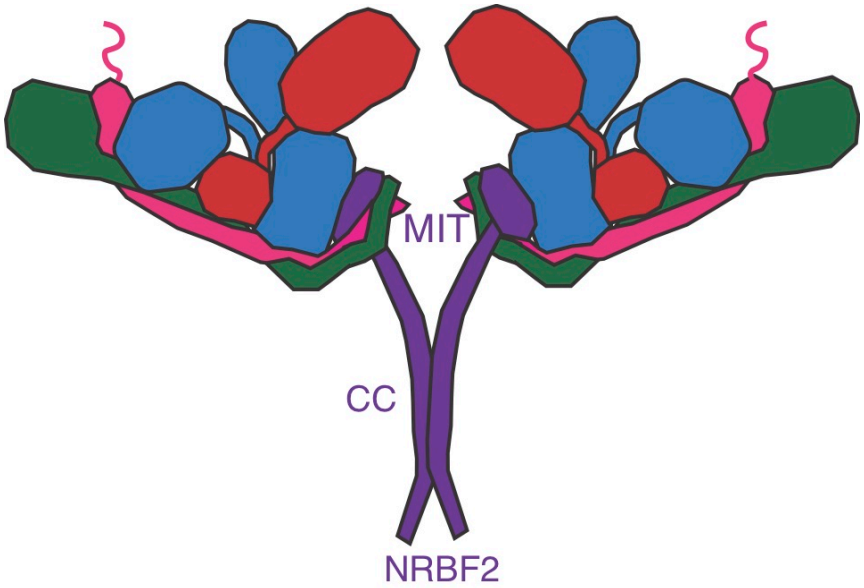

Figure 2.12 Dimeric PI3KC3-C1 containing NRBF2.
NRBF2 binds to the base of PI3KC3-C1, and induces dimerization through its central coiled-coil domain.

Membrane tethering by a dimeric form of an autophagy initiation complex has a precedent, the yeast Atg1 complex. Atg1 is capable of dimerizing and tethering membranes through its C-terminal EAT domain (Ragusa, Stanley, and Hurley 2012). The Atg1 complex can also form higher order structures that may contribute to scaffolding phagophore biogenesis (Köfinger et al. 2015). Perhaps, as seen for the Atg1 complex, PI3KC3-C1 can form higher order structures on membranes and contribute in non-catalytic ways to phagophore initiation. The discovery that the NRBF2-containing form of PI3KC3-C1 has a dimer-of-pentamer architecture provides a stepping-stone towards better understanding these complex events.

2.5 Materials and methods

2.5.1 Purification of NRBF2 and NRBF2$^{\Delta coiled\text{-}coil}$

The full length DNA encoding NRBF2 was cloned into vectors 1M (Addgene #29565), generating His6-MBP-TEV-NRBF2 and vector 1GFP, generating His6-GFP-TEV-NRBF2. Vectors were obtained from (QB3 Macrolab, UC Berkeley). The NRBF2 truncation construct was subcloned into the vector 1M, generating His6-MBP-TEV-NRBF2$^{\Delta CC}$. BL21 DE3 competent cells were transformed with NRBF2 constructs. Cells were cultured to an OD_{600} of 0.6-0.8 in the presence of kanamycin (0.05 mg/ml) and induced with 0.2 mM IPTG for 3 hours at 37˚C. Cell pellets were resuspended in 50 mM HEPES pH 8.0, 200 mM NaCl, 1 mM TCEP, 1 mM PMSF (dissolved in ethanol) and sonicated on ice. Lysates were clarified by centrifugation (18,000g for 60 minutes, 4C). The supernatant was incubated with TALON resin, CloneTech (His6-GFP-TEV-NRBF2) or Amylose resin, New England BioLabs (His6-MBP-TEV-NRBF2Δcoiled-coil) for 1.5 hours. Protein was

eluted with 300 mM Imidazole (His6-GFP-TEV-NRBF2) or 30 mM Maltose (His6-MBP-TEV- NRBF2$^{\Delta CC}$). His6-MBP-TEV- NRBF2$^{\Delta CC}$ was concentrated with a 10 kDa MWCO Amicon concentrator and injected over a Superdex-200 column (GE Healthcare) equilibrated in 20 mM HEPES pH 8.0, 200 mM NaCl, 2 mM $MgCl_2$, 1 mM TCEP. Eluted His_6-GFP-TEV-NRBF2 or His6-TEV-NRBF2 was further purified through anion exchange chromatography, the samples were passed over a HiTrap Q 5 ml Fast Flow column (GE Healthcare) and eluted with an increasing NaCl gradient (20 mM to 1 M). Eluted His6-GFP-TEV-NRBF2 or His6-TEV-NRBF2 was concentrated with a 10 kDa MWCO Amicon concentrator and injected over a Superfex-200 column (GE Healthcare) equilibrated in 20 mM HEPES pH 8.0, 200 mM NaCl, 2 mM $MgCl_2$, 1 mM TCEP.

2.5.2 Purification of PI3KC3-C1

The full length DNAs encoding VPS15, VPS34, and BECN1 were codon optimized for expression in HEK293 cells as previously described (Baskaran et al. 2014). WT ATG14 was cloned into a pCAG vector with GST-tag and used for kinase assays. A truncation of ATG14 lacking the last 11 amino acids was similarly cloned into a pCAG vector containing a GST tag (generating GST-ATG14$^{\Delta ALPS}$) and used for HDX-MS, EM, and SEC studies. Cells were lysed by gentle shaking in lysis buffer (50 mM HEPES, pH 8.0, 200 mM NaCl, 2 mM $MgCl_2$, 10% (vol/vol) glycerol, 1% (vol/vol) Triton X-100, 1 mM TCEP, and EDTA free proteinase inhibitors (Roche, Basel, Switzerland) and supplemented with phosphatase inhibitors (10 mM B-glycerophosphate, 5 mM Sodium Pyrophosphate, 0.5 mM Sodium Orthoavanade, 50 mM NaF) at 4°C. Lysates were clarified by centrifugation (18,000×g for 60 min at 4°C) and incubated with glutathione Sepharose 4B (GE Healthcare, Uppsala, Sweden), applied to a gravity column, washed, and purified complexes were eluted with 50 ml wash buffer containing 50 mM reduced glutathione. Eluted complexes were treated with TEV protease at 4°C overnight. TEV-treated complexes were loaded on a 2.5 ml Strep- Tactin Sepharose gravity flow column (IBA GmbH, Göttingen, Germany; at 4°C). The Strep-Tactin Sepharose column was washed, and purified complexes were eluted with wash buffer containing 10 mM desthiobiotin (Sigma-Aldrich, St. Louis, MO). Eluted complexes were purified to homogeneity by injection on Superose 6 16/50 (GE Healthcare) column that was equilibrated in gel filtration buffer (20 mM HEPES, pH 8.0, 200 mM NaCl, 2 mM $MgCl_2$, and 1 mM TCEP).

2.5.3 Purification of GFP-Bcl-$X_L^{\Delta TM}$

A solube version of *H. sapiens* Bcl-X_L lacking the transmembrane domain (Bcl-$X_L^{\Delta TM}$) was cloned into 1-GFP vector generating His6-GFP-TEV- Bcl-$X_L^{\Delta TM}$. BL21 DE3 competent cells were transformed with the Bcl-$X_L^{\Delta TM}$ constructs. Cells were cultured to an OD_{600} of 0.6-0.8 in the presence of ampicillin (0.01 mg/ml) and induced with 0.2 mM IPTG for 3 hours at 37˚C. Cell pellets were resuspended in 50 mM HEPES pH 8.0, 200 mM NaCl, 1 mM TCEP, 1 mM PMSF (dissolved in ethanol) and sonicated on ice. Lysates were clarified by centrifugation (18,000g for 60 minutes, 4C). The supernatant was incubated with TALON resin,

CloneTech and protein was eluted with 300 mM Imidazole. Then, further purified through anion exchange chromatography, the samples were passed over a HiTrap Q 5 ml Fast Flow column (GE Healthcare) and eluted with an increasing NaCl gradient (20 mM to 1 M). Eluted His6-GFP-TEV- Bcl-$X_L{}^{\Delta TM}$ was concentrated with a 10 kDa MWCO Amicon concentrator and injected over a Superfex-200 column (GE Healthcare) equilibrated in 20 mM HEPES pH 8.0, 200 mM NaCl, 2 mM $MgCl_2$, 1 mM TCEP.

2.5.4 Electron microscopy sample preparation

Negatively stained samples of PI3KC3-C1 and PI3KC3-C1:MBP-NRBF2$^{\Delta CC}$ were prepared on continuous carbon grids that had been plasma cleaned in a 10% O2 atmosphere for 10 s using a Solarus plasma cleaner (Gatan Inc., Pleasanton, CA). 4 µl of PI3KC3-C1 at a concentration of 25 nM in 20 mM Tris, pH 8.0, 200 mM NaCl, 2 mM $MgCl_2$, 1 mM TCEP, and 3% trehalose were placed on the grids and incubated for 30 s. The grids were floated on four successive 50 µl drops of 1% uranyl formate solution incubating for 10 s on each drop. The stained grids were blotted to near dryness with a filter paper and air-dried.

2.5.5 EM data collection

Native PI3KC3-C1 and PI3KC3-C1: MBP-NRBF2$^{\Delta CC}$ samples were imaged using an FEI Tecnai 12 electron microscope (FEI, Hillsboro, OR) operated at 120 keV at a nominal magnification of 49,000 (2.18 Å calibrated pixel size at the specimen level) using a defocus range of −0.7 to −1.5 µm with an electron dose of 35e^{-}/Å^2. Images were acquired on a TVIPS TemCam F-416 4049 × 4096 pixel CMOS detector (TVIPS GmbH, Gauting, Germany) using the automated Leginon data collection software (Suloway et al. 2005).

2.5.6 Image processing

The initial steps of image processing and classification were performed using the Appion image processing environment (Lander et al. 2009). Template-based automated particle picking was performed using the FindEM program (Roseman 2004) with particles generated from previous 2D class averages (Baskaran et al. 2014). The contrast transfer functions (CTFs) of the micrographs were estimated using CTFFIND (Mindell and Grigorieff 2003). Particles were extracted using a 192 × 192 pixel box size and binned by a factor of 2. Particles were automatically selected from micrographs and subjected to 2D reference-free classification by iterative multi-reference alignment (MRA) (Ogura, Iwasaki, & Sato, 2003). EMAN2 (Tang et al. 2007) was used to find additional density attributed to MBP was visualized by creating a difference map calculated by subtracting the unlabeled reference group (PI3KC3-C1) from the labeled group (PI3KC3-C1:MBP-NRBF2$^{\Delta CC}$).

2.5.7 HDX-MS

Amide hydrogen exchange mass spectrometry (HDX-MS) was initiated by a 20-fold dilution of stock PI3KC3-C1 (2 µM) or PI3KC3-C1 (2 µM) and full-length NRBF2 (5 µM) into D_2O buffer containing 20 mM HEPES (pD 8.0), 200 mM

NaCl, 2 mM $MgCl_2$, and 1 mM TCEP at 30°C. Incubations in deuterated buffer were performed for 10 seconds. Backbone amide exchange was quenched at 0°C by the addition of ice-cold quench buffer (400 mM KH_2PO_4 /H_3PO_4, pH 2.2). Quenched samples were injected onto a chilled HPLC setup with in-line peptic digestion and desalting steps. Desalted peptides were eluted and directly analyzed by an Orbitrap Discovery mass spectrometer (Thermo Scientific, Waltham, MA). The HPLC system was extensively cleaned between samples. Initial peptide identification was performed via tandem MS/MS experiments. A PEAKS Studio 7 (www.bioinfor.com) search was used for peptide identification. Initial mass analysis of the peptide centroids was performed using HDExaminer version 1.3 (Sierra Analytics, Modesto, CA), followed by manual verification of each peptide. The deuteron content of the peptic peptides covering PI3KC3-C1 was determined from the centroid of the molecular ion isotope envelope. The deuteron content was adjusted for deuteron gain/loss during pepsin digestion and HPLC.

2.5.8 Lipid kinase assay

ATP consumption in the presence of lipids was determined using the ADP-Glo Kinase Assay kit (Promega, Madison, WI). The kinase reaction was performed in 96-well NBS white plates (Corning, Corning, NY), in 1.25× kinase reaction buffer (12.5 mM HEPES, pH 7.0, 125 mM NaCl, 2.5 mM $MnCl_2$). Samples were PI3KC3-C1 (20 nM), PI3KC3-C1 (20 nM) and NRBF2 (500 nM), PI3KC3-C1 (20 nM) and NRBF2$^{\Delta CC}$ (500 nM). The reaction was initiated by adding 5 µl of 125 µM ATP to 20 µl of 1.25× kinase reaction buffer. The reaction was carried out for 30 minutes at 23°C, then 25 µl of ADP-Glo reagent containing 10 mM $MgCl_2$ was added to the reaction mixture and incubated at 23°C for 30 min to stop the enzyme reaction and deplete unconsumed ATP. After depletion of ATP, 50 µl of Kinase Detection Reagent was added to convert ADP to ATP and to introduce luciferase and luciferin for ATP detection. The reaction mixture was further incubated 23°C for 30 min and the luminescence was measured with a GloMax-Multi detection system (Promega).

2.5.9 Size exclusion chromatography with multiangle light scattering (SEC-MALS)

The final concentration of NRBF2 used for SEC-MALS was 125 µM (4 mg/ml) and the final concentration of NRBF2$^{\Delta CC}$ for SEC-MALS was 160 µM (3 mg/ml). SEC-MALS experiments were performed using an Agilent 1200 high performance liquid chromatography system (Agilent Technologies, Santa Clara, CA) coupled to a Wyatt DAWN HELEOS-II MALS instrument and a Wyatt Optilab rEX differential refractometer (Wyatt, Santa Barbara, CA). For chromatographic separation, a WTC-050S5 size-exclusion column (Wyatt) with a 20-ml sample loop was used at a flow rate of 0.3 ml/min in 20 mM HEPES pH 7.4, 200 mM NaCl, 2 mM $MgCl_2$, 1 mM TCEP. The outputs were analyzed by ASTRA V software (Wyatt).

2.5.10 Fluorescence Recovery After Photobleaching (FRAP)

The FRAP experiments were performed by incubating 50 nM PI3KC3-C1 with Strep-Tactin Sepharose beads, and adding 1 μM GFP-NRBF2 or GFP- Bcl-$X_L^{\Delta TM}$. Defined areas on the beads' surface were photo-bleached using 75 mW laser coupled to a galvo FRAPPA device (Andor Instruments, Belfast, UK). Beads were imaged in confocal mode at two-second intervals before and after photo-bleaching. Fluorescence recovery was recorded for 450 seconds. Recovery curves were quantitated on a 0 to 1 scale, where pre-bleach intensity was normalized to 1 and initial post-bleach intensity was normalized to zero. Recoveries were calculated in MATLAB using an unbleached bead region for bleach control and performing background correction by subtracting the intensity of a non-bead region (MATLAB 8.5, The MathWorks Inc., Natick, MA, 2015).

CHAPTER 3:

NRBF2 activates PI3KC3-C1 via a two-part binding mechanism

Chapter 3 NRBF2 activates PI3KC3-C1 via a two-part binding mechanism

3.1 Summary

Autophagy is an evolutionarily conserved process requiring the autophagic-specific Class III Phosphatidylinsotiol-3 Kinase complex. Its activation by NRBF2 has been previously determined as well as the domain localization to the base of the complex where ATG14, BECN1 and VPS15 meet. Its ability to activate the lipid kinase of VPS34 via an allosteric mechanism had not been determined. This chapter shows precisely where the MIT domain of NRBF2 binds to PI3KC3-C1, that one copy of the MIT domain is insufficient for activation, and that full activation requires a second copy of the MIT domain. Dimeric NRBF2 cinches around the conformational flexible catalytic arm of the complex and stabilizes the lipid kinase domain of VPS34 and the putative kinase domain of VPS15.

3.2 Introduction

From a 28 Å reconstruction of human PI3KC3-C1 we learned that the complex has a V-shaped architecture with the lipid kinase domain on the right arm (Baskaran et al. 2014). The structure of yeast PI3KC3-C2 was improved by a crystal structure (4.5 Å), though lacking placement of side-chains and crystallization required stabilized by nanobodies, this structure showed that yeast and human complexes were highly conserved (Rostislavleva et al. 2015). A cryoEM reconstruction (6-8 Å) of human PI3KC3-C2 with inhibitory Rubicon fragment showed how Rubicon inhibited membrane binding through binding to the BECN1 BARA domain (Chang et al. 2019). However, we lack a high resolution structure of the autophagy-specific PI3KC3 complex.

Studies in yeast identified a PI3KC3-C1 interacting protein, called Atg38 (Araki et al. 2013). Atg38Δ cells displayed an autophagy defect and the authors reasoned that Atg38 enhanced PI3KC3-C1 complex integrity. The mammalian homolog of Atg38 is NRBF2 and subsequent studies in mammalian systems demonstrated it acted through PI3KC3-C1 and however, whether it functioned as pro-autophagy or anti-autophagy was controversial (Y. Zhong et al. 2014; Cao et al. 2014; Lu et al. 2014). In vitro research showed that purified NRBF2 binds tightly to PI3KC3-C1 at the base of the V-shaped complex and enhanced kinase activity through the N-terminal 3-helix bundle deemed the MIT domain (Microtubule Interacting and Trafficking motif) (L. N. Young et al. 2016). Although Atg38/NRBF2 are dimeric proteins, only NRBF2 was shown to dimerize PI3KC3-C1 (Ohashi et al. 2016; L. N. Young et al. 2016), however, the dimerization function is uncoupled from activation (L. N. Young et al. 2016).

We aimed to solve the structure of PI3KC3-C1 in the active state, since NRBF2 has been determined to be the most potent inducer of PI3KC3-C1, we pursued NRBF2 bound PI3KC3-C1 by cryoEM.

3.3 Results

3.3.1 Designing a five-subunit PI3KC3-C1 complex

In order to probe the active complex, a five subunit complex was generated by genetically fusing the N-terminal MIT domain of NRBF2 to the N-termini of BECN1 (MIT-linker-BECN1) and separated by a sequence encoding a flexible $(Gly\text{-}Gly\text{-}Ser)_4$ linkage, this linkage allows up to 42 Å of peptide extension as a random coil. The decision to fuse the N-termini of BECN1 was based on prior results from single particle negative stain EM studies and Hydrogen-Deuterium Exchange Mass Spectrometry (HDX-MS) (L. N. Young et al. 2016), see Chapter 2.

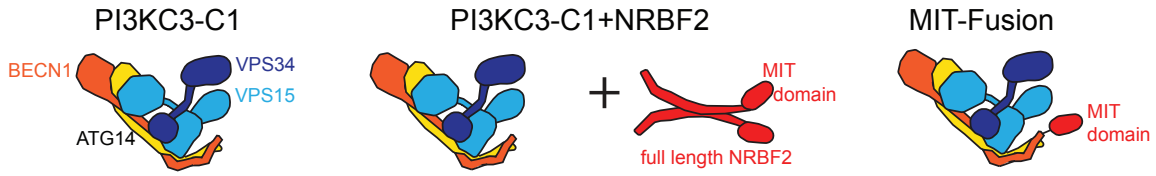

Figure 3.1 Schematic of MIT-Fusion Complex
Generation of the MIT-Fusion complex. The MIT-domain of NRBF2 was genetically fused to the N-terminus of BECN1.

3.3.2 Probing MIT-Fusion complex by HDX-MS

To confirm that the MIT-linker construct occupies the same binding site within PI3KC3-C1 as unfused NRBF2, we performed HDX-MS. Previously, we observed modest protection patterns in three subunits of PI3KC3-C1- ATG14, BECN1, and the solenoid of VPS15, indicating that NRBF2 binds to the base of the complex. In the MIT-Fusion complex, the same regions which previously showed only modest protection patterns instead showed an enhancement in protection, indicating that the presence of the MIT domain stabilizes PI3KC3-C1 (Figure 3.2-3.4).

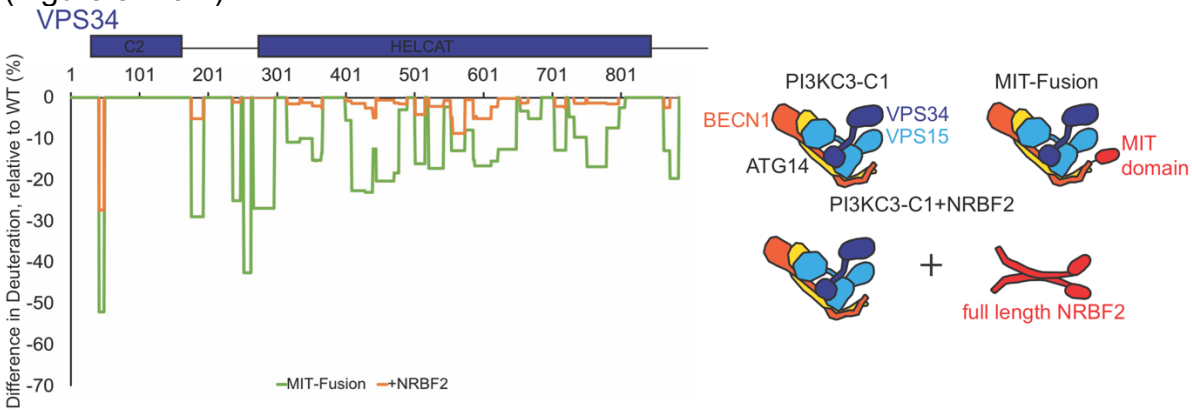

Figure 3.2 Difference in deuteration uptake plot for PI3KC3-C1 subunit VPS34
Shown above is a difference plot of the percent deuteration for PI3KC3-C1 subunit VPS34 in the apo-state relative to the addition of excess NRBF2 (orange), or when VPS34 is present in the MIT-Fusion complex (green).

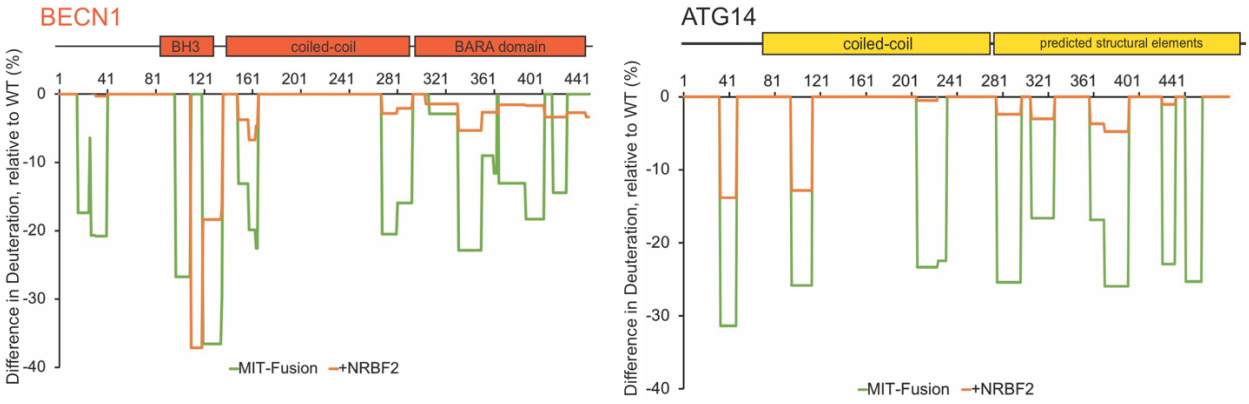

Figure 3.3: Difference in deuteration uptake plot for PI3KC3-C1 subunits BECN1 and ATG14

Difference plot of deuteration for two PI3KC3-C1 subunits, BECN1 and ATG14 in the apo-state when compared to excess NRBF2 (orange) and when these subunits are present in the MIT-Fusion complex (green).

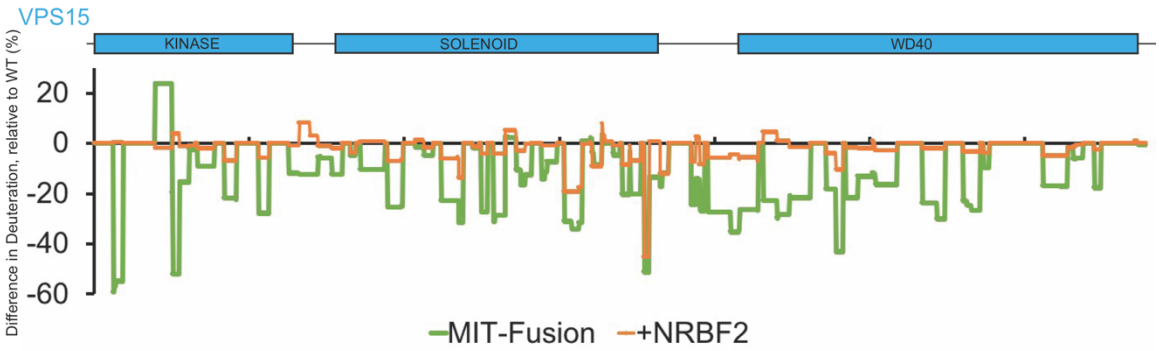

Figure 3.4 Difference in deuteration uptake plot for PI3KC3-C1 subunit VPS15

Difference plot of deuteration for two PI3KC3-C1 subunit VPS15 in the apo-state when compared to excess NRBF2 (orange) and when these subunits are present in the MIT-Fusion complex (green).

3.3.3 EM and CryoEM on MIT-Fusion Complex

Finally, the MIT-linker-BECN1 fusion does not alter the integrity of the complex as the MIT-Fusion complex visually looks like intact PI3KC3-C1 by negative stain EM (Figure 3.5).

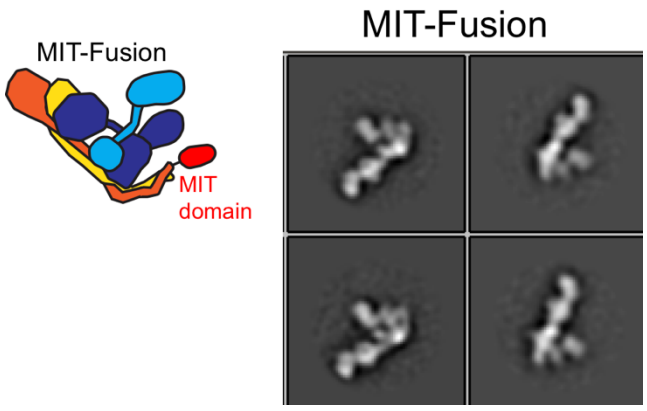

Figure 3.5 Negative stain EM on MIT-Fusion Complex
The MIT-Fusion complex by negative stain EM.

VPS34 is highly dynamic and capable of dislodging and extending up to 20 nanometers away from the core of PI3KC3-C1 (Baskaran et al. 2014). Moreover, its direct visualization by cryo-EM has been severely limited, these HDX results indicate that the MIT-Fusion complex would serve as a useful structural tool for investigating the autophagic specific PI3KC3-C1, of which we still lack a high resolution model.

We pursued single particle cryoEM on a complex containing VPS34:VPS15:ATG14:MIT-linker-BECN1. Two datasets were merged from a Titan Krios equipped with an energy filter and with a K2 camera, obtaining a resolution ranging from 6.5-8.5 Å (Figure 3.6) The cryoEM map agrees with the previous reports that human PI3KC3-C1 and -C2 possess an overall V-shaped architecture (Baskaran et al. 2014; Chang et al. 2019). The coordinates of the yeast crystal structure of PI3KC3-C2 can be flexibly fit into this cryoEM map (Rostislavleva et al. 2015).

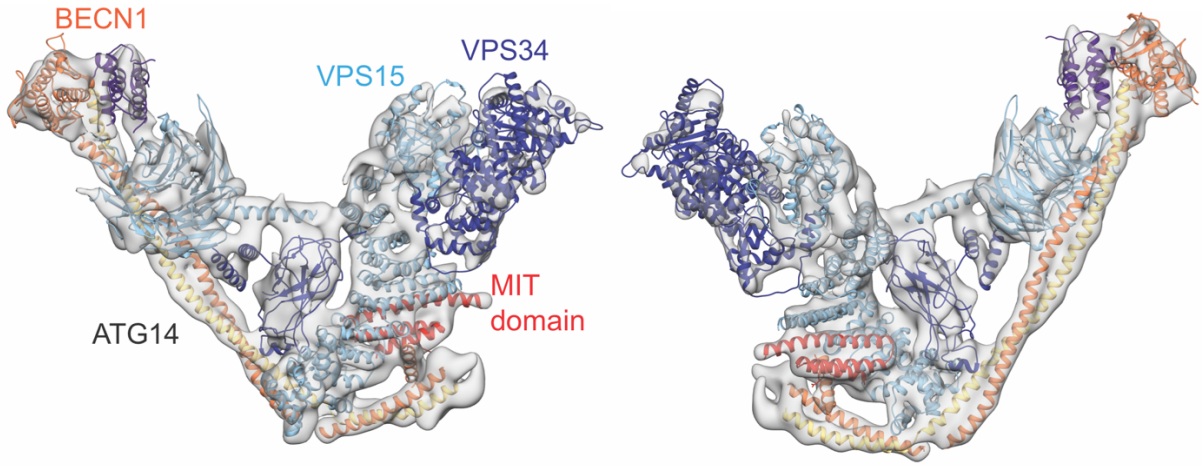

Figure 3.6 CryoEM on MIT-Fusion complex 1
Single particle cryo-EM reconstruction of MIT-Fusion complex 1.

Additionally, the cryo-EM map unambiguously fits the three helix bundle of the MIT domain (coordinates originate from a 1.5 Å crystal structure generated by the Joint Center for Structural Genomics). Surprisingly, the MIT domain forms a series of contacts with the central helices of the VPS15 solenoid (Figure 3.7). This large binding surface rationalizes the previously reported high affinity binding constant of 40 nM (L. N. Young et al. 2016).

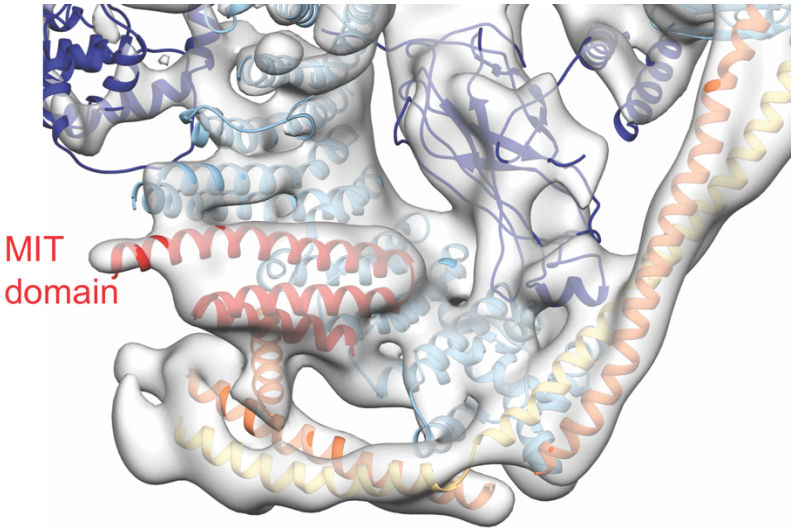

Figure 3.7 MIT domain of NRBF2 binds solenoid of VPS15
MIT domain 4ZEY fits within the cryoEM map of the MIT-Fusion complex.

However, since the MIT domain binds to the solenoid of VPS15, it doesn't explain NRBF2's specificity for PI3KC3-C1 over -C2, as the VPS15 solenoid is also present in PI3KC3-C2. Aligning the yeast crystal structure of PI3KC3-C2 with our model for the MIT-Fusion complex, it is apparent that the C2 domain of Vps38/UVRAG, the PI3KC3-C2 specific member would occlude the MIT binding site (Figure 3.8). In immunoprecipitation experiments, Atg38/NRBF2 was observed to only bind PI3KC3-C1, which contains ATG14 (Lu et al. 2014). This lead to the interpretation that NRBF2 binds to PI3KC3-C1 directly via an ATG14-dependent interaction. However, this cryoEM map shows that NRBF2's primary binding site on PI3KC3-C1 is the VPS15 solenoid and suggests that the C2 of UVRAG would block NRBF2 binding to PI3KC3-C2.

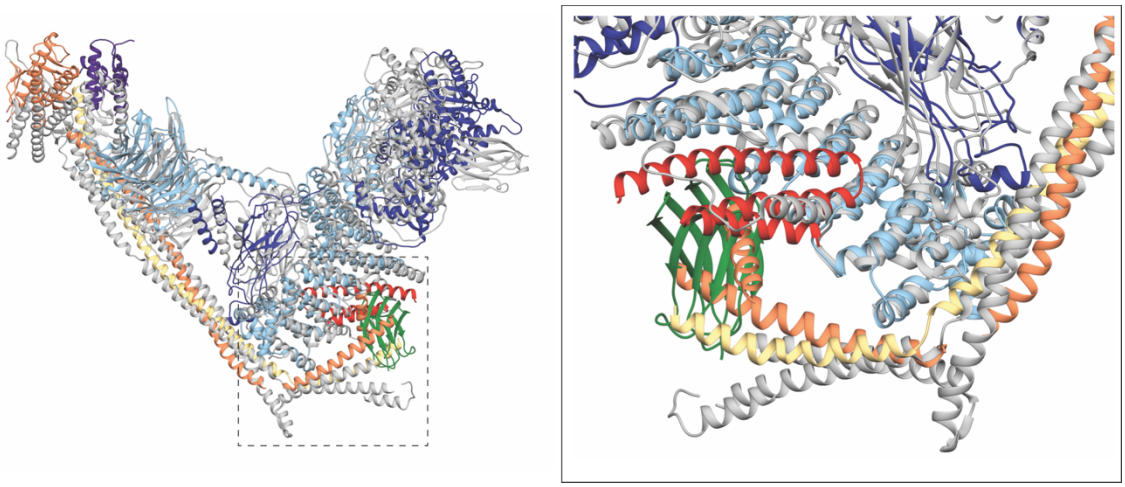

Figure 3.8 C2 domain of UVRAG occludes MIT NRBF2 binding site
PI3KC3-C2 (gray) contains UVRAG instead of ATG14. The C2 domain of UVRAG (green) would occlude the MIT domain of NRBF2 (red) from binding the VPS15 solenoid (light blue). Overlaid are PDB coordinates from yeast crystal structure 5DFZ and coordinates fitting the MIT-Fusion complex including homology models of 5DFZ and MIT crystal structure, 4ZEY.

Comparing PI3KC3-C1 and the MIT-Fusion, there are structural rearrangements within the base of the complex (Figure 3.9). The base of the complex is where a number of post-translational and regulatory signals converge on the autophagic specific PI3KC3-C1 via the “regulatory hub,” the N-termini of BECN1 and ATG14 (J.H. Hurley and Young 2017), see chapter 1. This is a site which is regulated by ULK1, AMPK, Bcl-2, among others. The presence of the MIT domain induces a structural rearrangement within the base of the complex (Figure 3.9). This agrees with HDX-MS experiments that show protection in ATG14 and BECN1 in the presence of NRBF2. Additionally, we can resolve the VPS34 catalytic domain, indicating that the MIT domain reduces the conformational flexibility of PI3KC3-C1 (Figure 3.6).

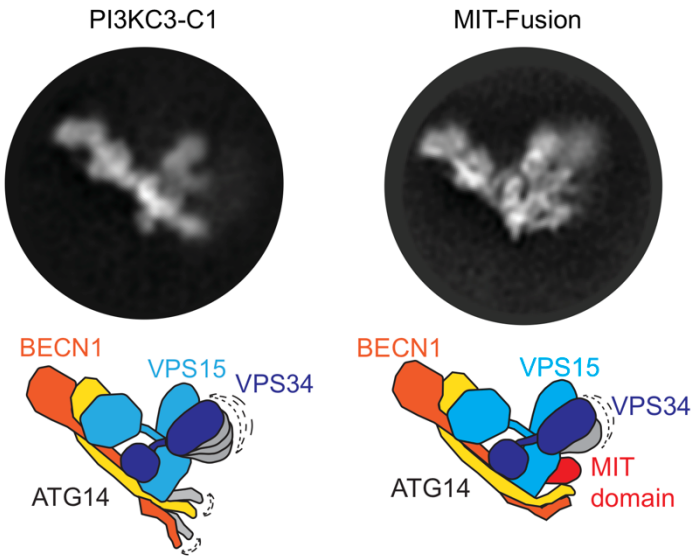

Figure 3.9 Comparison 2D class averages between PI3KC3-C1 and MIT-Fusion complex.

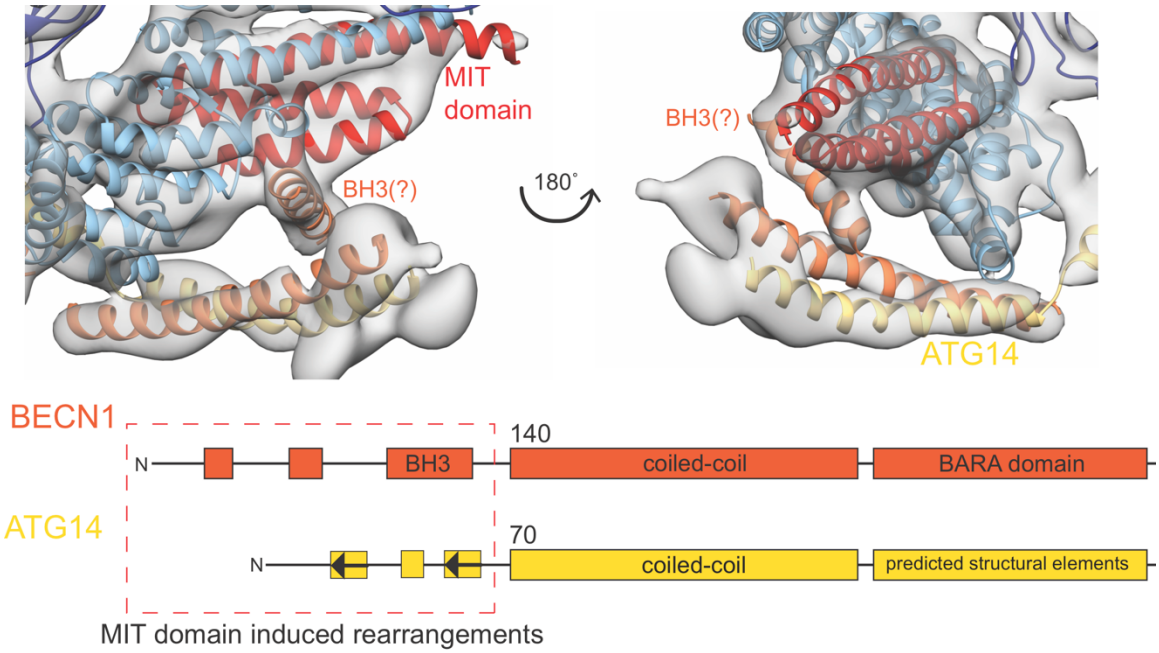

Figure 3.10 BECN1 helix, potentially the BH3 of BECN1, bound by NRBF2 MIT domain

A helix, possibly the BH3 of BECN1 is bound by the MIT domain of NRBF2. This helix is likely the BH3 of BECN1, due to the location central to the coiled-coil and the length of the helix, but this needs further evidence.

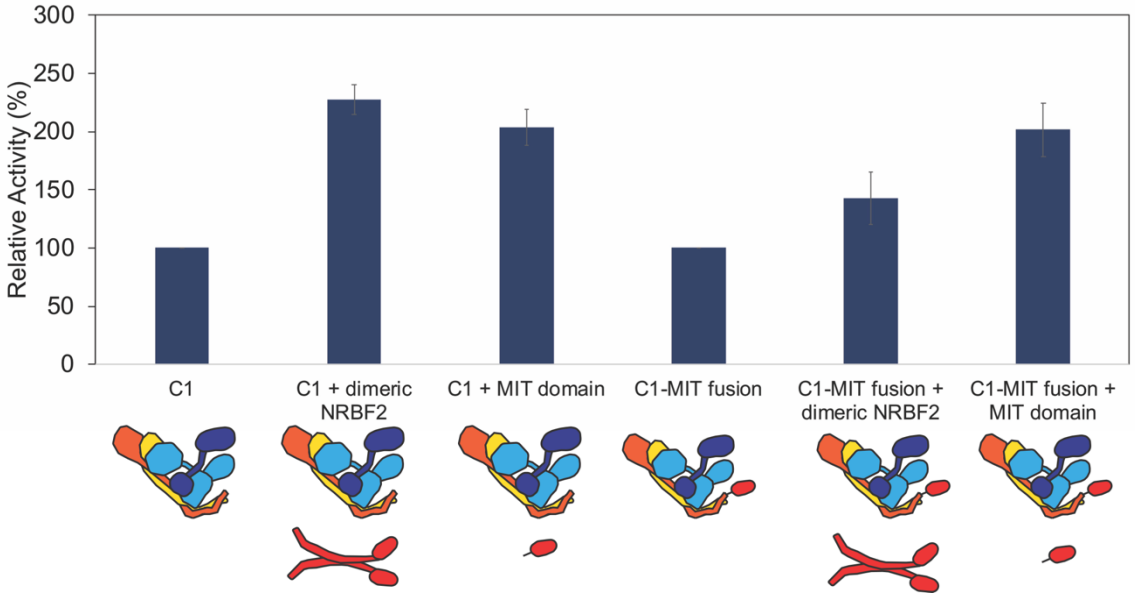

Figure 3.11 Two copies of NRBF2 activates PI3KC3-C1
Activity assay results of PI3KC3-C1 plus excess dimeric NRBF2 or MIT domain, compared to the MIT-Fusion complex plus excess dimeric NRBF2 or MIT domain. Results indicate that two copies of the MIT domain are required for PI3KC3-C1 activation.

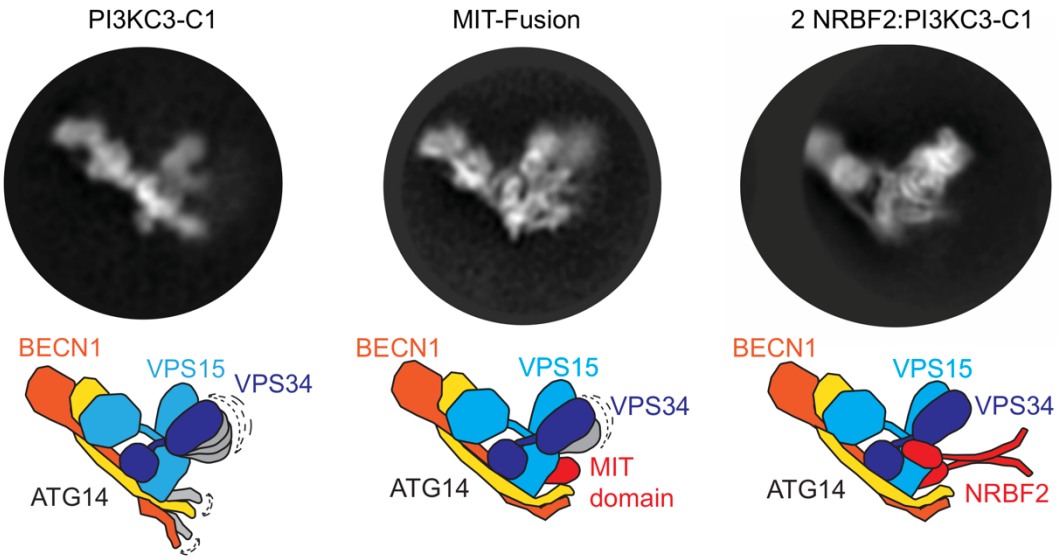

Figure 3.12 Comparisons of 2D class averages between PI3KC3-C1, MIT-Fusion complex, PI3KC3-C1 containing dimeric NRBF2
CryoEM based 2D class averages of PI3KC3-C1, MIT-Fusion complex, and PI3KC3-C1 and dimeric NRBF2.

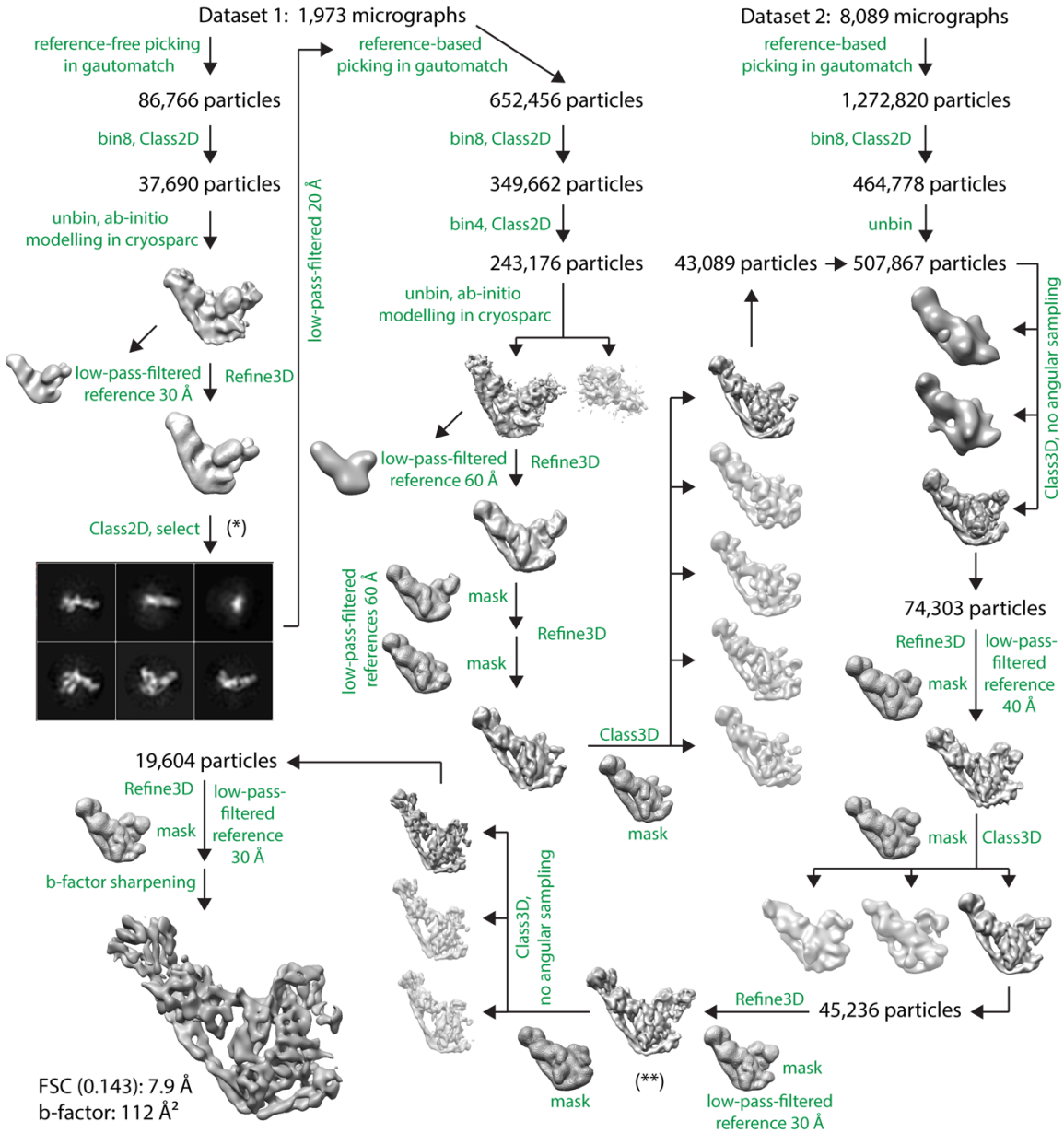

Figure 3.13 CryoEM workflow

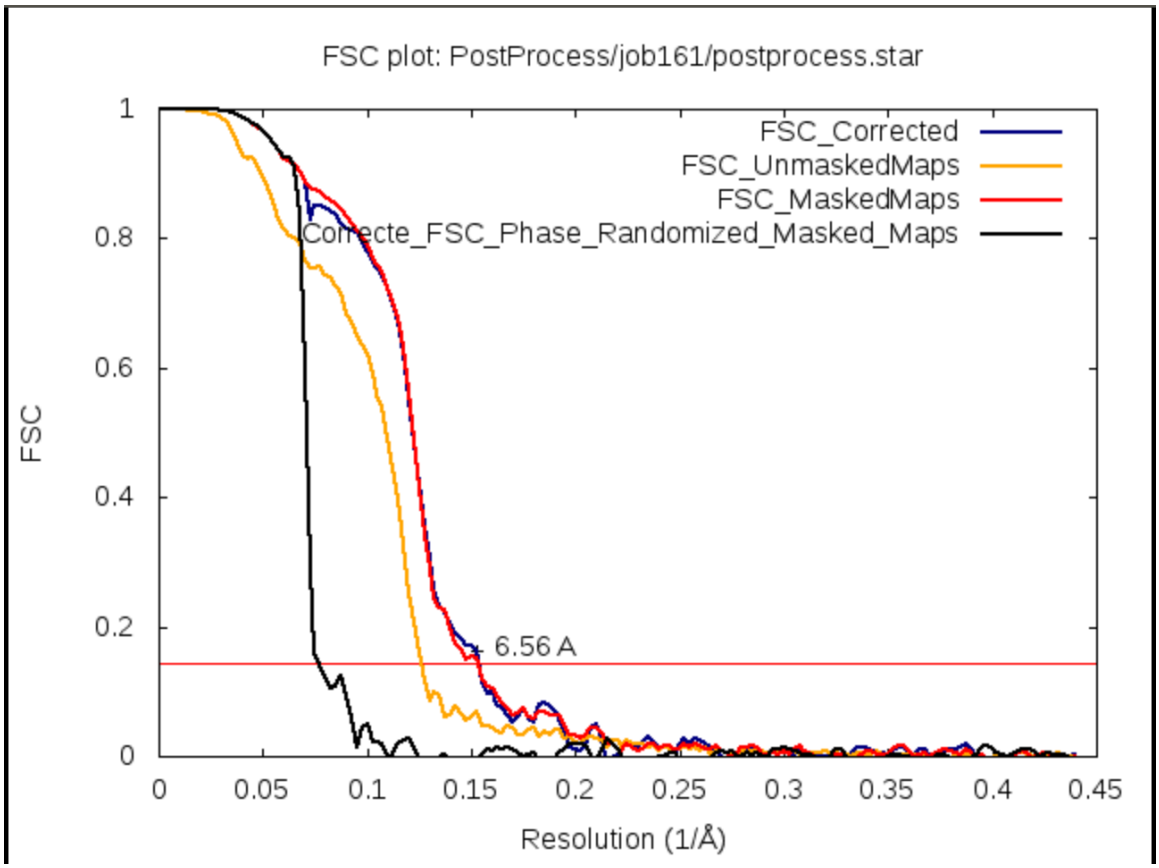

Figure 3.14 Resolution estimation of MIT-Fusion complex 1

3.4 Discussion

We have determined that dimeric NRBF2 binds and activates PI3KC3-C1. First, one N-terminal MIT domain of NRBF2 binds to the VPS15 solenoid. This MIT domain binds the same site which the C2 of UVRAG would occupy in PI3KC3-C2. The presence of the MIT domain within PI3KC3-C1 induces the conformationally flexible complex to adopt a more rigid conformation. However, one copy of the MIT domain does not enhance PI3KC3-C1 activity.

NRBF2 is a dimer, we and other reported that NRBF2 can dimerize two heterotetramers of PI3KC3-C1 (L. N. Young et al. 2016; Ohashi et al. 2016). The function of this larger complex oligomerization remains to be determined. Previously we determined that the monomeric MIT domain activates PI3KC3-C1 (L. N. Young et al. 2016). This led to the interpretation that one copy of the MIT domain per PI3KC3-C1 induced activation. Here, we further demonstrate that a second copy of the MIT domain of NRBF2 is required for activating PI3KC3-C1.

The mechanism of NRBF2 induced activation appears to be a stabilization of the entire complex, particularly of the right catalytic arm. NRBF2 as a dimer and wraps around the right arm, with one domain binding anterior of the VPS15 solenoid and a second domain binding posteriorly, assuming the viewer is taking the traditional face-on view of the V-shaped architecture of PI3KC3-C1. The result of this binding is a less conformationally flexible right arm, facilitating the

VPS34 lipid kinase domain and the putative VPS15 kinase domain to be in closer proximity.

I speculate that the BH3 domain of BECN1 is engaged when NRBF2 is present, due to the unattributed density for a helix at the base of the complex when the MIT domain is bound to VPS15. Its sequence identify cannot be determined at this resolution. The significance of the BECN1 BH3 helix engagement or protection while NRBF2 is bound implies that Bcl-2/Bcl-XL and NRBF2 are mutually exclusive binding partners.

3.5 Materials and methods

3.5.1 Purification of NRBF2 and NRBF2$^{\Delta coiled\text{-}coil}$

The full length DNA encoding NRBF2 was cloned into vectors 1M (Addgene #29565), generating His6-MBP-TEV-NRBF2 and vector 1GFP, generating His6-GFP-TEV-NRBF2. Vectors were obtained from (QB3 Macrolab, UC Berkeley). The NRBF2 truncation construct was subcloned into the vector 1M, generating His6-MBP-TEV-NRBF2$^{\Delta CC}$. BL21 DE3 competent cells were transformed with NRBF2 constructs. Cells were cultured to an OD_{600} of 0.6-0.8 in the presence of kanamycin (0.05 mg/ml) and induced with 0.2 mM IPTG for 3 hours at 37˚C. Cell pellets were resuspended in 50 mM HEPES pH 8.0, 200 mM NaCl, 1 mM TCEP, 1 mM PMSF (dissolved in ethanol) and sonicated on ice. Lysates were clarified by centrifugation (18,000g for 60 minutes, 4C). The supernatant was incubated with TALON resin, CloneTech (His6-GFP-TEV-NRBF2) or Amylose resin, New England BioLabs (His6-MBP-TEV-NRBF2Δcoiled-coil) for 1.5 hours. Protein was eluted with 300 mM Imidazole (His6-GFP-TEV-NRBF2) or 30 mM Maltose (His6-MBP-TEV- NRBF2$^{\Delta CC}$). His6-MBP-TEV- NRBF2$^{\Delta CC}$ was concentrated with a 10 kDa MWCO Amicon concentrator and injected over a Superdex-200 column (GE Healthcare) equilibrated in 20 mM HEPES pH 8.0, 200 mM NaCl, 2 mM $MgCl_2$, 1 mM TCEP. Eluted His_6-GFP-TEV-NRBF2 or His6-TEV-NRBF2 was further purified through anion exchange chromatography, the samples were passed over a HiTrap Q 5 ml Fast Flow column (GE Healthcare) and eluted with an increasing NaCl gradient (20 mM to 1 M). Eluted His6-GFP-TEV-NRBF2 or His6-TEV-NRBF2 was concentrated with a 10 kDa MWCO Amicon concentrator and injected over a Superfex-200 column (GE Healthcare) equilibrated in 20 mM HEPES pH 8.0, 200 mM NaCl, 2 mM $MgCl_2$, 1 mM TCEP.

3.5.2 Purification of PI3KC3-C1 and MIT-Fusion

The full length DNAs encoding VPS15, VPS34, and BECN1 were codon optimized for expression in HEK293 cells as previously described (Baskaran et al. 2014). WT ATG14 was cloned into a pCAG vector with GST-tag and used for kinase assays. A truncation of ATG14 lacking the last 11 amino acids was similarly cloned into a pCAG vector containing a GST tag (generating GST-ATG14$^{\Delta ALPS}$) and used for HDX-MS and EM studies. Cells were lysed by gentle shaking in lysis buffer (50 mM HEPES, pH 8.0, 200 mM NaCl, 10% (vol/vol) glycerol, 1% (vol/vol) Triton X-100, 10 mM TCEP, 0.11 micromolar NG311, and protease inhibitors at 4°C. Lysates were clarified by centrifugation (18,000×g for

60 min at 4°C) and incubated with glutathione Sepharose 4B (GE Healthcare, Uppsala, Sweden), applied to a gravity column, washed, and purified complexes were eluted with 50 ml wash buffer containing 50 mM reduced glutathione. Eluted complexes were treated with TEV protease at 4°C overnight. TEV-treated complexes were loaded on a 2.5 ml Strep- Tactin Sepharose gravity flow column (IBA GmbH, Göttingen, Germany; at 4°C). The Strep-Tactin Sepharose column was washed, and purified complexes were eluted with wash buffer containing 10 mM desthiobiotin (Sigma-Aldrich, St. Louis, MO). Eluted complexes were purified to homogeneity by injection on Superose 6 16/50 (GE Healthcare) column that was equilibrated in gel filtration buffer (20 mM HEPES, pH 8.0, 150 mM NaCl, and 1 mM TCEP).

3.5.3 HDX-MS

Amide hydrogen exchange mass spectrometry (HDX-MS) was initiated by a 20-fold dilution of stock PI3KC3-C1 (2 μM), PI3KC3-C1 (2 μM) and full-length NRBF2 (5 μM), or MIT-Fusion PI3KC3-C1 into D_2O buffer containing 20 mM HEPES (pD 8.0), 200 mM NaCl and 1 mM TCEP at 30°C. Incubations in deuterated buffer were performed for 10 seconds. Backbone amide exchange was quenched at 0°C by the addition of ice-cold quench buffer (400 mM KH_2PO_4 /H_3PO_4, pH 2.2). Quenched samples were injected onto a chilled HPLC setup with in-line peptic digestion and desalting steps. Desalted peptides were eluted and directly analyzed by an Orbitrap Discovery mass spectrometer (Thermo Scientific, Waltham, MA). The HPLC system was extensively cleaned between samples. Initial peptide identification was performed via tandem MS/MS experiments. A PEAKS Studio 7 (www.bioinfor.com) search was used for peptide identification. Initial mass analysis of the peptide centroids was performed using HDExaminer version 1.3 (Sierra Analytics, Modesto, CA), followed by manual verification of each peptide. The deuteron content of the peptic peptides covering PI3KC3-C1 was determined from the centroid of the molecular ion isotope envelope. The deuteron content was adjusted for deuteron gain/loss during pepsin digestion and HPLC.

3.5.4 Electron microscopy sample preparation

Negatively stained samples of MIT-Fusion complex were prepared on continuous carbon grids that had been plasma cleaned in a 10% O2 atmosphere for 10 s using a Solarus plasma cleaner (Gatan Inc., Pleasanton, CA). 4 μl of MIT-Fusion complex at a concentration of 35 nM in 20 mM HEPES, pH 8.0, 150 mM NaCl, 1 mM TCEP, and 3% trehalose were placed on the grids and incubated for 30 s. The grids were floated on four successive 50 μl drops of 1% uranyl formate solution incubating for 10 s on each drop. The stained grids were blotted to near dryness with a filter paper and air-dried.

3.5.5 EM data collection and image processing

MIT-Fusion complexes were imaged using an FEI Tecnai 12 electron microscope (FEI, Hillsboro, OR) operated at 120 keV at a nominal magnification of 49,000 (2.18 Å calibrated pixel size at the specimen level) using a defocus range of −0.7

to −1.5 µm with an electron dose of 35e^{-}/Å^2. Images were acquired on a TVIPS TemCam F-416 4049 × 4096 pixel CMOS detector (TVIPS GmbH, Gauting, Germany) using the automated Leginon data collection software (Suloway et al. 2005).

3.5.6 CryoEM sample preparation

MIT-Fusion complex datasets

Protochips C-flat 2/1 of 400 mesh grids were coated with a carbon support, and glow-discharged in the presence of amylamine for 55 seconds. A sample of PI3KC3-C2 containing the following subunits: VPS15, VPS34, MIT-12-residue linker-BECN1, ATG14ΔALPS was incubated on a grid for 1 minute at 15˚C, 100% humidity. The sample was protected with 0.02% (v/v) NP40 substitute, 3% (w/v) trehalose and addition of 0.5 mM BS3 crosslinker proceeded for 30 minutes. The sample was blotted for 2 seconds and then plunge frozen within Mark IV Vitrobot into a 50/50 mix of ethane/propane.

3.5.7 CryoEM data collection and image processing

The grid was transferred to a FEI Krios microscope operating at 200 kV and collected with a GIF Quantum energy filter (Gatan), and images acquired with a Gatan K3 Direct Electron Detector with a pixel size of 0.568 Å. Defocus was randomized between -1.5 to -3.5 microns. SerialEM was used to collect an automated dataset of 8,089 micrographs.

3.5.8 Modeling

Homolog models were made using the yeast 4.5 Å crystal structure (PDB: 5DFZ) using Swiss-modeler. Homology models were docked into a 6.5 Å reconstruction using UCSF Chimera using the fit Map in Model tool. The crystal structure from the MIT domain of NRBF2 was docked into the EM envelope (PDB: 4ZEY). The rest of the model was adjusted, manually, in Coot using real-space refinement tools, and placement of helices when appropriate.

3.5.8 Lipid kinase assay

ATP consumption in the presence of lipids was determined using the ADP-Glo Kinase Assay kit (Promega, Madison, WI). The kinase reaction was performed in 96-well NBS white plates (Corning, Corning, NY), in 1.25× kinase reaction buffer (12.5 mM HEPES, pH 7.0, 125 mM NaCl, 2.5 mM $MnCl_2$). Samples were PI3KC3-C1 (20 nM), PI3KC3-C1 (20 nM) and NRBF2 (500 nM), PI3KC3-C1 (20 nM) and NRBF2$^{\Delta CC}$ (500 nM). The reaction was initiated by adding 5 µl of 125 µM ATP to 20 µl of 1.25× kinase reaction buffer. The reaction was carried out for 30 minutes at 23°C, then 25 µl of ADP-Glo reagent containing 10 mM $MgCl_2$ was added to the reaction mixture and incubated at 23°C for 30 min to stop the enzyme reaction and deplete unconsumed ATP. After depletion of ATP, 50 µl of Kinase Detection Reagent was added to convert ADP to ATP and to introduce luciferase and luciferin for ATP detection. The reaction mixture was further incubated 23°C for 30 min and the luminescence was measured with a GloMax-Multi detection system (Promega).

CHAPTER 4:

Bidirectional control of autophagy by BECN1 BARA domain dynamics

The content in this chapter was published by Chunmei Chang†, **Lindsey N. Young**†, Kyle L. Morris, Sören von Bülow, Johannes Schöneberg, Hitomi Yamamoto-Imoto, Yukako Oe, Kentaro Yamamoto, Shuhei Nakamura, Goran Stjepanovic, Gerhard Hummer, Tamotsu Yoshimori and James H. Hurley (2019) 'Domain Dynamics Article Bidirectional Control of Autophagy by BECN1 BARA Domain Dynamics', pp. 339–353. doi: 10.1016/j.molcel.2018.10.035.
†Equal contribution.

Author contributions: the wonderful biochemistry presented here was done by Chunmei Chang, the EM and cryo-EM studies were performed by Lindsey Young, with advice from Kyle Morris, Sören von Bülow performed the Molecular Dynamics Simulations, Johannes Schöneberg wrote a script to quantify fluorescence signals. All model cartoons were made with love by Lindsey Young, with from input from Chunmei and Jim. Chunmei Chang, Lindsey Young, and Jim Hurley wrote the manuscript.

Chapter 4: Bidirectional control of autophagy by BECN1 BARA domain dynamics

4.1 Summary

Membrane targeting of the BECN1-containing class III PI 3-kinase (PI3KC3) complexes is pivotal to the regulation of autophagy. The interaction of PI3KC3 complex II and its ubiquitously expressed inhibitor, Rubicon, was mapped to the first β sheet of the BECN1 BARA domain by hydrogen-deuterium exchange and cryo-EM. The interaction determinants were confirmed in cell-based assays of PI3KC3 activity and autophagy. These data suggested that BARA β sheet-1 unfolds to directly engage the membrane. This mechanism was confirmed using protein engineering, giant unilamellar vesicle assays, and molecular simulations. Using this mechanism, a BECN1 β sheet-1-derived peptide activates both PI3KC3 complexes I and II, while HIV-1 Nef inhibits complex II. These data reveal how BECN1 switches on and off PI3KC3 binding to membranes. The observations explain how PI3KC3 inhibition by Rubicon, activation by autophagy-inducing BECN1 peptides, and inhibition by HIV-1 Nef, are mediated by the switchable ability of the BECN1 BARA domain to partially unfold and insert into membranes.

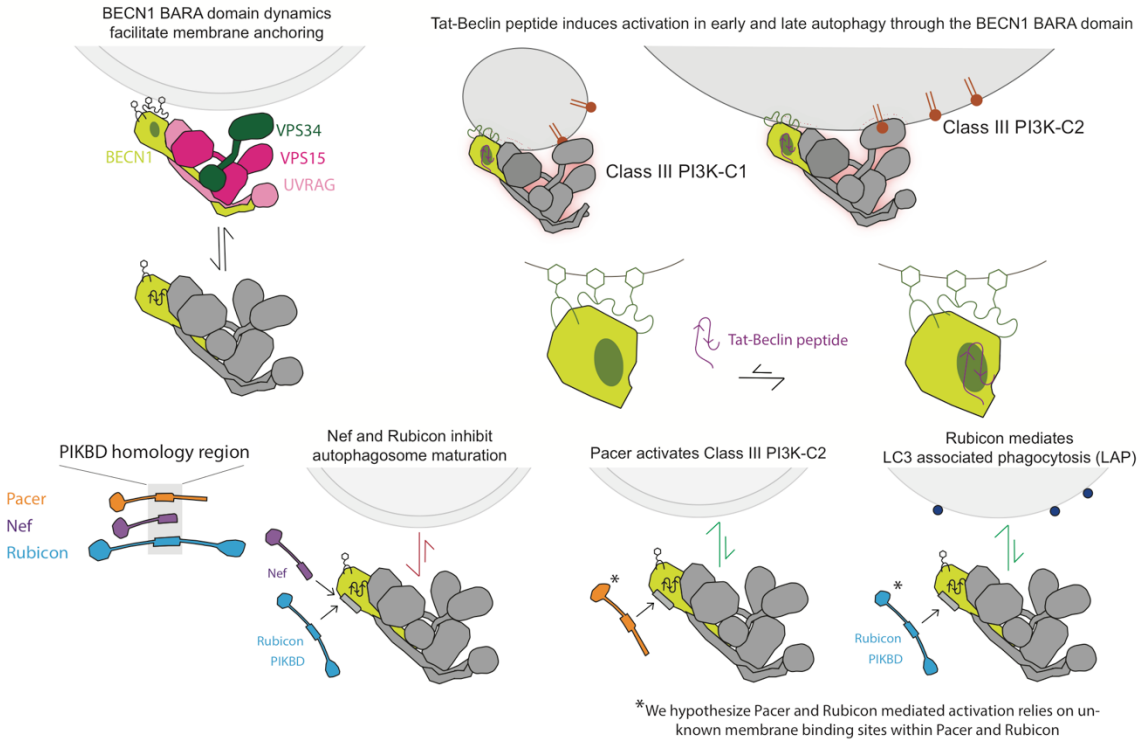

Figure 4.1 Graphical abstract
The BECN1 BARA domain plays a dual role in autophagy regulation. It is a target for the autophagy inducing Tat-Beclin peptide and can be inhibited by anti-autophagy proteins Nef and Rubicon.

4.2 Introduction

Autophagy is the degradative process of cytosolic cargo engulfment by the double membrane phagophore (also known as the isolation membrane) for its transport to the lysosome (Mizushima, Yoshimori, and Ohsumi 2011). Autophagy is essential for cellular homeostasis and survival during starvation. Autophagic dysfunction is thought to contribute to neurodegeneration, cancer, aging, infection, and liver and other diseases (Mizushima et al. 2008), and inducers of autophagy are actively being sought as candidate therapeutic agents (Galluzzi et al. 2017). The generation of phosphatidylinositol 3-phosphate (PI(3)P) by the class III phosphatidylinositol 3-kinase (PI3KC3) complexes I and II (PI3KC3-C1 and –C2) (Itakura et al. 2008; Kihara et al. 2001; Sun et al. 2008) is central to the initiation and expansion of the phagophore (Bento et al. 2016; J.H. Hurley and Young 2017).

All PI3KC3 complexes contain the lipid kinase VPS34, the scaffold and putative protein kinase VPS15, and the regulatory subunit BECN1 (J. M. Backer 2016; J.H. Hurley and Young 2017). PI3KC3-C1 and C2 are distinguished by the mutually exclusive presence of either ATG14 or UVRAG (Itakura et al. 2008; C. Liang et al. 2008; Matsunaga et al. 2009; Sun et al. 2008; Yun Zhong et al. 2009b), respectively, which both engage with the core complex via the central coiled-coil of BECN1 (Li et al. 2012). PI3KC3-C1 functions in autophagy initiation (Itakura et al. 2008; Obara, Sekito, and Ohsumi 2006; Sun et al. 2008), while PI3KC3-C2 functions in both in phagophore expansion (Itakura et al. 2008; C. Liang et al. 2006) and in the non-autophagic process of endosome maturation (J. M. Backer 2016). ATG14 and UVRAG form a heterodimeric regulatory subcomplex with BECN1 through a parallel coiled coil interaction. One copy of such a regulatory complex then assembles with the catalytic VPS34:VPS15 subcomplex to form the complete PI3KC3 complex. Further variants of complexes I and II are formed in cells by the incorporation of additional subunits, including the C1 activating subunit NRBF2 (Cao et al. 2014; Lu et al. 2014; Zhong et al. 2014) and the potent C2 inhibitor Rubicon (Matsunaga et al. 2009; Yun Zhong et al. 2009b).

BECN1 is the smallest subunit in the complex, yet it has a vital and central role as a hub coordinating autophagy with other cell processes, including apoptosis (Hurley & Young 2017; Levine et al. 2016). BECN1 was the first mammalian autophagy protein to be characterized (X. H. Liang et al. 1999), and its discovery as a tumor suppressor connected autophagy to cancer (X. H. Liang et al. 1999). BECN1 connects PI3KC3 to the membrane via its C-terminal BARA (beta-alpha repeated, autophagy; the BARA overlaps with a region formerly known as ECD) domain (Huang et al. 2012). BECN1 is the target for autophagy regulation by the anti-apoptotic protein Bcl-2 (Pattingre et al. 2005), the C1 complex activating subunit NRBF2 (L. N. Young et al. 2016), and phosphoreglation by ULK1 (Egan et al. 2015; Russell et al. 2013), EGFR (Wei et al. 2013), MAPKAPK2/3 (Wei et al. 2015)(Wei et al., 2015), AMPK (J. Kim et al. 2013), DAPK (Zalckvar et al. 2009), and Akt (R. C. Wang et al. 2012). The Nef protein of HIV-1 has been reported to inhibit autophagy by targeting BECN1 (Kyei et al., 2009). A peptide fragment of BECN1 corresponding to its putative

Nef binding site is a remarkably potent inducer of autophagy in cells when cell penetrability is conferred by fusion to the polybasic domain of HIV-1 Tat (Shoji-Kawata et al. 2013). This Tat-BECN1 peptide (T-BP) promotes clearance of toxic protein aggregates and intracellular pathogens from cells (Shoji-Kawata et al. 2013). A major goal of structural studies of autophagic complexes (James H. Hurley and Schulman 2014) has been to understand how these many regulatory influences on BECN1 are communicated to the VPS34 catalytic domain and converted into changes in PI(3)P levels, thereby regulating autophagy.

PI3KC3-C1 and C2 have essentially the same V-shaped three-dimensional architecture (Baskaran et al. 2014; Rostislavleva et al. 2015). The right arm of the V contains the catalytic domains of VPS15 and VPS34. The V-shaped structure is probably an inactive conformation, as the VPS34 catalytic domain needs to dislodge from its position in this structure to phosphorylate its lipid substrate (Stjepanovic et al. 2017). On its own, the VPS34 catalytic domain has relatively low activity compared to that of the assembled complex (Stjepanovic et al. 2017). A major role of the rest of the PI3KC3 complex is to deliver VPS34 to membranes. BECN1 seems to play an important role in membrane targeting of the complex. The BECN1-containing subcomplex resides in the left arm of the V, where its parallel coiled-coil binds to the non-catalytic C-terminal helical and WD40 domains of VPS15 and the N-terminal C2 domain of VPS34 (Baskaran et al. 2014; Rostislavleva et al. 2015). BECN1 binds to membrane through its C-terminal BARA domain (Huang et al. 2012), which is located at the end of the left arm together with the BARA-like BARA2 domain of UVRAG. The BECN1 BARA binds to membranes, at least in part, through three hyper-exposed aromatic “finger” residues (Huang et al. 2012) which are located at the outermost tip of the left arm and ideally situated to insert into target membranes.

One of the major endogenous regulatory proteins is Rubicon, which is a widely expressed and potent negative regulator of autophagy. Rubicon tightly associates with PI3KC3-C2 (Matsunaga et al. 2009; Yun Zhong et al. 2009b). Rubicon contains an N-terminal RUN domain (RPIP8, UNC-14, NESCA motif), a middle region (MR) that includes predicted disordered, helical, and coiled-coil domains, and C-terminal cysteine-rich (CRD) and Rubicon Homology (RH) domains (Figure 4.2). Rubicon is the founding member of a group of RH-domain containing autophagy and PI3KC3-C2 regulatory proteins, which also includes PLEKHM1 (McEwan et al. 2015; Tabata et al. 2010) and Pacer (Cheng et al. 2017). In this study, we began by seeking to understand how Rubicon inhibits PI3KC3-C2 because of its broad importance in autophagic regulation and for potential insights into the development of autophagy inducers. We discovered that despite Rubicon's C2-directed specificity, it inhibits autophagy by targeting the ability of the BECN1 BARA domain to target membranes. This led us to uncover a mechanism whereby the dynamics of the first β-sheet of BECN1 allow it to unfold and "flip out" of its ground state crystallized conformation and insert into target membranes, promoting VPS34 activity. This mechanism is general to both complexes I and II. It offers an explanation for the potency of the BECN1-derived TBP peptide as an autophagy inducer, and suggests a path forward for

the design of small molecule autophagy inducers acting by the same mechanism. Finally, we show that HIV-1 Nef inhibits PI3KC3 by the same mechanism, highlighting the importance of this mode of membrane docking and the wide use of this mechanism to regulate autophagy in normal physiology and infection.

4.3 Results

4.3.1 Mapping the Rubicon PIKBD

We began by mapping the PI3KC3-C2 binding and inhibitory region of Rubicon. We found that the RUN and CRD-RH domains did not interact with the intact PI3KC3-C2, despite reported binding of the RUN domain to isolated VPS34 (Sun et al. 2011). The MR bound as well as full length Rubicon, and full binding was retained in a smaller C-terminal fragment of the middle domain (MRC; Fig. Figure 4.2). We therefore judged that the MRC encompassed the PI3KC3-C2 binding and inhibitory properties of the full Rubicon protein, and refer to it henceforward as the PIKBD (PI3KC3-C2 binding domain). Both MR and PIKBD formed stable and monodisperse complexes with PI3KC3-C2 on size exclusion chromatography (Figure 4.2). Full-length Rubicon, MR, and PIKBD all inhibited PI3KC3-C2 lipid kinase activity in small unilamellar vesicles (SUVs) by a factor of 2 at 12.5 nM concentration (Figure 4.2).

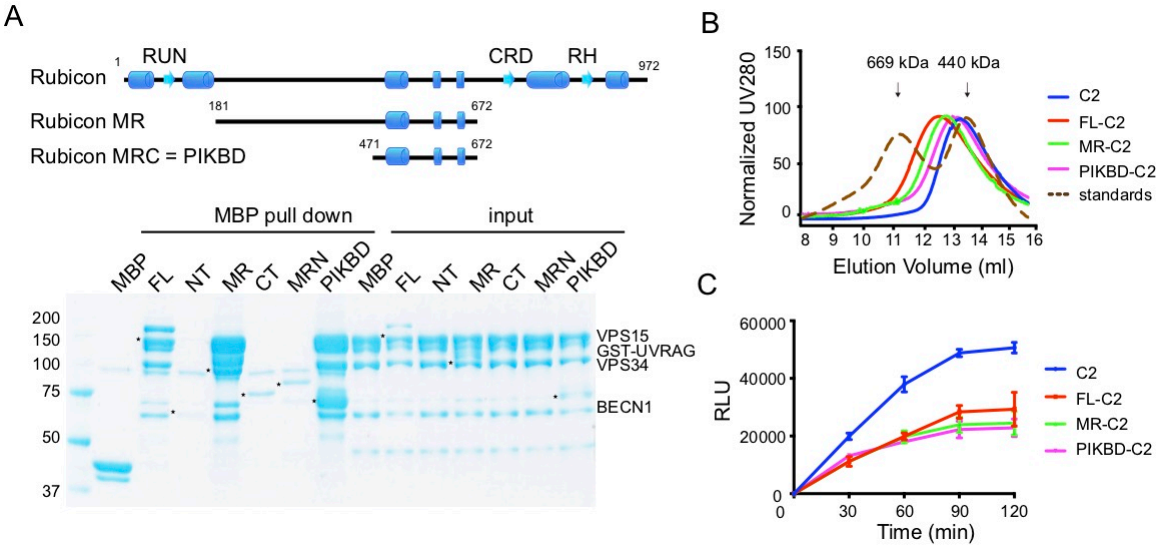

Figure 4.2 Mapping the Rubicon PIKBD.
(A) Schematic diagram of the predicted secondary structure of Rubicon (upper). MBP tagged full length Rubicon or deletion mutants were co-expressed with the subunits of PI3KC3-C2 (GST tagged UVRAG; Strep tagged VPS34, VPS15 and BECN1) in HEK293 cells. Both MBP and GST pull down were performed. The resulting precipitates were visualized by SDS-PAGE (lower). GST pull-down precipitates were represented as input. FL, full length; MR, middle region; NT, N terminus; CT, C terminus; MRN, middle region N terminus; MRC, middle region C terminus; PIKBD, PI3KC3-binding domain. (B) Size exclusion chromatography of PI3KC3-C2 complexes. Different complexes are indicated with color codes at right. The peak fraction of each complex was used for subsequent activity assays. UV, ultraviolet. (C) Activities of PI3KC3-C2 complexes (12.5 nM) on SUVs containing PI. Different complexes are indicated with color codes. RLU, relative light units.

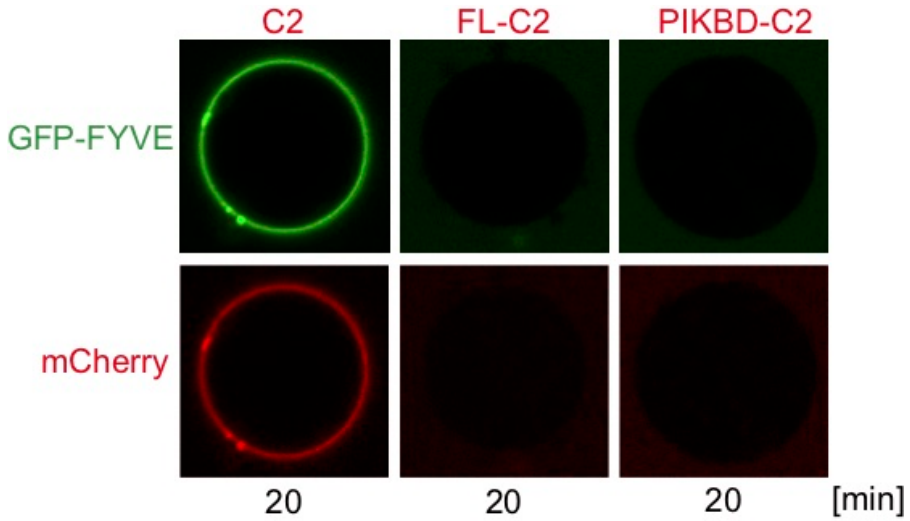

Figure 4.3: Rubicon and Rubicon PIKBD inhibit PI3KC3-C2 on GUVs
Confocal images of GUVs showing the binding of FYVE domain (green) and different PI3KC3 complexes (red). GUVs were incubated with wild type C2, Rubicon FL-C2, or Rubicon PIKBD-C2 complex respectively.

We also probed PI3KC3-C2 activity using a giant unilamellar vesicle (GUV) assay in which PI(3)P production is monitored using a GFP-FYVE domain probe and PI3KC3-C2 binding to the membrane is monitored with an mCherry-PI3KC3-C2 fusion (Figure 4.3). Wild-type PI3KC3-C2 robustly generates PI(3)P and binds strongly to the GUV membrane (Figure 4.3). Both full-length Rubicon and the PIKBD essentially completely inhibit both membrane binding and PI(3)P production (Figure 4.3). These data also lead to a second important conclusion, that Rubicon inhibits PI3KC3 by blocking membrane binding.

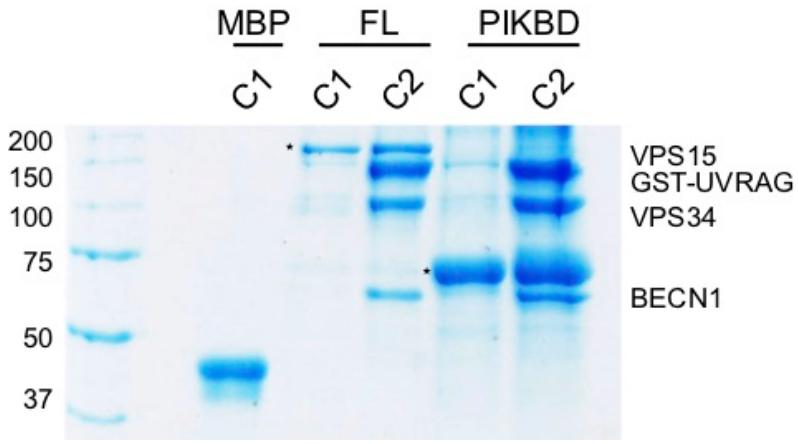

Figure 4.4: Rubicon binds specifically PI3KC3-C2 over PI3KC3-C1
MBP tagged full length Rubicon or PIKBD were co-expressed with the subunits of PI3KC3-C1 or C2 in HEK293 cells. The MBP pull-down precipitates were visualized by SDS-PAGE.

Rubicon is generally considered to be a specific modulator of PI3KC3-C2 activity. We investigated whether purified full-length Rubicon could bind to recombinant PI3KC3-C1 (Figure 4.4). Only trace binding to PI3KC3-C1 (ATG14)

was observed (Figure 4.4). This was in accord with the expectation that binding to complex II would be strongly preferred. The PIKBD mirrored the very weak binding of full-length Rubicon to PI3KC3-C1, indicating that the fragment is, like full-length Rubicon, specific for C2 over C1.

4.3.2 Rubicon PIKBD targets BECN1 BARA β-sheet 1

We used hydrogen-deuterium exchange coupled to mass spectrometry (HDX-MS) to probe Rubicon-PI3KC3-C2 interactions in more detail. HDX of Rubicon-PI3KC3-C2 samples was compared to Rubicon PIKBD and PI3KC3-C2 samples alone at 10, 30, 60, and 90 s (Figure 4.5). No significant (> 5%) changes in protection were seen for VPS34 or VPS15 (data not shown). Two peptides from BECN1 were protected by more than 10 % in the presence of PIKBD, spanning residues 261-287 (Figure 4.5). These two peptides correspond to the first β sheet of the BECN1 BARA domain (Figure 4.5). Remarkably, the residues spanned by this region (265-287) are nearly identical to those contained in the TBP (residues 267-284) (Shoji-Kawata et al. 2013). Protection of > 5 % was observed in a part of the UVRAG BARA2 (Figure 4.5) that is adjacent in the three-dimensional structure as inferred from the yeast C2 structure (Figure 4.5**)** (Rostislavleva et al. 2015).

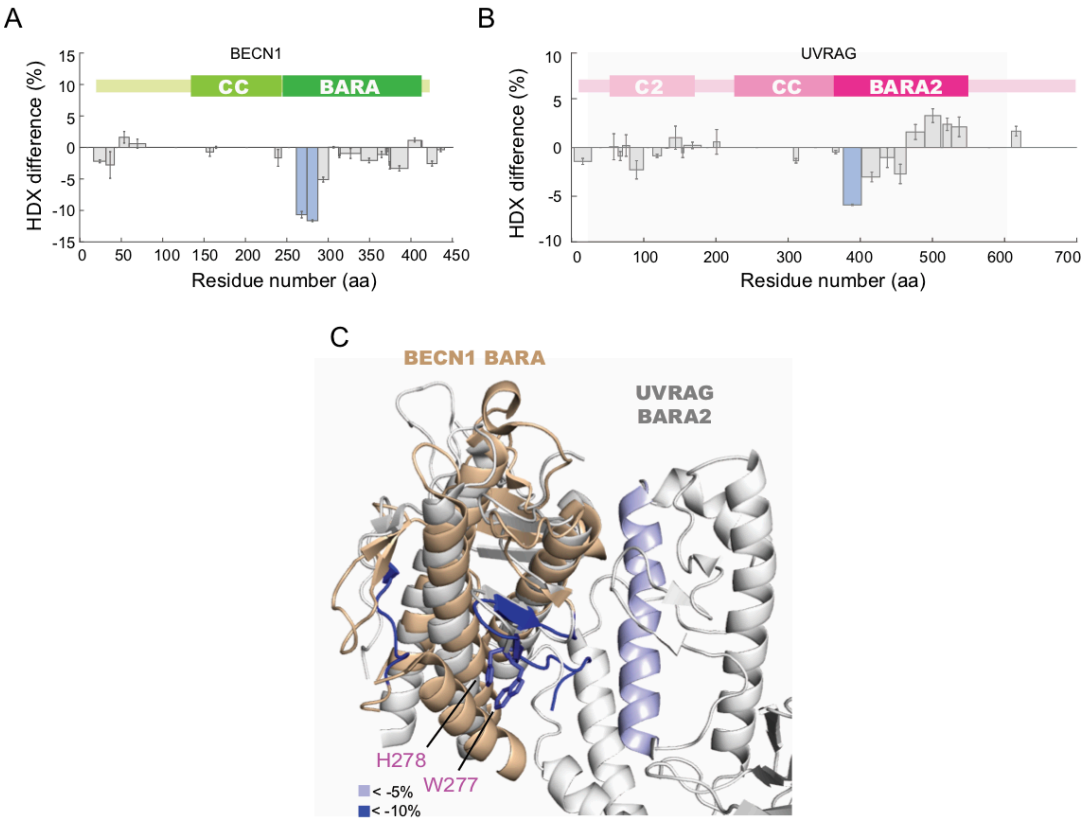

Figure 4.5 Mapping binding sites of Rubicon and PI3KC3-C2 by HDX-MS.
(A) Difference plot of percent deuteron incorporation in BECN1 of PI3KC3-C2 versus deuterons incorporated in the presence of Rubicon, 30s in D2O. (B) Difference plot of percent deuteron incorporation of UVRAG of PI3KC3-C2 versus deuterons incorporated in the presence of Rubicon, 30s in D2O. (C) HDX-MS difference map onto the crystal structure of human BECN 1

BARA domain (wheat) and crystal structure of yeast PI3KC3-C2 (grey), BECN1 BARA domain was aligned to the yeast crystal structure. Regions showing a decrease in HDX are depicted in blue (10% decrease) and lavender (5% decrease) in the presence of Rubicon.

4.3.3 Probing the BECN1 BARA domain

In order to confirm that β-sheet 1 was the major Rubicon binding site, we first replaced the entire β-sheet 1 with a polar loop (BECN1^{BS1PL}), and second, mutated the two most prominent exposed side chains of β-sheet 1, Trp277 and His278 (Figure 4.6, to Asp (BECN1 $^{WW-DD}$). BECN1 BS1PL and BECN1 WW-DD were expressed as part of reconstituted PI3KC3-C2, and neither was capable of pulling down Rubicon PIKBD (Figure 4.6). In contrast, the BECN1 BARA aromatic finger triple mutation BECN1^{DDD}, previously shown to block membrane binding (Huang et al., 2012), had no effect on Rubicon binding (Figure 4.6), indicating that the Rubicon binding site does not overlap with the previously established membrane binding site on BECN1. We went on to determine more precisely which portion of PIKBD bound directly to PI3KC3-C2. HDX-MS protection of >10 % was seen in the first and third of the three predicted helical regions of PIKBD (Figure 4.6). We determined by pull-down assay that the first helix, which is conserved in the PI3KC3-C2 binding region of Pacer (Cheng et al., 2017), was essential for PI3KC3-C2 binding, while the third region was dispensable (Figure 4.6).

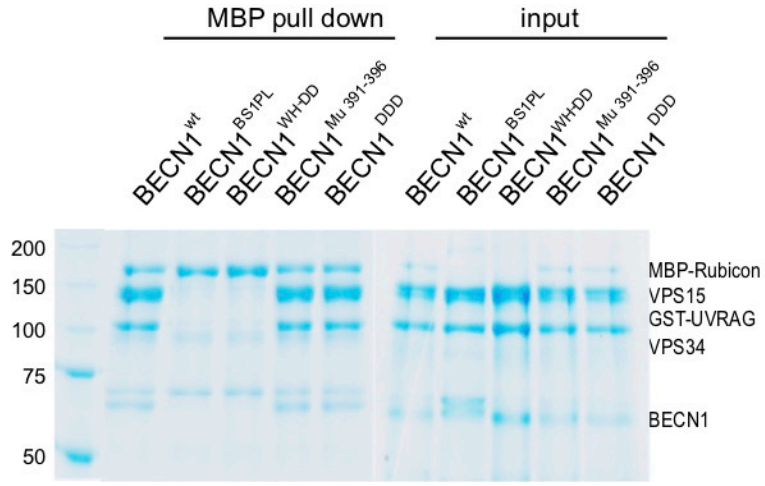

Figure 4.6 BECN1 mutants

BECN1 or mutants were co-expressed with full length MBP-tagged Rubicon and the other subunits of PI3KC3-C2. Both MBP and GST pull-down precipitates were visualized by SDS-PAGE.

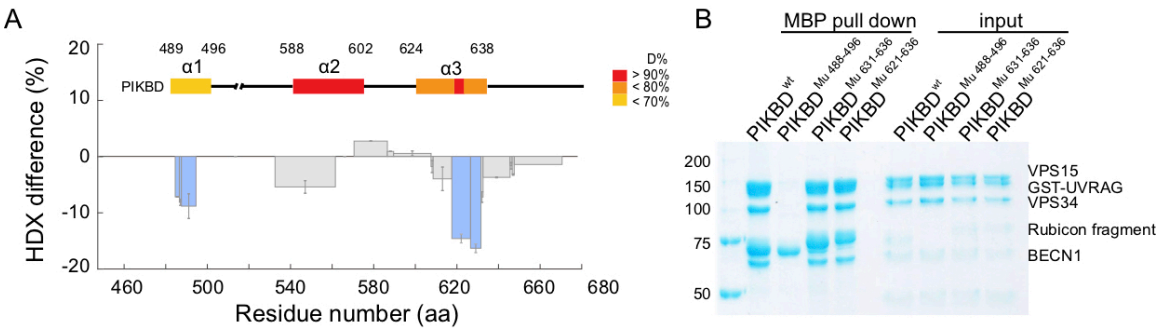

Figure 4.7: Rubicon PIKBD mutants
(A) Difference plot of %D incorporated into Rubicon PIKBD within the PI3KC3-C2 complex versus deuterons incorporated into Rubicon PIKBD alone after 10 s in D2O. The Rubicon PIKBD secondary structure drawing (upper) illustrates the heat map of apo state. Three predicted α-helices (α1-α3) are colored according to %D exchange. Data are presented as Mean ± Stddev, n=3. (B) MBP tagged Rubicon PIKBD or PIKBD mutants were co-expressed with the subunits of PI3KC3-C2 in HEK293 cells. Both MBP and GST pull-down precipitates were visualized by SDS-PAGE.

4.3.4 PIKBD inhibits PI(3)P production and autophagy in vivo

To further elucidate the function of PIKBD region of Rubicon, we replaced the central PIKBD residues 488-496 with Ala. We carried out HDX-MS on the mutant construct at three time points and found there was no change to its conformational stability relative to wild-type. We evaluated the impact of overexpressing the wild-type and mutant fragments on PI(3)P generation in cells as detected with a GFP-FYVE probe (Gillooly et al. 2000). Overexpression of Rubicon PIKBD inhibited PI(3)P production as strongly as full length Rubicon, while the PIKBD mutant had minimal effect (Figure 4.8). We also examined its effect on autophagic flux in HeLa cells from which Rubicon was genetically deleted. While wild-type Rubicon significantly reversed the autophagic flux in knock out cells, Rubicon PIKBD mutant does not, further highlighting the importance of this region in vivo (Figure 4.8). These data show that the inhibitory mechanism observed in vitro and described above is also the mechanism operative in cells.

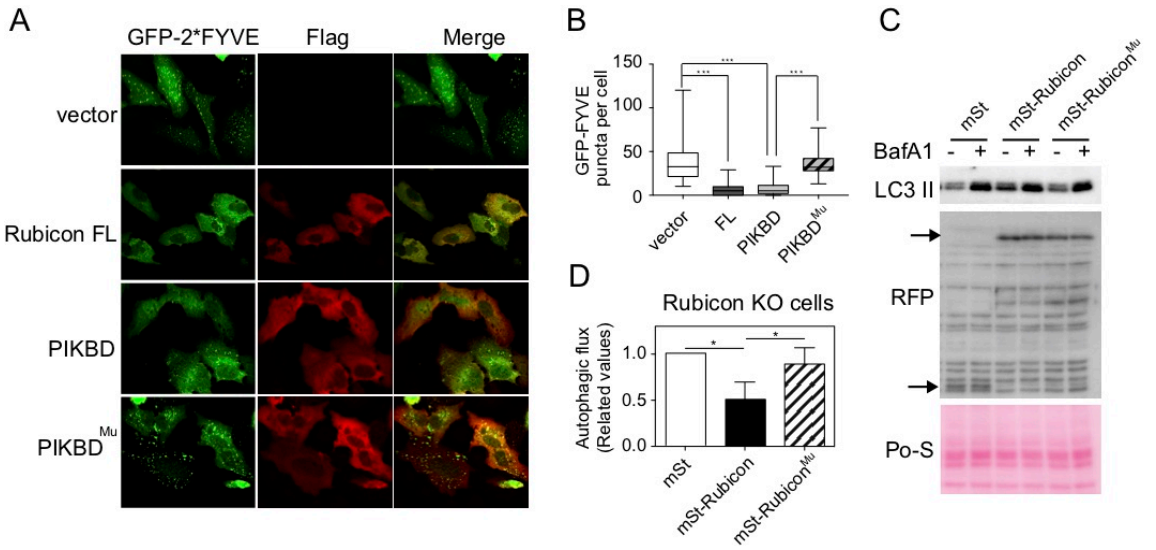

Figure 4.8: Rubicon PIKBD inhibits PI(3)P production and autophagic flux in vivo

(A) Distribution of GFP-FYVE (green) and Rubicon fragment (red) in U2OS cells. Cells transfected with Flag vector, Flag-Rubicon, Flag-Rubicon-PIKBD, or Flag-Rubicon-PIKBD mutant were starved with EBSS for 2 h. (B) Quantification of the number of GFP-FYVE puncta per cell in cells treated as in D. The data are quantified with Image J, and analyses were performed using GraphPad Prism 5 software. Data are presented as Mean ± Stddev, n = 50. ***p < 0.001. (C) The representative Western Blot for autophagic flux assay in Rubicon-KO cells with anti-LC3 antibody. After the transfection of mStrawberry (mSt), mSt-Rubicon, or mSt-Rubicon mutant, cells were starved with EBSS in the presence or absence of Bafilomycin A1(Baf A1). (D) Quantification of autophagic flux in (C). The data are quantified using Image J, and analyses were performed using GraphPad Prism 5 software. Comparisons between groups were performed using the one-way analysis of variance. Data are denoted as Mean ± Stddev, n=3. p values ≤ 0.05 were considered significant (*). Anti-RFP antibody and ponceau S (Po-S) were used to confirm the transfection efficacies of each plasmid and the loading protein amounts, respectively.

4.3.5 Cryo-EM structure of PI3KC3-C2 bound to Rubicon PIKBD

An initial negative stain EM characterization of MBP-PIKBD binding to PI3KC3-C2, using the MBP tag as a localization aid, confirmed that PIKBD was situated at the tip of the BECN1-UVRAG portion of the complex. This is at the end of the left arm in the standard view (Figure 4.9).

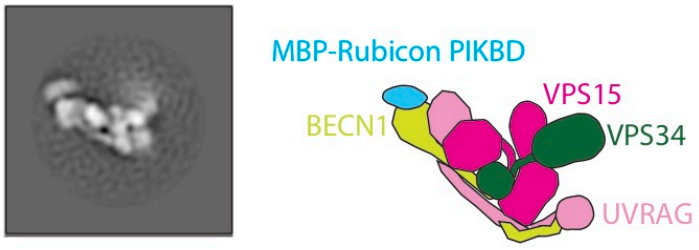

Figure 4.9: MBP-PIKBD localizes to the left arm of PI3KC3-C2

Negative stain EM on PI3KC3-C2 MBP-Rubicon PIKBD and model for domain placement.

PI3KC3 complexes are conformationally dynamic (Stjepanovic et al. 2017), which has made cryo-EM studies challenging. We generated a fusion between the C-terminus of BECN1 and the PIKBD on the basis of the HDX-MS and negative stain EM studies. The lipid kinase activity of the fusion was identical to that of PIKBD-inhibited PI3KC3-C2 (Figure 4.10. Moreover, this construct manifested the same pattern of HDX protection localized to BECN1 BARA residues 265-287 (Figure 4.10). This fusion was combined with a VPS34-VPS15 fusion (Stjepanovic et al. 2017), previously shown to stabilize the V-shaped "classic" conformation without otherwise perturbing the structure of the subunits. This material led to a sample with improved stability and decreased conformational heterogeneity, which was promising as judged by 2D class averages (Figure 4.11)

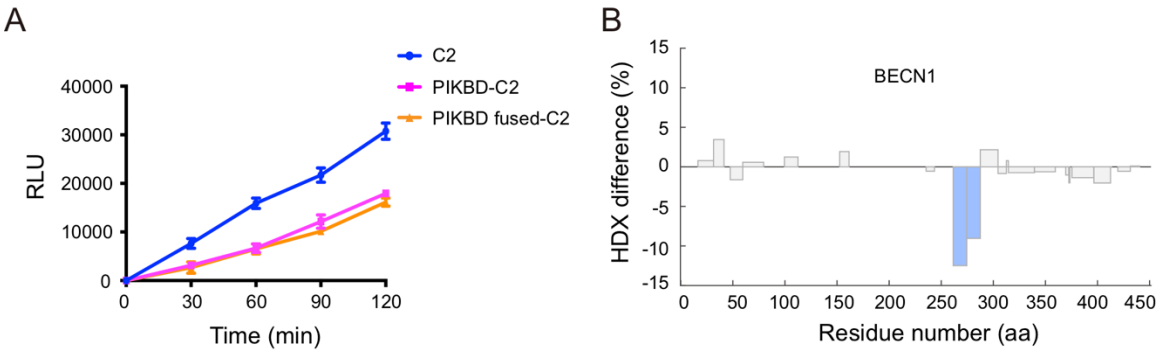

Figure 4.10 PIKBD-C2 Fusion complex

(A) PIKBD inhibits C2 whether as a fusion BECN1 (orange) or in the unfused state (pink). (B) BECN1 residues 265-287 were protected in the PIKBD-fusion-C2 complex.

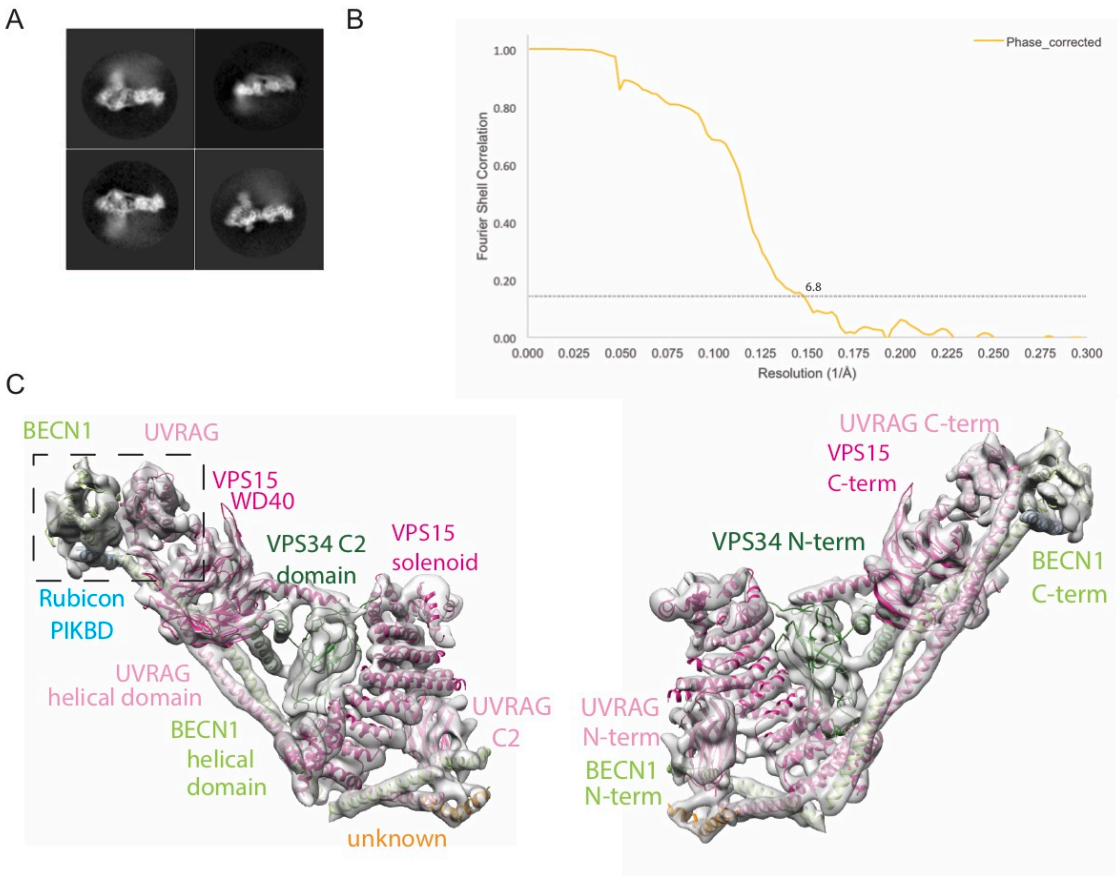

Figure 4.11: Cryo-electron microscopy on PI3KC3-C2:Rubicon PIKBD.
(A) 2D-class averages of PI3KC3-C2:MBP-Rubicon PIKBD by cryo-EM. (B) Whole reconstruction gold-standard FSC resolution estimation of PI3KC3-C2:Rubicon-PIKBD. (C) Model fit of 6.8 Å map, BECN1 in lime green, helix corresponding to Rubicon PIKBD, UVRAG in pink, VPS15 in magenta, and VPS34 in forest green.

A data set was obtained from a VPS34-VPS15:BECN1-PIKBD:UVRAG complex sample on a Titan Krios, leading to a 6.8 Å reconstruction (Figure 4.11, 4.13). The most heterogeneous part of the complex is the VPS34 catalytic domain, whose conformational dynamics is reduced, but not eliminated, in the VPS34-VPS15 fusion. This region was therefore removed from averaging by masking (Figure 4.12).

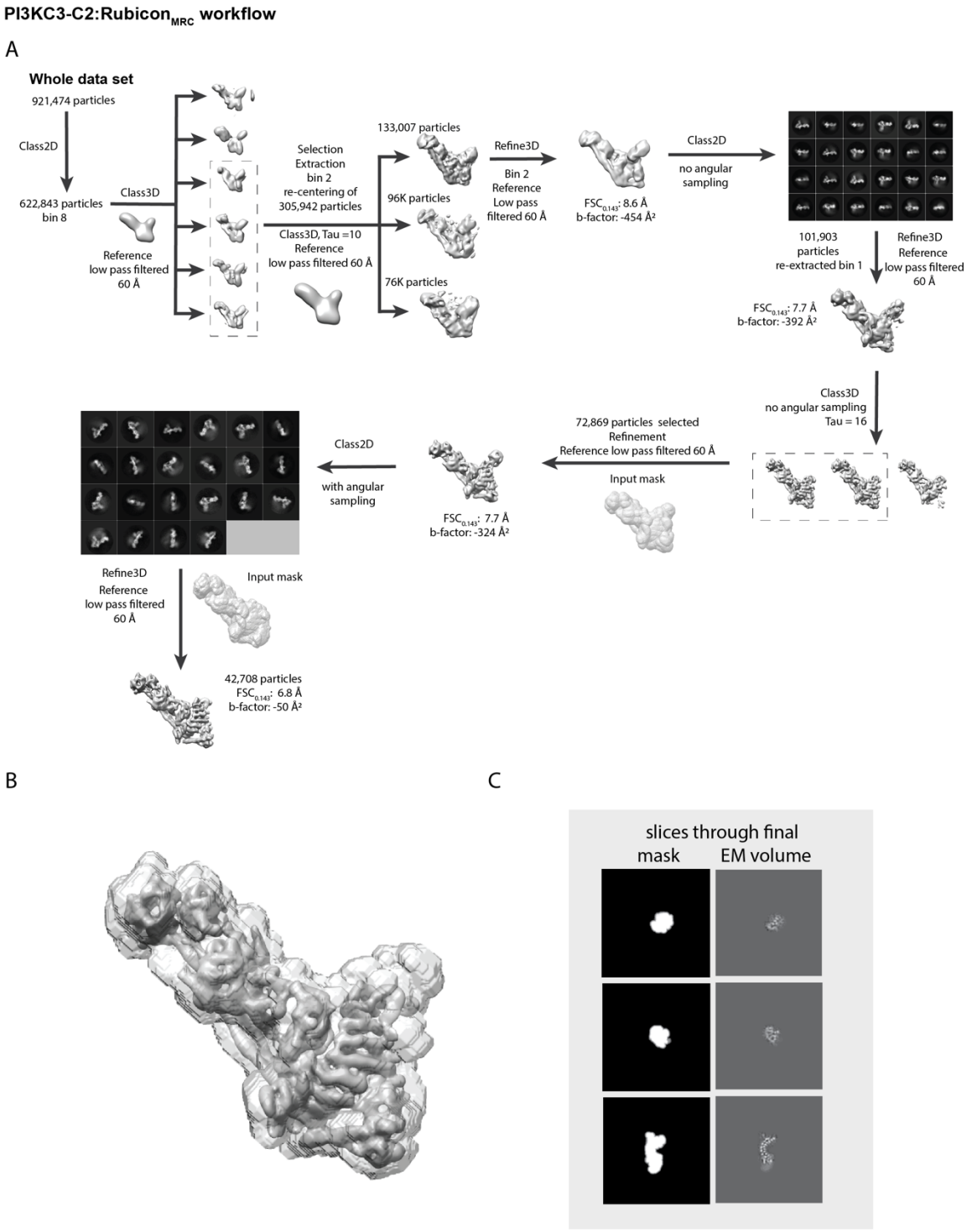

Figure 4.12 CryoEM workflow

(A) CryoEM data on PI3KC3-C2: Rubicon PIKBD was processed starting with 921,474 particles, subjected to 2D yielding 622,843 particles that went through 3D classification resulting in 305,942 particles. Re-grouping of 305,942 particles and another round of 3D classification yielded a class of 133,007 particles, which were refined. Another round of 2D classification removed more junk classes, leaving 101,903 particles, which were further refined. Another round of 3D classification removed broken particles, leaving 72,869 particles. These particles were refined, and then subjected to 2D classification with angular sampling, leaving a set of 42,708 very clean particles

that refined to 6.8 Å and a b-factor of -50 Å^2. (B) Sample masking procedure for refining PI3KC3-C2:Rubicon-PIKBD. This mask was generated using the map from the refinement, set at sigma level 6 (initial binarisation threshold 0.0073), the map was then extended 5 pixels (5.75 Å) and a soft-edge was added of 8 pixels (9.2 Å). (C) Slices through the mask and the final post-processed map confirm that the mask is soft, and that the features of the map can be visualized.

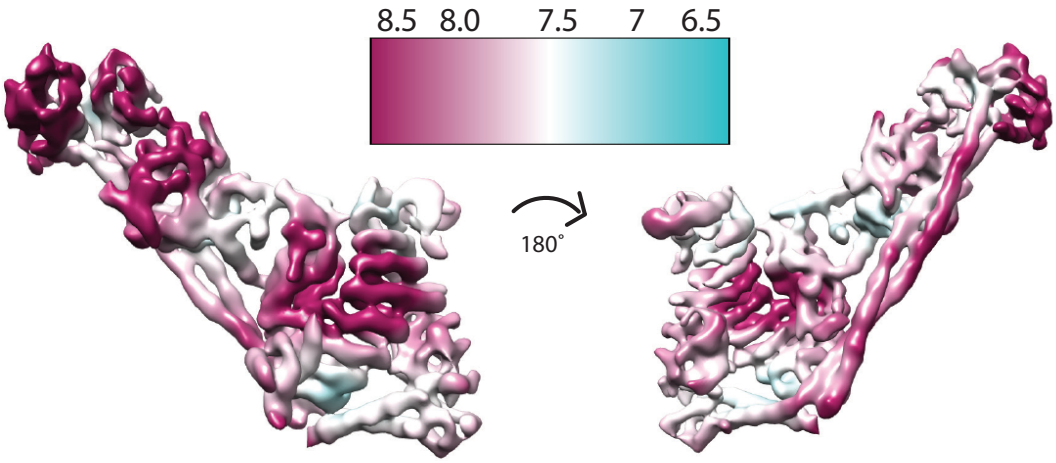

Figure 4.13 Local resolution estimation of the final cryoEM map

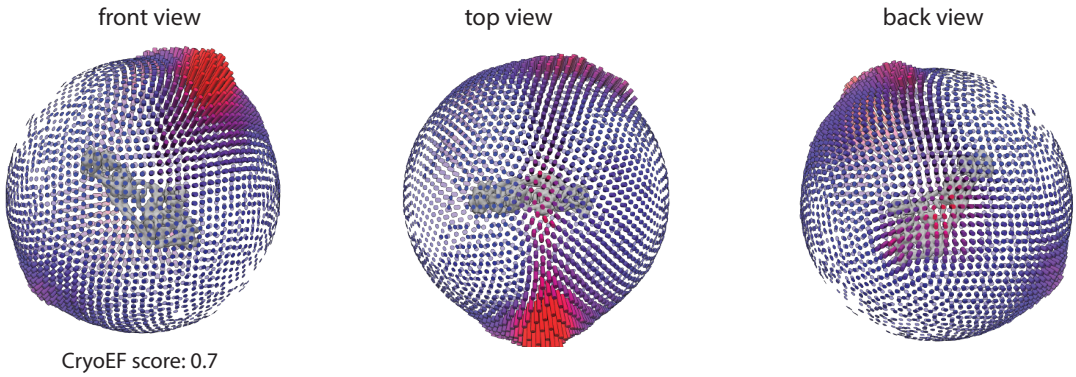

Figure 4.14: Particle distribution
Angular distribution of the final refinement, and a cryoEF score of 0.7.

The remainder of the density is generally consistent with the crystal structure of yeast PI3KC3-C2 (Rostislavleva et al. 2015) (Figure 4.15). The tip of the N-terminus of the UVRAG coiled coil moves by up to 16 Å, with similar large movements by the associated portion of the BECN1 coiled coil. Further along the coiled coils at their C-terminal ends, UVRAG and BECN1 move by 5 Å and 6 Å, respectively. The UVRAG C2 domain moves by 10 Å. The VPS34 C2 β-sheet core does not move, however, the VPS34 C2 helical insert region moves by up to 10 Å (Figure 4.15). These movements likely reflect either the absence of lattice contacts, inherent differences between the human and yeast complexes, or both. These regions are distal to the Rubicon binding site, and these changes are likely unrelated to Rubicon binding and do not affect the interpretation of the Rubicon complex.

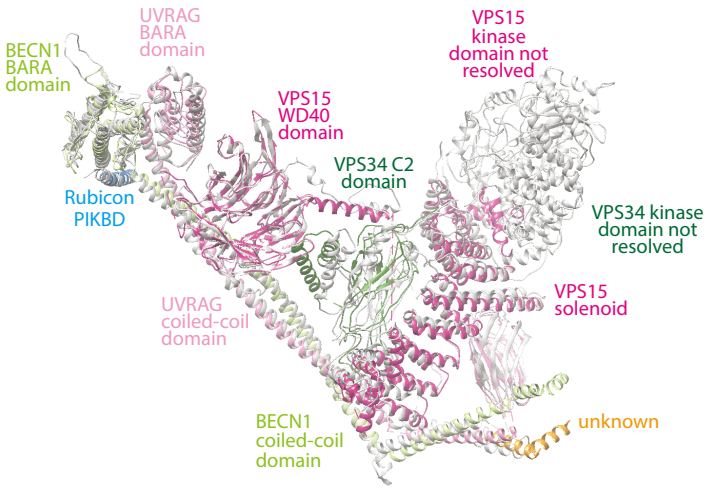

Figure 4.15 Model comparison to yeast PI3KC3-C2
Comparison of human cryo-EM and yeast crystal structures of PI3KC3-C2. An overlay of the yeast model 5DFZ (white) and the model generated in this study. The models were aligned to the C2 domain of VPS34.

4.3.5 PIKBD alpha-1 binds to the BECN1 BARA domain

The only major additional density feature not accounted for by the four subunits of PI3KC3-C2 was located adjacent to the BECN1 BARA domain (Figure 4.11). The local resolution of this part of the structure is estimated at ~8 Å (Figure 4.13). The main density feature corresponds to a 40 Å long α-helix, which is bound to surfaces formed by the first βαβ repeat of the BARA domain (Figure 4.16).

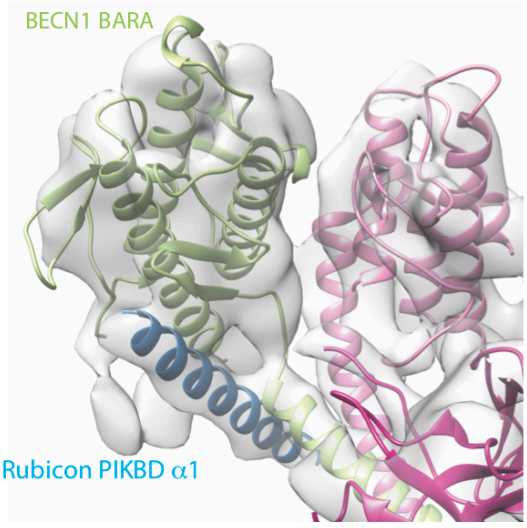

Figure 4.16: Inset of the BECN1 BARA domain where Rubicon PIKBD binds

We provisionally assigned this density to the Rubicon PIKBD. Additional density emanating from the C-terminus of BECN1 was assigned to the BECN1-PIKBD linker. The PIKBD directly contacts Trp277 and His278 (Figure 4.16), consistent with the HDX-MS data.

Based on the orientation of the linker density and the interactions described above, the additional helical density appeared most likely to belong to the first helix α1 of PIKBD. However, at the resolution attained, side chains are not visualized and it is not possible to assign the observed Rubicon density to a unique portion of the PIKBD sequence. Since the PIKBD sequence contains three predicted helical regions (Figure 4.17), we made constructs corresponding to α1 alone and α2-α3 combined. PIKBD-α1 pulled down PI3KC3-C2 effectively, while the α2-α3 did not (Figure 4.17), supporting this assignment. PIKBD-α1 was also inhibited PI3KC3-C2 at 15 nM concentration as judged by the GUV assay (Figure 4.17). However, PIKBD-α1 was somewhat less effective in inhibition than the full PIKBD, suggesting that α2-α3 do contribute to affinity to some degree, even though they are insufficient to pull down PI3KC3-C2 on their own. From these data, we infer that the well-defined helical density modeled as shown in Figure 4.16 corresponds to Rubicon α1 and is responsible for inhibiting BECN1.

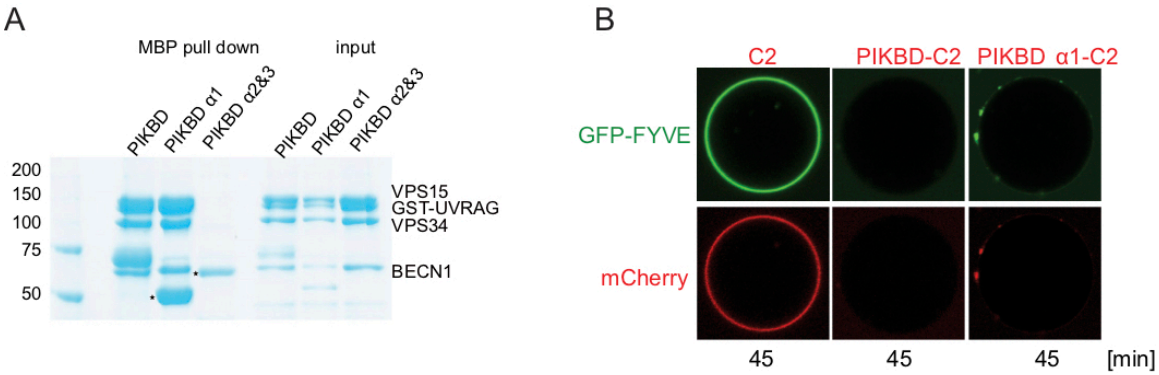

Figure 4.17 PIKBD-α1 pull down experiment
(A) MBP tagged Rubicon PIKBD α1 or α2&3 were co-expressed with the subunits of PI3KC3-C2 in HEK293 cells. Both MBP and GST pull-down precipitates were visualized by SDS-PAGE. (B) Confocal images of GUVs showing the binding of FYVE domain (green) and different PI3KC3 complexes (red). GUVs were incubated with C2, PIKBD-C2, or PIKBD α1-C2 complex respectively.

4.3.6 Membrane docking by BECN1 BARA β-sheet 1

In the crystal structure of BECN1 BARA, 16 residues (248-264) of the BECN1 coiled-coil were included in the construct. In the context of this isolated fragment, this region (referred to as “OH” for overlap helix) is folded back on the rest of the BARA domain (Huang et al. 2012). In structures of full-length BECN1 in the context of the assembled PI3KC3 (Baskaran et al. 2014; Rostislavleva et al. 2015), however, this region is part of the coiled coil that binds to ATG14 or UVRAG. The position and N-to-C direction of the Rubicon PIKBD allow it to be nearly superimposable with the OH helix (Figure 4.18).

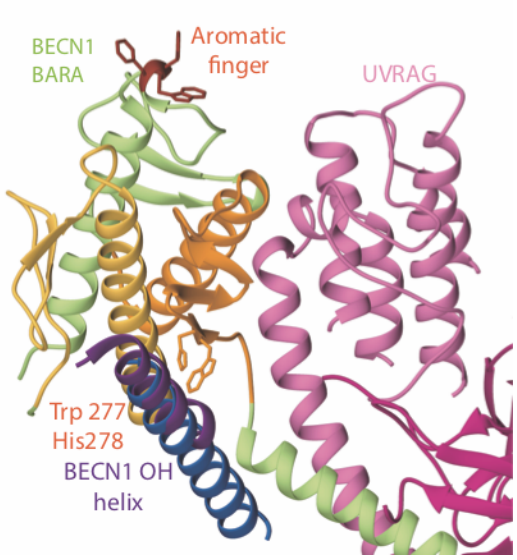

Figure 4.18 Model for PIKBD binding
The OH overlap helix (purple) of BECN1, which is incompatible with the full-length BECN1 subunit, is occupied by a longer helix corresponding to the Rubicon PIKBD (blue). BECN1 BARA domain has three β-α repeats (orange, lime green, and yellow), in the second β-α repeat (lime green) there are three aromatic residues (red) that constitute the aromatic finger necessary for membrane binding. Rubicon-PIKBD (blue) binds to amino acids Trp277 and His278 (orange) located on the first β-α repeat in the BARA domain. Residue register comes from a 1.4 Å crystal structure of the BECN1 BARA domain (4DDP).

This suggests that the face of β-sheet 1 of the BARA domain has a strong propensity to bind to helical structures. The binding of the BECN1 OH to the rest of the BARA domain probably accounts for the conformational stability and crystallizability of the OH-BARA construct (Huang et al. 2012). The HDX-MS data show that the BECN1 BARA β-sheet 1 is relatively dynamic in the full complex in the absence of Rubicon, but are strongly stabilized in its presence. The crystallographic and HDX-MS data taken together strongly suggest that binding of a helix across the face of the β-sheet 1, in particular, strongly stabilizes it in its β-conformation.

The known function of the BECN1 BARA domain is membrane docking (Huang et al. 2012), therefore we hypothesized that PIKBD binding to BECN1 might act by inhibiting the PI3KC3-C2:membrane interaction (Figure 4.19). We tested this idea by carrying out all-atom MD simulations of the BECN1 BARA domain bound to a phospholipid membrane. When β-sheet-1 is locked in its crystallized conformation, the BARA domain binds to the membrane in an upright geometry, the aromatic finger is stably anchored in the membrane, and the finger comprises the primary attachment site (Figure 4.19). When the β-sheet-1 region is unlocked and allowed to interact with the membrane, Phe270 and 274 form additional stable anchors with the membrane (Figure 4.19), while the positions of surrounding polar residues in the 265-287 region fluctuate. In the unlocked simulation, the geometry remains upright, the aromatic finger remains docked in the membrane, and the fold of the rest of the BARA domain is stable. The main consequence of β-sheet 1 unlocking is to dramatically increase the overall

strength of the hydrophobic interactions between the BARA domain and the membrane.

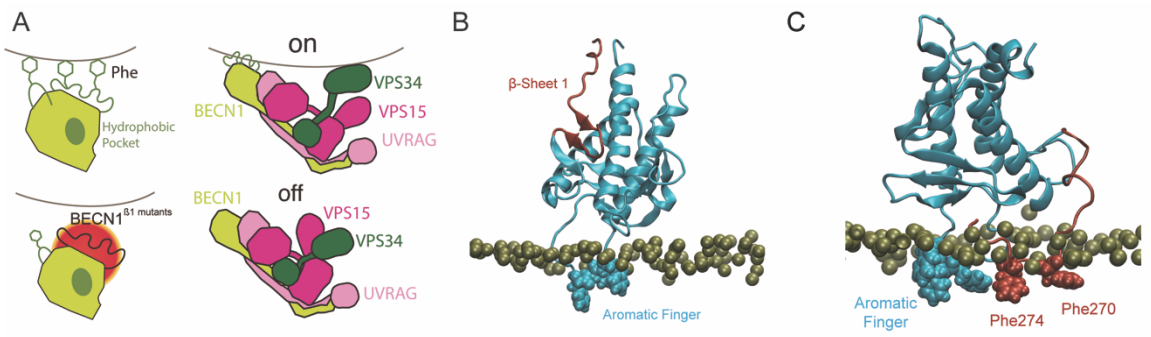

Figure 4.19 Model figure and Molecular Dynamics Simulations on the BECN1 BARA domain

(A) Model for membrane docking by BECN1 BARA domain. The BECN1 BARA domain is located at the tip of the regulatory "left hand" arm of the PI3KC3-C2 complex, where it docks onto membranes, promoting access of the kinase to its lipid substrate. One mode of membrane insertion is through the aromatic finger, the second occurs when the β-sheet of the first β-α repeat flips from its hydrophobic pocket in order bind the membrane. Beta sheet 1 mutants are incapable of binding membrane, leading to reduction in PI3KC3 activity. Representative snapshots of MD simulations of membrane-anchored BECN1 BARA domain with locked beta-sheet 1 (B) or unlocked beta-sheet 1 (C). BECN1 BARA domain in cyan, locked (B) or unlocked (C) beta-sheet 1 (residues 265-287) in red, phosphate atoms of the upper membrane leaflet depicted as golden spheres.

4.3.7 Beta-sheet in BECN1 BARA domain contributes to membrane binding

We carried out a series of GUV-based assays to test the docked model illustrated in Fig. 5B-D. The negative control complex containing the aromatic finger mutation BECN1^{DDD} failed to bind or generate PI(3)P on 50:50 PI:PS GUVs (Figure 4.20), confirming a previous report (Rostislavleva et al. 2015). Consistent with this prediction of the membrane docking model, the BECN1^{BS1PL} complex had minimal membrane binding and activity (Figure 4.19). We further explored the role of individual BARA β-sheet 1 residues using GUV assays of the hydrophobic anchor residues Phe270 and Phe274, and Rubicon binding residues Trp277 and His278. Phe270 and Phe274 has two roles in the model. They are the major anchors that lodge β-sheet 1 in the BARA domain hydrophobic core, but they are also putative membrane anchors in the extruded, membrane-bound state (Figure 4.19). The double mutant F^{270}S/F^{274}S (BECN1^{FF-SS}) essentially eliminates membrane binding and activity (Figure 4.20). We tested whether the solvent-exposed residues Trp277 and His278 (Figure 4.20) might have a dual role in Rubicon binding and membrane anchoring. However, the double mutant BECN1^{WH-DD} has essentially wild-type activity (Figure 4.20), consistent with the docked structure from the MD simulation. These data highlight the role of the two conserved Phe as the major membrane anchors within β-sheet 1.

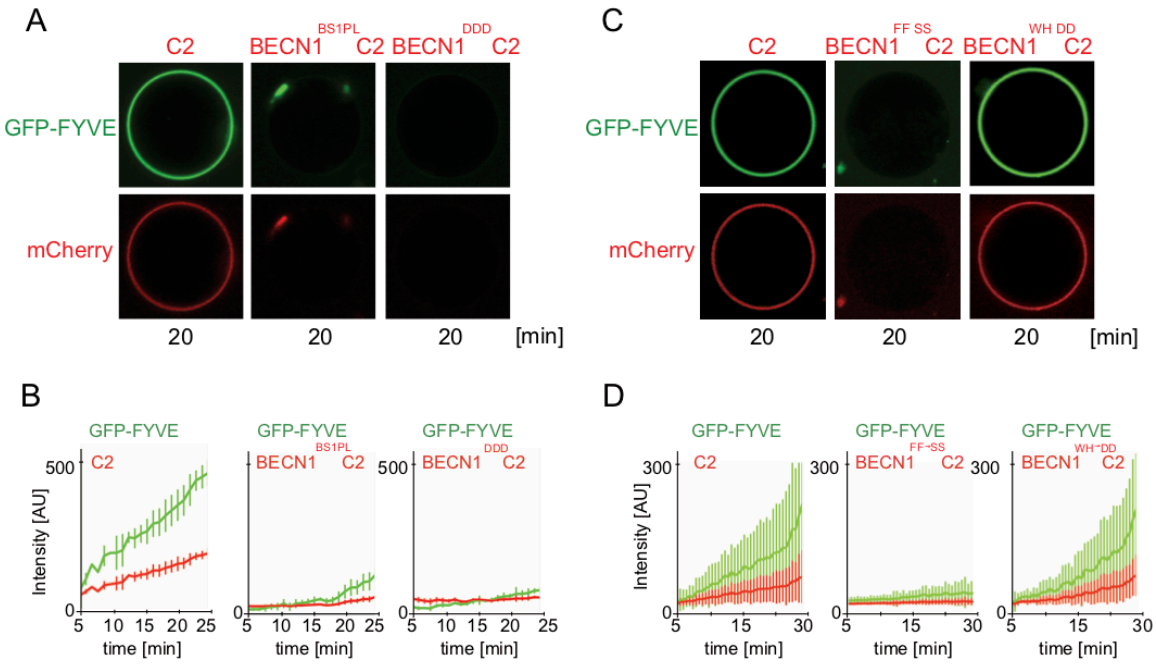

Figure 4.20 BECN1 BARA mutants

Confocal images of GUVs showing the binding of FYVE domain (green) and different PI3KC3 complexes (red). GUVs were incubated with C2, BECN1^{BS1PL}-C2, or BECN1^{DDD}-C2 complex respectively. (A) Quantitation of the reaction kinetics on the membrane from individual GUV tracing in (B) (see Methods, Mean ± Stddev; C2 N = 13, BECN1^{BS1PL}-C2 N = 7, BECN1^{DDD}-C2 N = 8). (C) Confocal images of GUVs showing the binding of FYVE domain (green) and different PI3KC3 complexes (red). GUVs were incubated with C2, BECN1$^{FF→SS}$-C2, or BECN1$^{WH→DD}$-C2 complex respectively. (D) Quantitation of the reaction kinetics on the membrane from individual GUV tracing in (C) (Mean ± Stddev; C2 N = 20, BECN1$^{FF→SS}$-C2 N = 12, BECN1$^{WH→DD}$-C2 N = 20).

4.3.8 BECN1 autophagy-activating peptide promotes PI3KC3 membrane binding in vitro

It is striking that the sequence of β-sheet 1 corresponds almost exactly to the TBP, which potently induces autophagy and upregulates PI(3)P production in cells (Shoji-Kawata et al. 2013). The function of this peptide requires Phe270 and Phe274, both of which are completely buried in the crystal structure of BECN1 BARA (Huang et al. 2012). This leads to a model for an expanded membrane docking site consisting of the three hydrophobic residues of the aromatic finger and additional Phe and other residues from the β-sheet 1 sequence in a flipped-out conformation (Figure 4.21). This model provides a potential explanation for PI3KC3 activation by the peptide, in which the peptide competes with β-sheet 1 for binding to the rest of the BARA domain, so promoting its extrusion and docking onto the membrane.

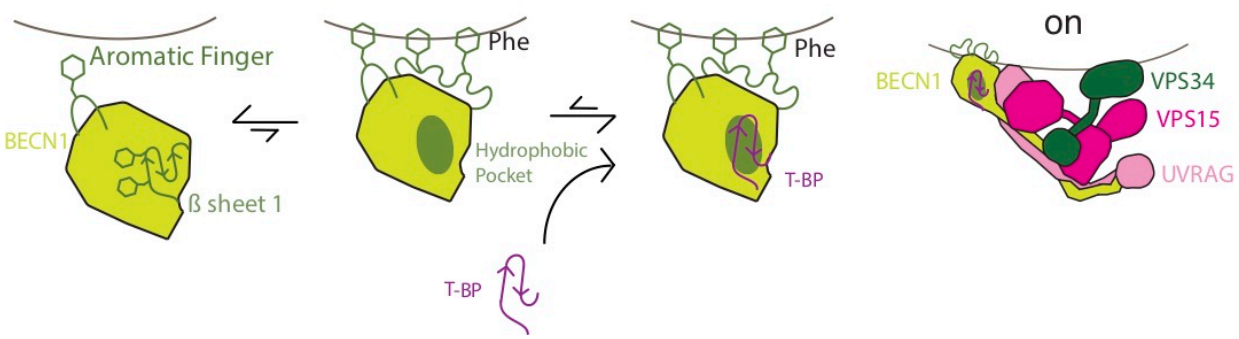

Figure 4.21 Model of TBP activation

Model for PI3KC3 activation by BECN1 peptide. An allosteric switch in beta sheet 1 facilitates this sequence to flip out and bind membranes. This equilibrium favors beta sheet 1 to occupy its hydrophobic pocket over the flipped out state, however, in the presence of T-BP, beta sheet 1 flips out, binds membrane and then activates PI3KC3, as T-BP is present to occupy this hydrophobic pocket.

We tested this hypothesis by conducting SUV and GUV-based activity assays using the TBP peptide. The Tat-containing T-BP construct was used in this experiment even though the cell penetrating ability of the Tat basic residue was not needed in this context. We found that shorter peptides omitting the Tat sequence strongly promoted formation of large PI3KC3-C2 aggregates, precluding further analysis. On the other hand, the basic Tat fusion acted as an anti-aggregating agent. In order to have a low baseline for unstimulated activity and so to avoid saturating the assay, we used liposomes of a composition PC:PE:PI:PS at molar ratio of 60:20:10:10, which is less favorable for PI3KC3 activity. In a SUV-based assay, the addition of 2.5 to 10 μM T-BP to PI3KC3-C2 increased enzyme activity by 2 to 3-fold (Figure 4.22). Control peptides incorporating $F^{270}S/F^{274}S$ (T-BPFS), or with a completely scrambled sequence (T-scrambled), led to no activation (Figure 4.22).

We had predicted on the basis of the BECN1-directed nature of T-BP that it should activate both complexes I and II. As expected, a similar activation of PI3KC3-C1 was observed, along with similar behavior by the control peptides (Figure 4.22). The model posits that β-sheet 1 unfolds such that its hydrophobic residues can insert into membranes. This led us to predict that it would not be possible to rescue the inactive $BECN1^{BS1PL}$ mutant complex with T-BP. As expected, almost no activity was seen for the $BECN1^{BS1PL}$ complex, with or without T-BP (Figure 4.22).

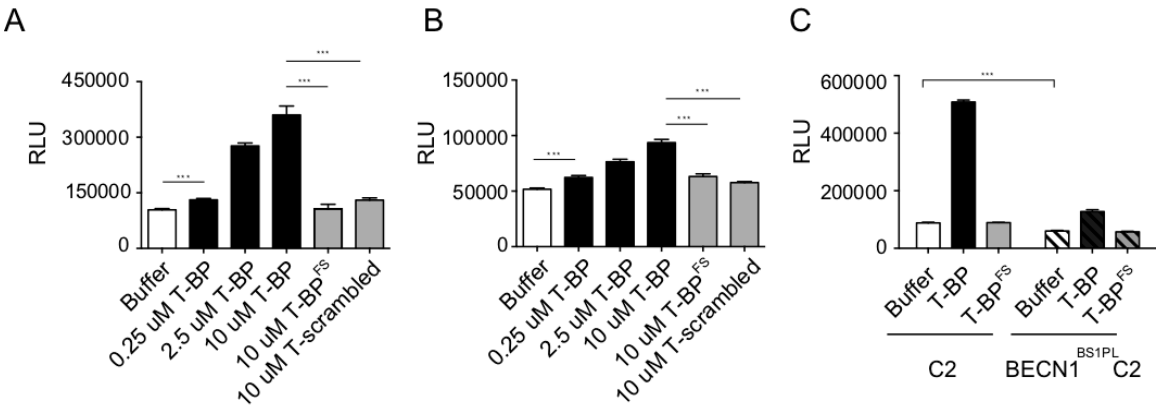

Figure 4.22 Tat-Beclin Peptide enhances activity on SUVs
(A and B) Activities of 25 nM PI3KC3-C2 (A) or PI3KC3-C1 (B) on SUVs in the absence and presence of Tat BECN1 peptide. Data are presented as Mean ± Stddev, n = 3. ***p < 0.001. (C) Activities of 25 nM PI3KC3-C2 or BECN1^{BS1PL}-C2 on SUVs in the absence and presence of Tat BECN1 peptide. Data are presented as Mean ± Stddev, n = 3. ***p < 0.001.

To more directly probe the role of T-BP in promoting membrane binding by PI3KC3, we applied the GUV assay to monitor PI3KC3 membrane binding and PI(3)P production in parallel, using a PC:PE:PI:PS (40:20:20:20) composition. These studies were carried out for 5 min instead of the longer times shown in earlier GUV figures, as peptide-induced deformations of the GUVs were observed at longer time points. We began with a control condition in which essentially no binding or activity could be observed in this lipid composition. Addition of T-BP potently promoted both GUV membrane binding (red channel) and PI(3)P formation by PI3KC3-C2 (Figure 4.23). It was previously established that PI3KC3-C1 requires high curvature membranes for activity (Fan, Nassiri, and Zhong 2011), and that it is nearly inactive on GUVs (Rostislavleva et al. 2015). Consistent with this past observation, minimal PI3KC3-C1 activity was observed, even in the presence of T-BP (Figure 4.23). This contrasted with the robust activation of PI3KC3-C1 in the presence of high curvature SUVs (Figure 4.22).

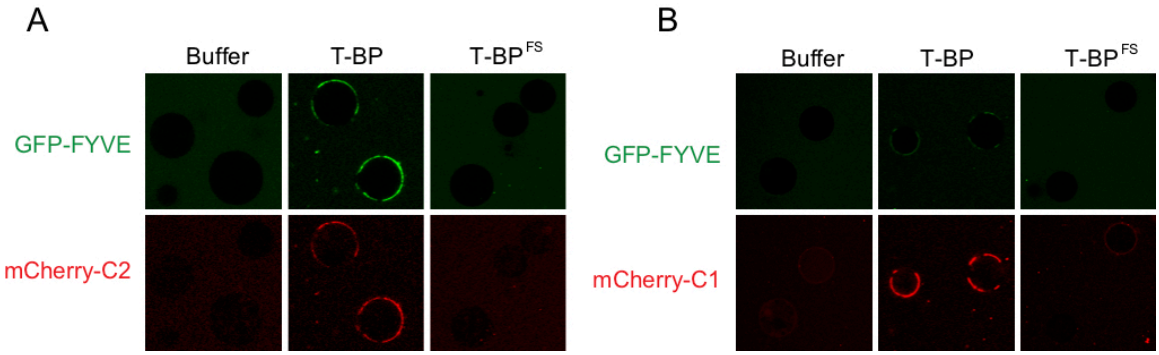

Figure 4.23 TBP on PI3KC3-C1 and -C2 on GUVs
Confocal images of GUVs showing the binding of FYVE domain (green) and PI3KC3-C2 or PI3KC3-C1 (red) in the absence and presence of BECN1 peptide.

Remarkably, membrane binding by PI3KC3-C1 was potently promoted by T-BP, despite its lack of enzyme activity. This shows that both PI3KC3-C1 and -C2 are targeted to membranes by the same BECN1 BARA driven mechanism. These data show that it is the enzyme activity, not simply the membrane binding, of PI3KC3-C1 that requires high membrane curvature. Since both complexes contain the same VPS34 catalytic unit, this surprising observation suggests that in the active conformation of PI3KC3, the complex-specific subunits UVRAG and/or ATG14 must interact with the catalytic domain. This point warrants further investigation. The main conclusion of the peptide studies is that all of the predictions of the T-BP activation model shown in Figure 4.21 were borne out. T-BP activation acts directly on BECN1, it is dependent on the presence of the anchoring Phe residues in the peptide, it depends on an intact hydrophobic sequence in BECN1 β-sheet 1, it is general for both complexes I and II as expected from its BECN1-directed character, and it is capable of driving the complexes onto membranes even in the absence of enzyme activation.

4.3.9 HIV-1 Nef inhibits PI3KC3-C2 in vitro

Because it had previously been proposed that HIV-1 Nef could inhibit PI3KC3 in autophagy (Kyei et al. 2009) and target BECN1 (Shoji-Kawata et al. 2013), we sought to test whether HIV-1 Nef could inhibit PI3KC3 complexes directly in a purified system. We noticed that the N-terminal region of HIV-1 spanning residues 36-64 had sequence homology with the PIKBD of Rubicon (Figure 4.24). This region of Nef is unstructured in most reports (Geyer, Fackler, and Peterlin 2001), but the most conserved DLEK sequence was observed to have a helical conformation by NMR (Grzesiek et al. 1996). Using SUV assays, we found that at 2.5 to 5 μM concentration, HIV-1 NL4-3 Nef inhibited PI3KC3-C2 by up to two-fold (Figure 4.24). Consistent with the idea that Rubicon and Nef inhibit by a similar mechanism, we found no inhibition of PI3KC3-C1 (Figure 4.24). Activity on GUVs was barely detectable in the presence of Nef, and membrane binding was almost completely blocked (Figure 4.25), consistent with an enzyme inhibition mechanism acting at the stage of membrane docking. Mutation of the DLEK sequence to poly-Ala reversed the ability of Nef to inhibit PI3KC3-C2 on GUVs, confirming that inhibition is mediated by the predicted Nef PIKBD (Figure 4.24).

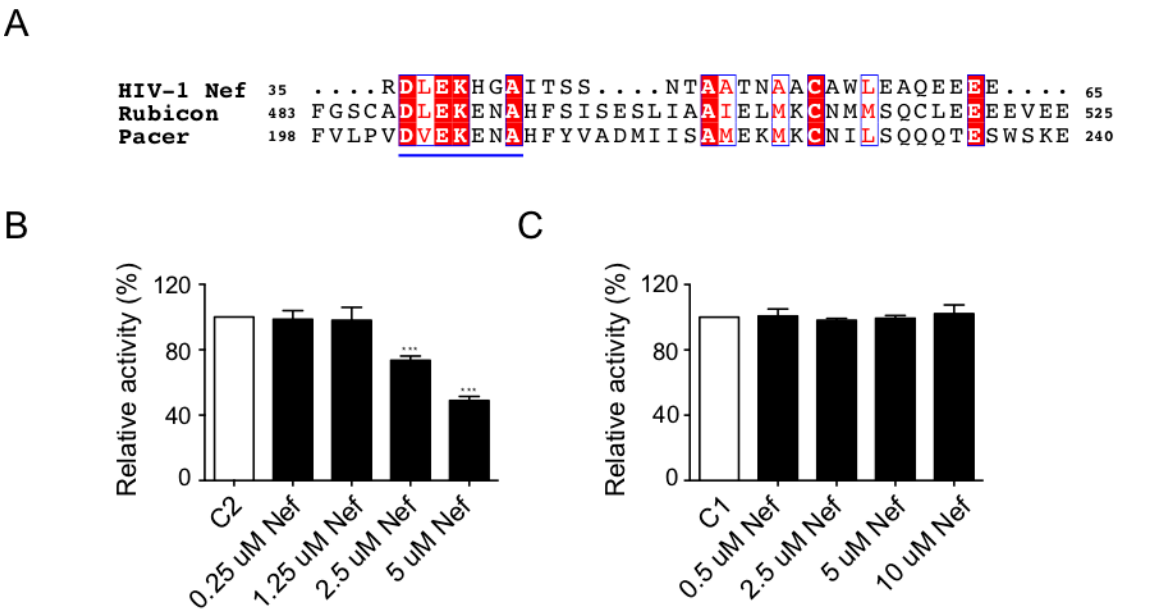

Figure 4.24 HIV-1 Nef inhibits PI3KC3-C2 in vitro

(A) Sequence alignment for HIV-1 Nef, Rubicon and Pacer. Completely conserved regions among the proteins are colored bright and predominantly conserved regions are enclosed in blue boxes. Residues that were included in the Rubicon mutant that knocked out binding and was used in the cell studies are underlined. (B and C) Activities of 25 nM PI3KC3-C2 (B) or PI3KC3-C1 (C) on SUVs in the absence and presence of HIV-1 Nef. Data are presented as Mean ± Stddev, n = 3. ***p < 0.001.

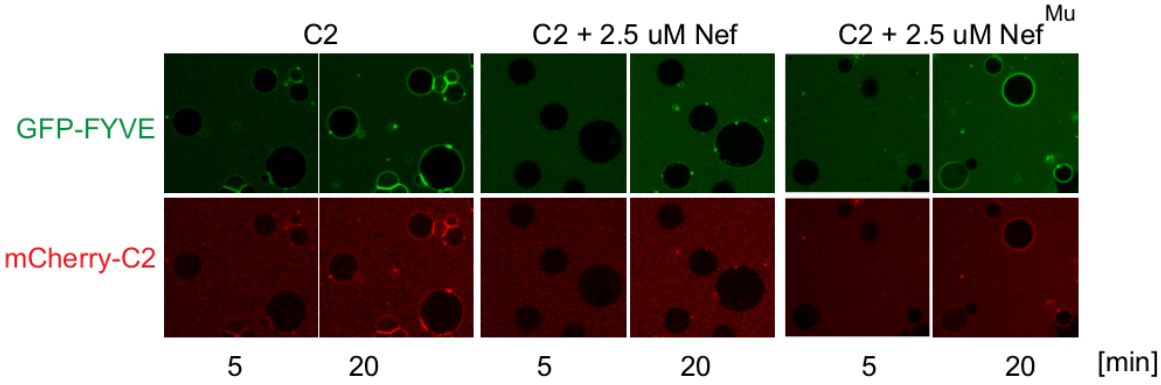

Figure 4.25 HIV-1 Nef inhibits PI3KC3-C2 in vitro

Confocal images of GUVs showing the binding of FYVE domain (green) and PI3KC3-C2 (red) in the presence of wild type Nef and a Nef mutant in the putative C2 binding site ("Nef^{Mu}", conserved DLEK to AAAA).

4.4 Discussion

In the study, we were able to reach broad conclusions about how BECN1 membrane binding is regulated by studying its inhibition by Rubicon. Rubicon was discovered as an inhibitory subunit of PI3KC3-C2 (Matsunaga et al. 2009; Sun et al. 2010; Sun et al. 2011; Yun Zhong et al. 2009a; Tabata et al. 2010). Rubicon is important in its own right as a widely expressed autophagy inhibitor

and an exemplar of a larger family of related proteins. Our structural and mutational results show that inhibition and binding are driven strongly by the BECN1 interaction, but also by interactions with UVRAG BARA2. Consistent with this, we replicated in vitro the previous biological observations that Rubicon binds to PI3KC3-C2 much more strongly than -C1. Rubicon is a positive regulator of LC3-associated phagocytosis (Martinez et al. 2015), a pathway whose machinery partially overlaps with that of autophagy. It remains to be seen how the results presented here bear on the role of Rubicon in this distinct pathway. With respect to the generality of the findings beyond Rubicon itself, Pacer also contains a region similar to the critical PIKBD-α1 BECN1 inhibitory region, and this region has been shown to contribute to Pacer's interaction with PI3KC3-C2 (Cheng et al. 2017). We found that HIV-1 Nef also contains such a sequence, and confirmed that HIV-1 Nef directly inhibits PI3KC3-C2, but not PI3KC3-C1, on GUV membranes.

Our observation that T-BP is capable of strongly activating both PI3KC3-C1 and C2 in a purified system establishes a new mechanism for direct BECN1 and PI3KC3 activation, and helps explain why T-BP is such a potent and broad-based activator of autophagy. T-BP has another mode of action in that it binds to an autophagy inhibitor, Golgi-associated plant pathogenesis-related protein 1 (GAPR-1) (Shoji-Kawata et al. 2013), and thereby reverses inhibition by GAPR-1. T-BP induces autophagy more potently than GAPR-1 knockdown in some contexts, however, leading Shoji-Kawata et al. (2013) to propose that other unknown mechanisms likely worked in parallel. Here, we have identified such a mechanism. We found that BECN1 itself is a target of T-BP, that both PI3KC3 complexes are potently activated by T-BP. The BECN1 BARA itself therefore appears to be an attractive target for the creation of novel autophagy inducing agents.

BECN1 is a key node in the autophagic interactome (Levine et al. 2016) yet as the smallest of the three non-catalytic subunits of PI3KC3 complexes, it has not been completely clear why BECN1 evolved to be such an important focal point for autophagy regulation. The results described here highlight the centrality of membrane docking by the BARA domain both as a mechanism for BECN1 to promote PI(3)P formation and autophagy, and as a pivot point for regulation. Binding of the regulators Bcl-2 (Oberstein, Jeffrey, and Shi 2007) and NRBF2 (Ohashi et al. 2016; L. N. Young et al. 2016), and phosphoregulation (Russell et al. 2013) of BECN1, are centered near its N-terminus, remote from its C-terminal BARA domain. While Rubicon, HIV-1 Nef, and T-BP regulate the strength of membrane binding, these other above-mentioned interactors and modifications seem to modulate the strength of the BECN1-VPS34 interaction. These ideas and the data provided here lead to a simple overarching scheme for PI3KC3 regulation by BECN1. N-terminus-directed regulation controls the affinity of the BECN1 subcomplex for the VPS34-VPS15 subcomplex in this scheme, while C-terminus-direct regulation by Rubicon controls the affinity of BECN1 for the membrane.

Here, we showed that several prominent positive and negative modulators of autophagy and PI3KC3 activity, namely Rubicon, HIV-1 Nef, and T-BP, act by

directly controlling the ability of PI3KC3 complexes to dock onto membranes via the BECN1 BARA domain (Figure 4.21). While it has been clear for some time that BECN1 is a central node for autophagy regulation, it has been much less clear how BECN1 might actually switch autophagy on and off. The observations here have finally shed light on this question by showing how BECN1 BARA dynamics can be modulated to bring lipid kinase activity above or below baseline, providing a versatile bidirectional regulatory mechanism. This mechanism explains autophagy regulation that is known to occur in normal physiology and in infection, and is harnessed by a potential therapeutic autophagy inducer.

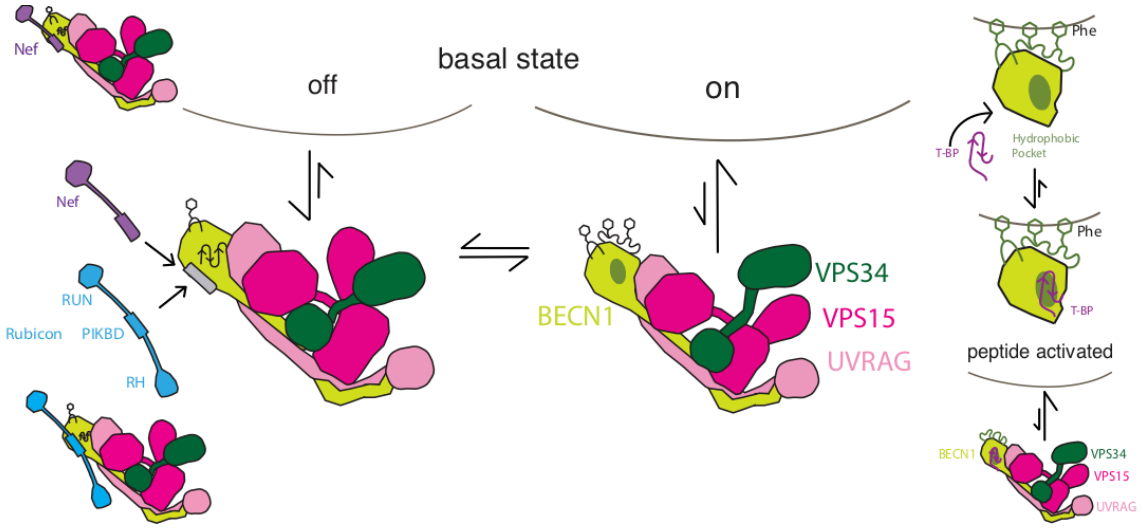

Figure 4.24 Model figure
Schematic for bidirectional regulation of PI3KC3 in normal physiology, infection, and therapeutic intervention.

4.5 Methods

4.5.1 Plasmid construction

Synthetic DNA encoding human RUBCN was cloned into the pCAG vector with an N-terminal MBP tag followed by a tobacco etch virus (TEV) cleavage site. RUBCN truncation constructs and mutants were subcloned into the pCAG vector with MBP tag. Genes encoding PI3KC3 core subunits were cloned into the pCAG vector with an N-terminal twin-STREP-FLAG tag. BECN1-(GGS)4-RUBCN fusion and BECN1 mutants were subcloned to the pCAG vector with twin-STREP-FLAG tag. For BECN1BS1PLconstruct, the residues 262-287 of wild type BECN1 were replaced by a polar peptide comprises the amino acid sequence GSDEASEGSGLSSPSALN-SLSSPSAL. DNA encoding UVRAG was cloned into the pCAG vector with an N-terminal GST tag followed by a TEV cleavage site. The GST tag was replaced by mCherry to generate the mCherry tagged UVRAG construct. mStrawberry-Rubicon PIKBD mutant was constructed from mStrawberry-human Rubicon WT (Tabata et al., Mol. Biol. Cell,2010). The amino

acids of Rubicon (488 DELKENAHF 496) were replaced by Alanine to make Rubicon PIKBD mutant. All constructs were verified by DNA sequencing.

4.5.2 Protein expression and purification

Protein expression and purification was performed as described previously (Baskaran et al., 2014; Stjepanovic et al., 2017). Transient transfections were performed using polyethylenimine (Polysciences), and cells were harvested after 48 to 72 h expression. Cells were lysed with lysis buffer (50 mM HEPES pH 7.4, 1% Triton X-100, 200 mM NaCl, 1 mM MgCl2, 10% glycerol, and 1mM TCEP) supplemented with EDTA free protease inhibitors (Roche). The lysate was clarified by centrifugation (15000 rpm for 1 h at 4 °C) and incubated with glutathione Sepharose 4B (GE Healthcare) or amylose resin (New England Biolabs) for 2 h at 4 °C, applied to a gravity column, and washed extensively with wash buffer (50 mM HEPES pH 8.0, 200 mM NaCl, 1 mM MgCl2, and 1mM TCEP). The target complexes were eluted with wash buffer containing 50 mM reduced glutathione or 20 mM maltose, and treated with TEV protease at 4 °C overnight. TEV-treated complexes were loaded on a Strep-Tactin Sepharose gravity flow column (IBA, GmbH) at 4 °C. The target complexes were eluted with wash buffer containing 10 mM desthiobiotin (Sigma), and applied to Superose 6 16/50 (GE Healthcare) column equilibrated with gel filtration buffer (20 mM HEPES pH 8.0, 200 mM NaCl, 1 **mM MgCl2, and 1** mM TCEP). Peak fractions were collected and used immediately for subsequent assays.

4.5.3 Pull down assay

Transient transfection was performed in 20 mL suspended cells for each condition. Cells were harvested after 48 h expression, and lysed with 2 mL lysis buffer (50 mM HEPES pH 7.4, 1% Triton X-100, 200 mM NaCl, 1 mM MgCl2, 10% glycerol, 1mM TCEP and protease inhibitors). The lysate was clarified by centrifugation (15000 x g for 30 min, at 4 °C) and incubated with 30 µL glutathione Sepharose 4B or amylose resin for 4 h at 4 °C. The protein-bound resin was washed with lysis buffer for 5 times, and then wash buffer (50 mM HEPES pH 8.0, 200 mM NaCl, 1 mM MgCl2, and 1mM TCEP) for 3 times. The proteins were eluted with 100 µL wash buffer containing 50 mM reduced glutathione or 20 mM maltose. The eluted proteins were applied to SDS–PAGE for analysis.

4.5.4 HDX-MS

Amide hydrogen exchange mass spectrometry (HDX-MS) was initiated by a 10-fold dilution of stock wild type and Rubicon fragment associated PI3KC3-C2 complexes (5 µM) into D2O buffer containing 20 mM HEPES (pD 8.0), 200 mM NaCl, 1 mM MgCl2 at 30 °C. Incubations in deuterated buffer were performed for 10 to 90 s. Backbone amide exchange was quenched at 0 °C by the addition of ice-cold quench buffer (400 mM KH2PO4/H3PO4, pH 2.2). Quenched samples were injected onto a chilled HPLC setup with in-line peptic digestion and desalting steps. Desalted peptides were eluted and directly analyzed by an Orbitrap Discovery mass spectrometer (Thermo Scientific). Initial peptide

identification was performed via tandem MS/MS experiments. A Proteome Discoverer 2.1 (Thermo Scientific) search was used for peptide identification. Mass analysis of the peptide centroids was performed using HDExaminer (Sierra Analytics), followed by manual verification of each peptide. The relative deuteron content of the peptic peptides covering PI3KC3-C2 complexes was determined from the centroid of the molecular ion isotope envelope. The average error (n = 3) of all time points and conditions for each HDX experiment was approximately 0.7%.

4.5.5 Lipid kinase assay with SUVs

Small unilamellar vesicles (SUVs) were used as the lipid substrate for lipid kinase assay. Briefly, lipid mixture with a molar composition of 60% POPC, 20% POPE, 10% POPS, and 10% POPI or 60% brain PC, 20% brain PE, 10% brain PS, and 10% liver PI was desiccated overnight, resuspended in SUV buffer (20 mM HEPES pH 8.0, 200 mM NaCl), and then sonicated to make a 0.5 mg/ml stock. The lipid kinase assay was carried out using ADP-Glo Kinase Assay (Promega). Freshly purified PI3KC3-C2 and Rubicon associated PI3KC3-C2 complexes were pre-incubated with sonicated SUVs in the reaction buffer (20 mM HEPES pH 8.0, 200 mM NaCl, 1 mM MnCl2, 1mM TCEP). The reaction was initiated by adding 10 × ATP (250 μM), and incubated at room temperature for indicated time. Control reactions without ATP were set up for all proteins. An ATP-depletion reagent was added to terminate the lipid kinase reaction, deplete the remaining ATP, leaving only ADP. Then a kinase detection reagent was added to convert ADP to ATP, which is used in a coupled luciferase reaction. The luminescent output was measured with a GloMax-Multi detection system (Promega) and was correlated with kinase activity.

4.5.6 Negative stain EM sample prep, data collection, and processing

Negatively stained samples of PI3KC3-C2:MBP-Rubicon PIKBD were prepared on continuous carbon grids that had been plasma cleaned in a 10% O2 atmosphere for 10 s using a Solarus plasma cleaner (Gatan Inc., Pleasanton, CA). Procedures were generally as previously reported (Baskaran et al., 2014; Young et al., 2016). 4 μl of PI3KC3-C2:MBP-Rubicon PIKBD at a concentration of 30 nM in 20 mM Tris, pH 8.0, 200 mM NaCl, 2 mM MgCl2, 1 mM TCEP, and 3% trehalose were placed on the grids and incubated for 30 s. The grids were floated on four successive 40 μl drops of 1% uranyl formate solution incubating for 10s on each drop. The stained grids were blotted to near dryness with a filter paper and air-dried. PI3KC3-C2:MBP-Rubicon PIKBD sample was imaged using an FEI Tecnai 20 electron microscope (FEI, Hillsboro, OR) operated at 120 keV at a nominal magnification of 81,000x (1.5 Å per pixel) equipped with a US4000 CCD camera (Gatan) using a defocus range of −2.5 to −1.0 μm with an electron dose of 35 e−/Å2. Data was collected via Leginon data collection software (Suloway et al., 2005). The power spectrum of each image was estimated with gCTF and particles were picked template-free with Gautomatch. Images were processed in RELION (Kimanius et al., 2016) to generate 2D reference-free classifications.

4.5.7 Cryo-EM sample preparation and data acquisition

Protochips C-flat 2/2 of 400 mesh grids were coated with a carbon support, and glow-discharged in the presence of amylamine for 60 seconds. A sample of PI3KC3-C2 containing the following subunits: VPS15-VPS34 fusion, UVRAG, BECN1-12 residue linker-Rubicon PIKBD fusion was incubated on a grid for 1 minute at 15˚C, 100% humidity. The sample was protected with 0.01% (v/v) NP40 substitute and 1% (w/v) trehalose. The sample was blotted for 3 seconds and then plunge frozen within Mark IV Vitrobot into a 50/50 mix of ethane/propane. The grid was transferred to a FEI Krios microscope operating at 300 kV and collected with a GIF Quantum energy filter (Gatan), and images acquired with a Gatan K2 Direct Electron Detector with a final pixel size of 0.575 Å. Defocus was randomized between -1.3 to -3.3 microns. SerialEM was used to collect an automated dataset of 4,202 micrographs.

4.5.8 Cryo-EM image processing

Individual frames were motion corrected with MotionCor2 (Li et al., 2013) with internal two-fold Fourier binning, discarding the initial two frames, 5 by 5 patch based alignment and dose-weighing up the total exposure of 59.7 electrons/A2. The contrast transfer function was estimated on the full non-dose weighted micrographs with gCTF version 1.06 (Zhang, 2016). Non-template based picking was performed from non-dose weighted micrographs in Gautomatch, resulting in 388K particles. Particles were extracted in a 352 pixel box, with 8-fold binning and subjected to 2D classification in Relion-2.0 *(Kimanius* et al., 2016). Following 2D, classes with strong features corresponding to 95K particles were selected and an ab initio reconstruction was generated in cryoSPARC (Punjani et al., 2017), resulting in an 8.8 Å map with a Bfactor of -730. The particle angles and reference volume were imported and refined in Relion-2.0 to 8.1 Å and a bfactor of -439. Template-based picking was performed with Gautomatch using seven 2D class averages from Relion-2.0, using the 2D projections from the 8.1 Å reconstruction. The resulting 921,474 particles were extracted and binned by 8, then subjected to 2D classification, cleaning up the data to 622,843 particles. These particles then went through 3D classification, still using bin 8. The resulting 305,942 particles were re-extracted at bin 2, and re-centered. Another round of 3D classification was performed on these 305,942 particles, using a reference map low pass filtered to 60 Å, tau was set 10. The resulting most populated class of 133,007 particles was further refined to 8.6 Å, with a bfactor of -454 Å2. Then, 2D classification without angular sampling was performed, selecting 101,903 particles that were refined to 7.7 Å with a bfactor of -393 Å2. These 101,903 particles were subjected to 3D classification, without angular sampling, with tau set to 16. Two of the three classes were selected, resulting in 72,869 particles, which refined to 7.7 Å and a bfactor of -342 Å2. These 72,869 particles were subjected to another round of 2D classification without angular sampling. A final selection of 42,708 particles were refined to 6.8 Å with a bfactor of -50 Å2.

4.5.9 CryoEM Modeling

A model from a 4.5 Å crystal structure (PDB: 5DFZ) was placed into a 8.6 Å reconstruction using UCSF Chimera using the fit Map in Model tool. In Chimera, model 5DFZ (in Chimera, #0) was split into 6 chains (command: split #0), the nanobody (chain E) and putative N-terminus of Atg6 (chain G) were removed (select #0:.G; delete selected), leaving yAtg6 (hBECN1), yVps38 (hUVRAG), yVps15 (hVPS15), and yVps34 (hVPS34). The models for the kinase domains of yVps34 and yVps15 were then selected and deleted. The remaining models were then fit sequentially within the 8.6 Å EM volume generated in this study (in Chimera, map #1). This volume (map #1) was then colored based on its physical proximity to the now fitted model (#0) and then segmented, creating a new EM volume. This newly generated reference volume allowed the very flexible VPS34 and VPS15 kinase domains to be excluded from further refinements. This volume was saved and imported into Relion-2.0. When the refinement reached 7.7 Å, an extra helix, possibly accounting for Rubicon PIKBD could be visualized, the model was then updated to include the human crystal structure of the BECN1 BARA domain, thereby replacing the yAtg6 BARA domain of model 5DFZ. The "OH" (overlap helix) of 4DDP was removed because in the full 4-subunit apo complex, these residues correspond to the C-terminal part of the BECN1 coiled-coil. The OH was replaced with a longer helix of 34 residues corresponding to Rubicon PIKBD. The rest of the model was adjusted, manually, in Coot using real-space refinement tools, and placement of helices when appropriate. For VPS15, Swiss-modeler was used to replace the yeast model with numbering from human residues. For the C2 VPS34 domain, and BECN1 and UVRAG coiled coils, sequence alignments were used.

4.5.10 Giant unilamellar vesicle (GUV) assay

GUVs were prepared as previously described (Wollert et al., 2009). Lipids with different compositions were spread on indium-tin oxide-coated glass slides, and dried overnight in a desiccator. For comparing the activity between different PI3KC3 complexes, lipid mixture with a molar composition of 50% brain PS and 50% liver PI was used. For the BECN1 peptide assay, lipid mixture with molar composition of 40% brain PC, 20 % brain PE, 20% brain PS, and 20% liver PI was used. The lipid film was electro-formed in 400 mM sucrose for 1 h at 60 °C (10 HZ, 1V). GUVs were then stored at room temperature and used within 48 h. Freshly purified mCherry tagged PI3KC3-C2 complexes and GUVs were incubated in GUV dilution buffer (20 mM HEPES pH 8.0, 190 mM NaCl, 1 mM MnCl2, 1 mM TCEP, 20 μM ATP) at room temperature. A GFP tagged FYVE domain of human Hrs was used as the probe of PI(3)P. The concentration of PI3KC3 was 50 nM, and GFP-FYVE concentration was 7 uM. After 5 min incubation, time-lapse images were acquired in multitracking mode on a Nikon A1 confocal microscope with a 63 × Plan Apochromat 1.4 NA objective. Identical laser power and gain settings were used during the course of all conditions.

4.5.11 GUV image quantitation

Data analysis of GUV fluorescence intensities over time was done computationally by a custom developed iPython (Perez and Granger, 2007) code. To mitigate drift of the GUVs, two-channel GUV movies were split into individual channels and frames. Using scikit-image (van der Walt et al., 2014) and OpenCV (Bradski, 2000), for each frame, a thresholding and Hough circle transformation was performed to automatically detect the outline of GUVs and retrieve their individual intensities. Detected GUVs were then matched frame by frame in the same movie to obtain intensity trajectories. Multiple intensity trajectories were calculated from multiple data-sets and the average and standard deviation calculated and reported.

4.5.11 Cell culture

Cells were grown in DMEM supplemented with 10% FBS, 2 mM glutamine, 100 U/ml penicillin, and 100 U/ml streptomycin in a 37°C incubator with a humidified, 5% CO2 atmosphere. Transient transfections were performed using Lipofectamine 2000 (Invitrogen) according to the manufacturer's instructions. For FYVE puncta analysis, U2OS cells were starved with EBSS for 2 h after transfection with GFP tagged 2 × FYVE domain of EEA1 and Flag tagged Rubicon, cells were then fixed in 4% formaldehyde for 10 min at room temperature. After washing twice in PBS, cells were incubated in PBS containing 10% FBS and 0.1% saponin to block nonspecific sites of antibody adsorption. The cells were then incubated with appropriate anti-Flag antibody (Sigma) and Alexa Fluor 546 secondary antibody (ThermoFisher) in 0.1% saponin. Confocal images were captured in multitracking mode on a Nikon A1 confocal microscope with a 63 × Plan Apochromat 1.4 NA objective. To quantify the number of GFP-FYVE puncta, a total of 50 cells were recorded and analyzed with Image J.

4.5.12 Generation of the Rubicon KO cell line using CRISPR/Cas9 gene system

The Rubicon KO cell line was generated using CRISPR guide RNAs (5'-cacccgggggtccaagttgccaa -3', and 5'- aaacttggcaacttggacccccg -3') that targets exon 6 in chromosome 3; the common exon of all protein coded splicing variants. Annealed guide RNAs oligonucleotides were inserted into the px458 vector, and the gRNA construct was transfected into HeLa cells using ViaFect™ (Promega) transfection reagent. GFP positive single-cells were sorted into the 96 wells plate by FACS. Candidate single-clone colonies were verified by immunoblotting using anti-Rubicon antibody (D9F7, lot#1, 8465S, cell signaling technology) and Genomic DNA sequence (amplifying primer set; 5'-atatggatccccactggtgacagtgagtgtc -3', and 5'- atatgaattctttcagtctctgcactagcca -3'). The selected Rubicon KO clone had +1 and -7 frameshift indels, and no Rubicon and fragmented gene products bands by immunoblotting.

4.5.13 Autophagic flux assay

The autophagic flux assay was performed as described previously (Mizushima et al., 2010). Briefly, after twenty-four hours of the transfection with mStrawberry,

Rubicon, or Rubicon-mutant to the WT and Rubicon KO cells using Lipofectamine 2000 reagent (Invitrogen), cells were treated with 125 nM of Bafilomycin A1 (BioViotica, Dransfeld, Germany), a lysosomal inhibitor, for 2 hours in EBSS. Harvested cells were analyzed by the western blotting with anti-LC3 antibody (MBL), and the autophagic flux was estimated by the comparison of two samples with or without the inhibitor treatment. The transfection efficacies and loading protein amounts were confirmed by the western blotting with anti-RFP antibody (MBL) and Ponceau S staining, respectively.

4.5.14 Molecular dynamics simulations

The MD simulations of the membrane-attached BECN1 BARA domain started from the crystal structure (PDB ID: 4DDP (Huang et al., 2012)). We removed the overlap helix (residues 248-264), used Modeller (Benjamin and Andrej, 2016) to add loop residues 265-268, 387, and 448-450 missing in 4DDP, and capped N- and C-termini by acetylation and amidation, respectively. The structure was protonated at pH 8 using the H++ webserver (http://biophysics.cs.vt.edu) (Anandakrishnan et al., 2012). We placed the protein near a membrane bilayer containing 40% DOPC, 20% DOPE, 20% DOPS, and 20% POPI, as prepared with charmm-gui (http://www.charmm-gui.org) (Jo et al., 2008). The system was solvated with TIP3P water (Jorgensen et al., 1983) and ions (200 mM NaCl). Steepest-descent energy minimization was followed by a short (1 ns) pre-equilibration MD run using the Gromacs molecular dynamics software (vers. 2016.5) (Abraham et al., 2015) using the charmm36 force field for lipids (Klauda et al., 2010) and proteins (Best et al., 2012). All simulations were carried out at 300 K and, if at constant pressure, at 1 bar with semiisotropic pressure coupling. The aromatic finger (residues 359-361) was pulled inside the membrane. All pulling was done in an NVT ensemble at a constant force of 500 kJ mol-1 nm-1. Once the aromatic finger was inserted into the membrane, we equilibrated the system in an NPT ensemble for 23 ns, applying soft restraints on the z-positions of the aromatic finger residues. After removing the position restraints, we performed 335 ns of MD simulation in an NPT ensemble using the velocity-rescaling thermostat (Bussi et al., 2007) and the Parrinello-Rahman barostat (Parrinello and Rahman, 1981).

Simulations with unlocked β-sheet 1, residues 265-287 were modeled as a loop using Modeller (Benjamin and Andrej, 2016). Protonation, system preparation, and pre-equilibration followed the preceding protocol. The aromatic finger was pulled into a membrane of the same composition, followed by 30 ns of equilibration. Subsequently, Phe270 and Phe274 were pulled into the membrane with restraints on the z-positions of the anchored aromatic finger. The system was equilibrated in an NPT ensemble for 70 ns with soft z-position restraints on the aromatic finger, and on Phe270 and Phe274. The restraints were then removed and a simulation run was carried out for 242 ns.

References

Abeliovich, Hagai, Chao Zhang, William A Dunn, Kevan M Shokat, and Daniel J Klionsky. 2003. “Chemical Genetic Analysis of Apg1 Reveals A Non- Kinase Role in the Induction of Autophagy” 14 (February): 477–90. doi:10.1091/mbc.E02.

Alemu, Endalkachew Ashenafi, Trond Lamark, Knut Martin Torgersen, Aasa Birna Birgisdottir, Kenneth Bowitz Larsen, Ashish Jain, Hallvard Olsvik, Aud Øvervatn, Vladimir Kirkin, and Terje Johansen. 2012. “ATG8 Family Proteins Act as Scaffolds for Assembly of the ULK Complex: Sequence Requirements for LC3-Interacting Region (LIR) Motifs.” *Journal of Biological Chemistry* 287 (47): 39275–90. doi:10.1074/jbc.M112.378109.

Alers, Sebastian, Antje S Löffler, Florian Paasch, Alexandra M Dieterle, Hildegard Keppeler, Kirsten Lauber, David G Campbell, et al. 2011. “Atg13 and FIP200 Act Independently of Ulk1 and Ulk2 in Autophagy Induction” 8627. doi:10.4161/auto.7.12.18027.

Araki, Yasuhiro, Wei Chi Ku, Manami Akioka, Alexander I. May, Yu Hayashi, Fumio Arisaka, Yasushi Ishihama, and Yoshinori Ohsumi. 2013. “Atg38 Is Required for Autophagy-Specific Phosphatidylinositol 3-Kinase Complex Integrity.” *Journal of Cell Biology* 203 (2): 299–313. doi:10.1083/jcb.201304123.

Axe, Elizabeth L., Simon A. Walker, Maria Manifava, Priya Chandra, H. Llewelyn Roderick, Anja Habermann, Gareth Griffiths, and Nicholas T. Ktistakis. 2008. “Autophagosome Formation from Membrane Compartments Enriched in Phosphatidylinositol 3-Phosphate and Dynamically Connected to the Endoplasmic Reticulum.” *Journal of Cell Biology* 182 (4): 685–701. doi:10.1083/jcb.200803137.

Bach, Markus, Mark Larance, David E. James, and Georg Ramm. 2011. “The Serine/Threonine Kinase ULK1 Is a Target of Multiple Phosphorylation Events.” *Biochemical Journal* 440 (2): 283–91. doi:10.1042/bj20101894.

Backer, J. M. 2016. “The Intricate Regulation and Complex Functions of the Class III Phosphoinositide 3-Kinase Vps34.” *Biochemical Journal* 473 (15): 2251–71. doi:10.1042/BCJ20160170.

Backer, Jonathan M. 2008. “The Regulation and Function of Class III PI3Ks: Novel Roles for Vps34.” *The Biochemical Journal* 410 (1): 1–17. doi:10.1042/BJ20071427.

Bar-Peled, Liron, and David M. Sabatini. 2014. “Regulation of MTORC1 by Amino Acids.” *Trends in Cell Biology* 24 (7). Elsevier Ltd: 400–406. doi:10.1016/j.tcb.2014.03.003.

Baskaran, Sulochanadevi, Lars-Anders Carlson, Goran Stjepanovic, Lindsey N Young, Do Jin Kim, Patricia Grob, Robin E Stanley, Eva Nogales, and James H Hurley. 2014. “Architecture and Dynamics of the Autophagic Phosphatidylinositol 3-Kinase Complex.” *ELife* 3. doi:10.7554/eLife.05115.001.

Behrends, Christian, Mathew E Sowa, Steven P Gygi, and J Wade Harper. 2010. “Network Organization of the Human Autophagy System.” *Nature* 466

(7302). Nature Publishing Group: 68–76. doi:10.1038/nature09204.
Bento, Carla F, Maurizio Renna, Ghita Ghislat, Claudia Puri, Avraham Ashkenazi, Mariella Vicinanza, Fiona M Menzies, and David C Rubinsztein. 2016. “Mammalian Autophagy : How Does It Work ?,” no. January: 1–29. doi:10.1146/annurev-biochem-060815-014556.
Brandizzi, Federica, and Charles Barlowe. 2013. “Organization of the ER – Golgi Interface for Membrane Traffic Control.” *Nature Publishing Group* 14 (6). Nature Publishing Group: 382–92. doi:10.1038/nrm3588.
Cao, Yanyan, Yichen Wang, Widian F Abi Saab, Fajun Yang, Jeffrey E Pessin, and Jonathan M Backer. 2014. “NRBF2 Regulates Macroautophagy as a Component of VPS34 Complex I,” no. May.
Chan, E. Y. W., A. Longatti, N. C. McKnight, and S. A. Tooze. 2008. “Kinase-Inactivated ULK Proteins Inhibit Autophagy via Their Conserved C-Terminal Domains Using an Atg13-Independent Mechanism.” *Molecular and Cellular Biology* 29 (1): 157–71. doi:10.1128/mcb.01082-08.
Chang, Chunmei, Lindsey N Young, Kyle L Morris, Gerhard Hummer, Tamotsu Yoshimori, James H Hurley, and Johannes Scho. 2019. “Domain Dynamics Article Bidirectional Control of Autophagy by BECN1 BARA Domain Dynamics,” 339–53. doi:10.1016/j.molcel.2018.10.035.
Cheng, Xiawei, Xiuling Ma, Xianming Ding, Lin Li, Xiao Jiang, Zhirong Shen, She Chen, Wei Liu, Weihua Gong, and Qiming Sun. 2017. “Pacer Mediates the Function of Class III PI3K and HOPS Complexes in Autophagosome Maturation by Engaging Stx17.” *Molecular Cell* 65 (6). Elsevier Inc.: 1029–1043.e5. doi:10.1016/j.molcel.2017.02.010.
Cheong, Heesun, Tomohiro Yorimitsu, Fulvio Reggiori, Julie Legakis, Chao-Wen Wang, and Daniel Klionsky. 2005. “Atg17 Regulates the Magnitude of the Autophagic Response.” *Molecular Biology of the Cell* 16 (May): 2207–17. doi:10.1091/mbc.E04.
Di Bartolomeo, Sabrina, Marco Corazzari, Francesca Nazio, Serafina Oliverio, Gaia Lisi, Manuela Antonioli, Vittoria Pagliarini, et al. 2010. “The Dynamic Interaction of AMBRA1 with the Dynein Motor Complex Regulates Mammalian Autophagy.” *Journal of Cell Biology* 191 (1): 155–68. doi:10.1083/jcb.201002100.
Diao, Jiajie, Rong Liu, Yueguang Rong, Minglei Zhao, Jing Zhang, Ying Lai, Qiangjun Zhou, et al. 2015. “ATG14 Promotes Membrane Tethering and Fusion of Autophagosomes to Endolysosomes.” *Nature* 520 (7548): 563–66. doi:10.1038/nature14147.
Drin, Guillaume, Romain Gautier, Thomas Boehmer, Thomas U Schwartz, and Bruno Antonny. 2007. “A General Amphipathic a -Helical Motif for Sensing Membrane Curvature” 14 (2): 138–46. doi:10.1038/nsmb1194.
Egan, Daniel F, Matthew G H Chun, Mitchell Vamos, Haixia Zou, Juan Rong, J Miller, Hua Jane Lou, et al. 2015. “Small Molecule Inhibition of the Autophagy Kinase ULK1 and Identification of ULK1 Substrates” 59 (2): 285–97. doi:10.1016/j.molcel.2015.05.031.Small.
Faini, Marco, Rainer Beck, Felix T Wieland, and John A G Briggs. 2013. “Vesicle Coats : Structure , Function , and General Principles of Assembly.” *Trends in*

Cell Biology 23 (6). Elsevier Ltd: 279–88. doi:10.1016/j.tcb.2013.01.005.
Fan, Weiliang, Ashley Nassiri, and Qing Zhong. 2011. “Autophagosome Targeting and Membrane Curvature Sensing by Barkor / Atg14 (L)” 108 (19): 7769–74. doi:10.1073/pnas.1016472108.
Feng, Yuchen, Steven K Backues, Misuzu Baba, Jin-mi Heo, J Wade Harper, and Daniel J Klionsky. 2016. “Phosphorylation of Atg9 Regulates Movement to the Phagophore Assembly Site and the Rate of Autophagosome Formation.” *Autophagy* 12 (4). Taylor & Francis: 648–58. doi:10.1080/15548627.2016.1157237.
Fimia, Gian Maria, Anastassia Stoykova, Alessandra Romagnoli, Luigi Giunta, Sabrina Di Bartolomeo, Roberta Nardacci, Marco Corazzari, et al. 2007. “Ambra1 Regulates Autophagy and Development of the Nervous System” 447 (June). doi:10.1038/nature05925.
Fujioka, Yuko, Sho W Suzuki, Hayashi Yamamoto, Chika Kondo-Kakuta, Yayoi Kimura, Hisashi Hirano, Rinji Akada, Fuyuhiko Inagaki, Yoshinori Ohsumi, and Nobuo N Noda. 2014. “Structural Basis of Starvation-Induced Assembly of the Autophagy Initiation Complex.” *Nature Structural & Molecular Biology* 21 (6): 513–21. doi:10.1038/nsmb.2822.
Fujiwara, Nobuyuki, Tatsuya Usui, Takashi Ohama, Koichi Sato, and Experimental Procedures. 2016. “Regulation of Beclin 1 Protein Phosphorylation and Autophagy by Protein Phosphatase 2A (PP2A) and Death-Associated Protein Kinase 3 (DAPK3) *” 291 (20): 10858–66. doi:10.1074/jbc.M115.704908.
Galluzzi, Lorenzo, José Manuel Bravo-san Pedro, Beth Levine, Douglas R Green, and Guido Kroemer. 2017. “Pharmacological Modulation of Autophagy : Therapeutic Potential and Persisting Obstacles.” *Nature Publishing Group* 16 (7). Nature Publishing Group: 487–511. doi:10.1038/nrd.2017.22.
Galluzzi, Lorenzo, Federico Pietrocola, José Manuel Bravo-San Pedro, Ravi K Amaravadi, Eric H Baehrecke, Francesco Cecconi, Patrice Codogno, et al. 2015. “Autophagy in Malignant Transformation and Cancer Progression.” *The EMBO Journal* 34 (7): 856–80. http://emboj.embopress.org/content/34/7/856.abstract.
Ganley, Ian G., She Chen, Junru Wang, Xiaojun Ding, Du H. Lam, and Xuejun Jiang. 2009. “ULK1·ATG13·FIP200 Complex Mediates MTOR Signaling and Is Essential for Autophagy.” *Journal of Biological Chemistry* 284 (18): 12297–305. doi:10.1074/jbc.m900573200.
Geng, Jiefei, Usha Nair, Kyoko Yasumura-Yorimitsu, and Daniel J. Klionsky. 2010. “Post-Golgi Sec Proteins Are Required for Autophagy in Saccharomyces Cerevisiae.” *Molecular Biology of the Cell* 21: 2257–69. doi:10.1091/mbc.E09.
Geyer, Matthias, Oliver T Fackler, and B Matija Peterlin. 2001. “Structure – Function Relationships in HIV-1 Nef.” *EMBO Reports* 2 (7): 580–85. doi:10.1093/embo-reports/kve141.
Gillooly, David J, Isabel C Morrow, Margaret Lindsay, Robert Gould, Nia J Bryant, Jean-michel Gaullier, Robert G Parton, and Harald Stenmark. 2000.

"Gillooly et Al. - 2000 - Localization of PI (3) P in Yeast and Mammalian Cells" 19 (17): 4577–88.
Graef, Martin, Jonathan R Friedman, Christopher Graham, Mohan Babu, and Jodi Nunnari. 2013. "ER Exit Sites Are Physical and Functional Core Autophagosome Biogenesis Components." *Molecular Biology of the Cell* 24 (18): 2918–31. doi:10.1091/mbc.E13-07-0381.
Grzesiek, Stephan, Ad Bax, G Marius Clore, Angela M Gronenborn, Jin-shan Hu, Joshua Kaufman, Ira Palmer, Stephen J Stahl, and Paul T Wingfield. 1996. "SH3 Domain of Hck Tyrosine Protein Kinase" 3 (4): 2–7.
He, Congcong, Misuzu Baba, Yang Cao, and Daniel J Klionsky. 2008. "Self-Interaction Is Critical for Atg9 Transport and Function at the Phagophore Assembly Site during Autophagy" 19 (December): 5506–16. doi:10.1091/mbc.E08.
Heenan, Erin J., Janeen L. Vanhooke, Brenda R. Temple, Laurie Betts, John E. Sondek, and Henrik G. Dohlman. 2009. "Structure and Function of Vps15 in the Endosomal G Protein Signaling Pathway." *Biochemistry* 48 (27): 6390–6401. doi:10.1021/bi900621w.
Heike, Nora, Takeshi Kaizuka, Niklas Berleth, B Philip, Stefan Drießen, Fabian Stuhldreier, Nora Hieke, et al. 2015. "Expression of a ULK1 / 2 Binding-de Fi Cient ATG13 Variant Can Partially Restore Autophagic Activity in ATG13-de Fi Cient Cells," no. September: 1471–83.
Herman, P K, and S D Emr. 1990. "Characterization of VPS34, a Gene Required for Vacuolar Protein Sorting and Vacuole Segregation in Saccharomyces Cerevisiae." *Molecular and Cellular Biology* 10 (12): 6742–54. doi:10.1128/MCB.10.12.6742.Updated.
Hosokawa, Nao, Tominaga Hiroyuki, Maeda Hingo, Hayashi Makoto, Takeda Shu, Akira Shizuo, Komiya Setsuro, Nakamura Takashi, Akiyama Haruhiki, and Inamura Takeshi. 2008. "Nutrient-Dependent MTORC1 Association with the ULK1-Atg13-FIP200 Complex Required for Autophagy." *Molecular Biology of the Cell* 19 (12): 5373–86. doi:10.1091/mbc.E08.
Huang, Weijiao, Wooyoung Choi, Wanqiu Hu, Na Mi, Qiang Guo, Meisheng Ma, Mei Liu, et al. 2012. "Crystal Structure and Biochemical Analyses Reveal Beclin 1 as a Novel Membrane Binding Protein." *Cell Research* 22 (3): 473–89. doi:10.1038/cr.2012.24.
Hurley, J.H., and L.N. Young. 2017. *Mechanisms of Autophagy Initiation*. *Annual Review of Biochemistry*. Vol. 86. doi:10.1146/annurev-biochem-061516-044820.
Hurley, James H., and Brenda a. Schulman. 2014. "Atomistic Autophagy: The Structures of Cellular Self-Digestion." *Cell* 157 (2). Elsevier: 300–311. doi:10.1016/j.cell.2014.01.070.
Hurley, James H, and Dong Yang. 2008. "MIT Domainia." *Developmental Cell* 14 (1). Elsevier: 6–8. doi:10.1016/j.devcel.2007.12.013.
Ishihara, Naotada, Maho Hamasaki, Sadaki Yokota, Kuninori Suzuki, Yoshiaki Kamada, Akio Kihara, Tamotsu Yoshimori, Takeshi Noda, and Yoshinori Ohsumi. 2001. "Autophagosome Requires Specific Early Sec Proteins for Its Formation and NSF / SNARE for Vacuolar Fusion" 12 (November): 3690–

3702.
Itakura, Eisuke, Chieko Kishi, Kinji Inoue, and Noboru Mizushima. 2008. “Beclin 1 Forms Two Distinct Phosphatidylinositol 3-Kinase Complexes with Mammalian Atg14 and UVRag.” *Molecular Biology of the Cell* 19: 5360–72. doi:doi: 10.1091/mbc.E08-01-0080.
Jao, Christine C, Michael J Ragusa, Robin E Stanley, and James H Hurley. 2013. “A HORMA Domain in Atg13 Mediates PI 3-Kinase Recruitment in Autophagy.” *Proceedings of the National Academy of Sciences of the United States of America* 110 (14): 5486–91. doi:10.1073/pnas.1220306110.
Jin, Meiyan, and Daniel J. Klionsky. 2014. “Regulation of Autophagy: Modulation of the Size and Number of Autophagosomes.” *FEBS Letters* 588 (15). Federation of European Biochemical Societies: 2457–63. doi:10.1016/j.febslet.2014.06.015.
Joo, Joung Hyuck, Bo Wang, Elisa Frankel, Liang Ge, Lu Xu, Rekha Iyengar, XiuJie Li-Harms, et al. 2016. “The Noncanonical Role of ULK/ATG1 in ER-to-Golgi Trafficking Is Essential for Cellular Homeostasis.” *Molecular Cell* 62 (4): 491–506. doi:10.1016/j.molcel.2016.04.020.
Jung, Chang Hwa, Tominaga Hiroyuki, Maeda Hingo, Hayashi Makoto, Takeda Shu, Akira Shizuo, Chang Bong Jun, et al. 2008. “ULK1-Atg13-FIP200 Complexes Mediate MTOR Signaling to the Autophagy Machinery.” *Molecular Biology of the Cell* 19 (12): 5373–86. doi:10.1091/mbc.E08.
Kabeya, Yukiko, Noboru Mizushima, Akitsugu Yamamoto, Satsuki Oshitani-Okamoto, Yoshinori Ohsumi, and Tamotsu Yoshimori. 2004. “LC3, GABARAP and GATE16 Localize to Autophagosomal Membrane Depending on Form-II Formation.” *Journal of Cell Science* 117 (Pt 13): 2805–12. doi:10.1242/jcs.01131.
Kakuta, Soichiro, Hayashi Yamamoto, Lumi Negishi, Chika Kondo-Kakuta, Nobuhiro Hayashi, and Yoshinori Ohsumi. 2012. “Atg9 Vesicles Recruit Vesicle-Tethering Proteins Trs85 and Ypt1 to the Autophagosome Formation Site.” *The Journal of Biological Chemistry* 287 (53): 44261–69. doi:10.1074/jbc.M112.411454.
Kamada, Yoshiaki, Ken-ichi Yoshino, Chika Kondo, Tomoko Kawamata, Noriko Oshiro, Kazuyoshi Yonezawa, and Yoshinori Ohsumi. 2010. “Tor Directly Controls the Atg1 Kinase Complex to Regulate Autophagy.” *Molecular and Cellular Biology* 30 (4): 1049–58. doi:10.1128/MCB.01344-09.
Kamber, Roarke A., Christopher J. Shoemaker, and Vladimir Denic. 2015. “Receptor-Bound Targets of Selective Autophagy Use a Scaffold Protein to Activate the Atg1 Kinase.” *Molecular Cell* 59 (3). Elsevier Inc.: 372–81. doi:10.1016/j.molcel.2015.06.009.
Karanasios, Eleftherios, Eloise Stapleton, Maria Manifava, Takeshi Kaizuka, Noboru Mizushima, Simon a Walker, and Nicholas T Ktistakis. 2013. “Dynamic Association of the ULK1 Complex with Omegasomes during Autophagy Induction.” *Journal of Cell Science* 126 (Pt 22): 5224–38. doi:10.1242/jcs.132415.
Kihara, A, T Noda, N Ishihara, and Y Ohsumi. 2001. “Two Distinct Vps34 Phosphatidylinositol 3-Kinase Complexes Function in Autophagy and

Carboxypeptidase Y Sorting in Saccharomyces Cerevisiae." *The Journal of Cell Biology* 152 (3): 519–30. doi:10.1083/jcb.152.3.519.
Kim, Joungmok, Young Chul Kim, Chong Fang, Ryan C Russell, Jeong Hee Kim, Weiliang Fan, Rong Liu, Qing Zhong, and Kun-Liang Guan. 2013. "Differential Regulation of Distinct Vps34 Complexes by AMPK in Nutrient Stress and Autophagy." *Cell* 152 (1–2). Elsevier Inc.: 290–303. doi:10.1016/j.cell.2012.12.016.
Kim, Joungmok, Mondira Kundu, Benoit Viollet, and Kun Liang Guan. 2011. "AMPK and MTOR Regulate Autophagy through Direct Phosphorylation of Ulk1." *Nature Cell Biology* 13 (2). Nature Publishing Group: 132–41. doi:10.1038/ncb2152.
Kim, Young-Mi, Chang Hwa Jung, Minchul Seo, Eun Kyoung Kim, Ji-Man Park, Sun Sik Bae, and Do-Hyung Kim. 2015. "MTORC1 Phosphorylates UVRAG to Negatively Regulate Autophagosome and Endosome Maturation." *Molecular Cell* 57 (2). Elsevier Inc.: 207–18. doi:10.1016/j.molcel.2014.11.013.
Kirisako, Takayoshi, Yoshinobu Ichimura, Hisashi Okada, Yukiko Kabeya, Noboru Mizushima, Tamotsu Yoshimori, Mariko Ohsumi, Toshifumi Takao, Takeshi Noda, and Yoshinori Ohsumi. 2000. "The Reversible Modification Regulates the Membrane-Binding State of Apg8/Aut7 Essential for Autophagy and the Cytoplasm to Vacuole Targeting Pathway." *Journal of Cell Biology* 151 (2): 263–75. doi:10.1083/jcb.151.2.263.
Klionsky, Daniel J. 2007. "Autophagy: From Phenomenology to Molecular Understanding in Less than a Decade" 8 (November): 931–37. doi:10.1038/nrm2245.
Köfinger, Jürgen, Michael J. Ragusa, Il-Hyung Lee, Gerhard Hummer, and James H. Hurley. 2015. "Solution Structure of the Atg1 Complex: Implications for the Architecture of the Phagophore Assembly Site." *Structure* 23 (5). Elsevier: 809–18. doi:10.1016/j.str.2015.02.012.
Kofinger, Jurgen, Michael J. Ragusa, Il Hyung Lee, Gerhard Hummer, and James H. Hurley. 2014. "Solution Structure of the Atg1 Complex: Implications for the Architecture of the Phagophore Assembly Site." *Structure*, 809–18. doi:10.1016/j.str.2015.02.012.
Kraft, Claudine, Monika Kijanska, Eyal Kalie, Edyta Siergiejuk, Sung Sik Lee, Giuseppe Semplicio, Ingrid Stoffel, et al. 2012. "Binding of the Atg1/ULK1 Kinase to the Ubiquitin-like Protein Atg8 Regulates Autophagy." *The EMBO Journal* 31 (18). Nature Publishing Group: 3691–3703. doi:10.1038/emboj.2012.225.
Kyei, George B., Christina Dinkins, Alexander S. Davis, Esteban Roberts, Sudha B. Singh, Chunsheng Dong, Li Wu, et al. 2009. "Autophagy Pathway Intersects with HIV-1 Biosynthesis and Regulates Viral Yields in Macrophages." *Journal of Cell Biology* 186 (2): 255–68. doi:10.1083/jcb.200903070.
Lamb, Christopher a, Stefanie Nühlen, Delphine Judith, David Frith, Ambrosius P Snijders, Christian Behrends, and Sharon a Tooze. 2016. "TBC1D14 Regulates Autophagy via the TRAPP Complex and ATG9 Traffic." *The*

EMBO Journal 35 (3): 281–301. doi:10.15252/embj.201592695.
Lander, Gabriel C, Scott M Stagg, Neil R Voss, Anchi Cheng, Denis Fellmann, Craig Yoshioka, Christopher Irving, et al. 2009. “Image Processing.” *Access* 166 (1): 95–102. doi:10.1016/j.jsb.2009.01.002.Appion.
Lang, Thomas, Steffen Reiche, Michael Straub, Monika Bredschneider, and Michael Thumm. 2000. “Autophagy and the Cvt Pathway Both Depend on AUT9” 182 (8): 2125–33.
Lazarus, Michael B., Chris J. Novotny, and Kevan M. Shokat. 2015. “Structure of the Human Autophagy Initiating Kinase ULK1 in Complex with Potent Inhibitors.” *ACS Chemical Biology* 10 (1): 257–61. doi:10.1021/cb500835z.
Lemus, Leticia, Juan Luis Ribas, Leticia Lemus, Juan Luis Ribas, Natalia Sikorska, and Veit Goder. 2016. “An ER-Localized SNARE Protein Is Exported in Specific COPII Vesicles for Autophagosome Article An ER-Localized SNARE Protein Is Exported in Specific COPII Vesicles for Autophagosome Biogenesis.” *CellReports* 14 (7). The Authors: 1710–22. doi:10.1016/j.celrep.2016.01.047.
Levine, Beth, Rong Liu, Xiaonan Dong, and Qing Zhong. 2016. “Beclin Orthologs: Integrative Hubs of Cell Signaling, Membrane Trafficking, and Physiology.” *Trends in Cell Biology* 25 (9): 533–44. doi:10.1016/j.tcb.2015.05.004.
Li, Xiaohua, Liqiang He, Ka Hing Che, Sarah F Funderburk, Lifeng Pan, Nina Pan, and Mingjie Zhang. 2012. “Imperfect Interface of Beclin1 Coiled-Coil Domain Regulates Homodimer and Heterodimer Formation with Atg14L and UVRAG.” *Nature Communications* 3. Nature Publishing Group: 611–62. doi:10.1038/ncomms1648.
Liang, Chengyu, Pinghui Feng, Bonsu Ku, Iris Dotan, Dan Canaani, Byung-Ha Oh, and Jae U Jung. 2006. “Autophagic and Tumour Suppressor Activity of a Novel Beclin1-Binding Protein UVRAG.” *Nature Cell Biology* 8 (7): 688–99. doi:10.1038/ncb1426.
Liang, Chengyu, Jong-soo Lee, Kyung-soo Inn, Michaela U Gack, Qinglin Li, Esteban A Roberts, Isabelle Vergne, et al. 2008. “NIH Public Access” 10 (7): 776–87. doi:10.1038/ncb1740.Beclin1-binding.
Liang, Xiao Huan, Saadiya Jackson, Matthew Seaman, Kristy Brown, Bettina Kempkes, Hanina Hibshoosh, and Beth Levine. 1999. “Induction of Autophagy and Inhibition of Tumorigenesis by Beclin 1.” *Nature* 402 (6762): 672–76. doi:10.1038/45257.
Lim, Junghyun, M Lenard Lachenmayer, Shuai Wu, Wenchao Liu, and Mondira Kundu. 2015. “Proteotoxic Stress Induces Phosphorylation of P62 / SQSTM1 by ULK1 to Regulate Selective Autophagic Clearance of Protein Aggregates,” 1–28. doi:10.1371/journal.pgen.1004987.
Lin, Mary G., and James H. Hurley. 2016. “Structure and Function of the ULK1 Complex in Autophagy.” *Current Opinion in Cell Biology* 39: 61–68. doi:10.1016/j.ceb.2016.02.010.
Liu, Chin Chih, Yu Ching Lin, Yu Hsuan Chen, Chun Ming Chen, Liang Yu Pang, Hsuan An Chen, Pei Rung Wu, et al. 2016. “Cul3-KLHL20 Ubiquitin Ligase Governs the Turnover of ULK1 and VPS34 Complexes to Control Autophagy

Termination.” *Molecular Cell* 61 (1). Elsevier Ltd: 84–97. doi:10.1016/j.molcel.2015.11.001.
Lu, Jiahong, Liqiang He, Christian Behrends, Masatake Araki, Kimi Araki, Qing Jun Wang, Joseph M Catanzaro, et al. 2014. “NRBF2 Regulates Autophagy and Prevents Liver Injury by Modulating Atg14L-Linked Phosphatidylinositol-3 Kinase III Activity.” *Nature Communications* 5 (May). Nature Publishing Group: 3920. doi:10.1038/ncomms4920.
Lynch-Day, Molly A, Deepali Bhandari, Shekar Menon, Ju Huang, Huaqing Cai, Clinton R Bartholomew, John H Brumell, Susan Ferro-Novick, and Daniel J Klionsky. 2010. “Trs85 Directs a Ypt1 GEF, TRAPPIII, to the Phagophore to Promote Autophagy.” *Proceedings of the National Academy of Sciences of the United States of America* 107 (17): 7811–16. doi:10.1073/pnas.1000063107.
Ma, Xi, Shen Zhang, Long He, Yueguang Rong, Livia Wilz Brier, and Qiming Sun. 2017. “MTORC1-Mediated NRBF2 Phosphorylation Functions as a Switch for the Class III PtdIns3K and Autophagy” 8627 (February): 1–41. doi:10.1080/15548627.2016.1269988.
Mack, Hildegard I.D., Bin Zheng, John M. Asara, and Sheila M. Thomas. 2012. “AMPK-Dependent Phosphorylation of ULK1 Regulates ATG9 Localization.” *Autophagy* 8 (8): 1197–1214. doi:10.4161/auto.20586.
Mari, Muriel, Janice Griffith, Ester Rieter, Lakshmi Krishnappa, Daniel J Klionsky, and Fulvio Reggiori. 2010. “An Atg9-Containing Compartment That Functions in the Early Steps of Autophagosome Biogenesis” 190 (6): 1005–22. doi:10.1083/jcb.200912089.
Martinez, Jennifer, R. K. Subbarao Malireddi, Qun Lu, Larissa Dias Cunha, Stephane Pelletier, Sebastien Gingras, Robert Orchard, et al. 2015. “Molecular Characterization of LC3-Associated Phagocytosis Reveals Distinct Roles for Rubicon, NOX2 and Autophagy Proteins.” *Nature Cell Biology* 17 (7): 893–906. doi:10.1038/ncb3192.
Matsunaga, Kohichi, Eiji Morita, Tatsuya Saitoh, Shizuo Akira, Nicholas T Ktistakis, Tetsuro Izumi, Takeshi Noda, and Tamotsu Yoshimori. 2010. “Autophagy Requires Endoplasmic Reticulum Targeting of the PI3-Kinase Complex via Atg14L.” *The Journal of Cell Biology* 190 (4): 511–21. doi:10.1083/jcb.200911141.
Matsunaga, Kohichi, Tatsuya Saitoh, Keisuke Tabata, Hiroko Omori, Takashi Satoh, Naoki Kurotori, Ikuko Maejima, et al. 2009. “Two Beclin 1-Binding Proteins, Atg14L and Rubicon, Reciprocally Regulate Autophagy at Different Stages.” *Nature Cell Biology* 11 (4): 385–96. doi:10.1038/ncb1846.
McEwan, David G., Doris Popovic, Andrea Gubas, Seigo Terawaki, Hironori Suzuki, Daniela Stadel, Fraser P. Coxon, et al. 2015. “PLEKHM1 Regulates Autophagosome-Lysosome Fusion through HOPS Complex and LC3/GABARAP Proteins.” *Molecular Cell* 57 (1). Elsevier Inc.: 39–54. doi:10.1016/j.molcel.2014.11.006.
Mi, Na, Yang Chen, Shuai Wang, Mengran Chen, Mingkun Zhao, Guang Yang, Meisheng Ma, et al. 2015. “CapZ Regulates Autophagosomal Membrane Shaping by Promoting Actin Assembly inside the Isolation Membrane.”

Nature Cell Biology 17 (9): 1112–23. doi:10.1038/ncb3215.
Michel, Max, Melanie Schwarten, Luitgard Nagel-Steger, Dieter Willbold, Christina Decker, and Oliver H Weiergräber. 2015. “The Mammalian Autophagy Initiator Complex Contains 2 HORMA Domain Proteins.” *Autophagy* 11 (12): 2300–2308. doi:10.1080/15548627.2015.1076605.
Miller, Simon, Arkadiusz Oleksy, Olga Perisic, and Roger L Williams. 2010. “Shaping Development of Autophagy Inhibitors with the Structure of the Lipid Kinase Vps34.” *Autophagy* 6 (6): 805–7. doi:10.1126/science.1184429.
Miller, Simon, Brandon Tavshanjian, Arkadiusz Oleksy, Olga Perisic, Benjamin T Houseman, Kevan M Shokat, and Roger L Williams. 2010. “Shaping Development of Autophagy Inhibitors with the Structure of the Lipid Kinase Vps34.” *Science (New York, N.Y.)* 327 (5973): 1638–42. doi:10.1126/science.1184429.
Mindell, Joseph A., and Nikolaus Grigorieff. 2003. “Accurate Determination of Local Defocus and Specimen Tilt in Electron Microscopy.” *Journal of Structural Biology* 142 (3): 334–47. doi:10.1016/S1047-8477(03)00069-8.
Mizushima, Noboru, and Masaaki Komatsu. 2011. “Autophagy: Renovation of Cells and Tissues.” *Cell* 147 (4). Elsevier Inc.: 728–41. doi:10.1016/j.cell.2011.10.026.
Mizushima, Noboru, Beth Levine, Ana Maria Cuervo, and Daniel J Klionsky. 2008. “Autophagy Fights Disease through Cellular Self-Digestion.” *Nature* 451 (7182): 1069–75. doi:10.1038/nature06639.
Mizushima, Noboru, Tamotsu Yoshimori, and Yoshinori Ohsumi. 2011. “The Role of Atg Proteins in Autophagosome Formation.” *Annual Review of Cell and Developmental Biology* 27 (1): 107–32. doi:10.1146/annurev-cellbio-092910-154005.
Molday, R S, S W Englander, and R G Kallen. 1972. “Primary Structure Effects on Peptide Group Hydrogen Exchange.” *Biochemistry* 11 (2): 150–58. doi:10.1002/prot.340170110.
Nair, Usha, Anjali Jotwani, Jiefei Geng, Noor Gammoh, Diana Richerson, Wei Lien Yen, Janice Griffith, et al. 2011. “SNARE Proteins Are Required for Macroautophagy.” *Cell* 146 (2): 290–302. doi:10.1016/j.cell.2011.06.022.
Nixon, Ralph A. 2013. “The Role of Autophagy in Neurodegenerative Disease.” *Nature Medicine* 19 (8): 983–97. doi:10.1038/nm.3232.
Noda, Nobuo N., Takafumi Kobayashi, Wakana Adachi, Yuko Fujioka, Yoshinori Ohsumi, and Fuyuhiko Inagaki. 2012. “Structure of the Novel C-Terminal Domain of Vacuolar Protein Sorting 30/Autophagy-Related Protein 6 and Its Specific Role in Autophagy.” *Journal of Biological Chemistry* 287 (20): 16256–66. doi:10.1074/jbc.M112.348250.
Noda, Takeshi, John Kim, Wei-pang Huang, Misuzu Baba, Chikara Tokunaga, Yoshinori Ohsumi, and Daniel J Klionsky. 2000. “Apg9p / Cvt7p Is an Integral Membrane Protein Required for Transport Vesicle Formation in the Cvt and Autophagy Pathways” 148 (3): 465–79.
Obara, Keisuke, Takayuki Sekito, and Yoshinori Ohsumi. 2006. “Assortment of Phosphatidylinositol 3-Kinase Complexes — Atg14p Directs Association of Complex I to the Pre-Autophagosomal Structure in Saccharomyces

Cerevisiae" 17 (April): 1527–39. doi:10.1091/mbc.E05.
Oberstein, Adam, Philip D Jeffrey, and Yigong Shi. 2007. "Crystal Structure of the Bcl-XL-Beclin 1 Peptide Complex: Beclin 1 Is a Novel BH3-Only Protein." *The Journal of Biological Chemistry* 282 (17): 13123–32. doi:10.1074/jbc.M700492200.
Ogura, Toshihiko, Kenji Iwasaki, and Chikara Sato. 2003. "Topology Representing Network Enables Highly Accurate Classification of Protein Images Taken by Cryo Electron-Microscope without Masking." *Journal of Structural Biology* 143 (3): 185–200. doi:10.1016/j.jsb.2003.08.005.
Ohashi, Yohei, Nicolas Soler, Miguel García Ortegón, Lufei Zhang, Marie L. Kirsten, Olga Perisic, Glenn R. Masson, et al. 2016. "Characterization of Atg38 and NRBF2, a Fifth Subunit of the Autophagic Vps34/PIK3C3 Complex." *Autophagy* 8627 (September). Taylor & Francis: 00–00. doi:10.1080/15548627.2016.1226736.
Ohsumi, Yoshinori. 2000. "Kamada 2000, Tor-Mediated Induction of Autophagy via an Apg1 Protein Kinase Complex" 150 (6): 1507–13. doi:10.1083/jcb.150.6.1507.
Orsi, a, M Razi, H C Dooley, D Robinson, a E Weston, L M Collinson, and S a Tooze. 2012. "Dynamic and Transient Interactions of Atg9 with Autophagosomes, but Not Membrane Integration, Are Required for Autophagy." *Molecular Biology of the Cell* 23 (10): 1860–73. doi:10.1091/mbc.E11-09-0746.
Pantazatos, Dennis, Jack S Kim, Heath E Klock, Raymond C Stevens, Ian a Wilson, Scott a Lesley, and Virgil L Woods. 2004. "Rapid Refinement of Crystallographic Protein Construct Definition Employing Enhanced Hydrogen/Deuterium Exchange MS." *Proceedings of the National Academy of Sciences of the United States of America* 101 (3): 751–56. doi:10.1073/pnas.0307204101.
Papinski, Daniel, and Claudine Kraft. 2016. "Regulation of Autophagy by Signaling Through the Atg1/ULK1 Complex." *Journal of Molecular Biology* 428 (9). The Authors: 1725–41. doi:10.1016/j.jmb.2016.03.030.
Papinski, Daniel, Martina Schuschnig, Wolfgang Reiter, Larissa Wilhelm, Christopher a Barnes, Alessio Maiolica, Isabella Hansmann, et al. 2014. "Early Steps in Autophagy Depend on Direct Phosphorylation of Atg9 by the Atg1 Kinase." *Molecular Cell* 53 (3). The Authors: 471–83. doi:10.1016/j.molcel.2013.12.011.
Pattingre, Sophie, Amina Tassa, Xueping Qu, Rita Garuti, Huan Liang Xiao, Noboru Mizushima, Milton Packer, Michael D. Schneider, and Beth Levine. 2005. "Bcl-2 Antiapoptotic Proteins Inhibit Beclin 1-Dependent Autophagy." *Cell* 122 (6): 927–39. doi:10.1016/j.cell.2005.07.002.
Puri, Claudia, Maurizio Renna, Carla Figueira Bento, Kevin Moreau, and David C. Rubinsztein. 2014. "Diverse Autophagosome Membrane Sources Coalesce in Recycling Endosomes." *Autophagy* 10 (1). Elsevier: 182–84. doi:10.1016/j.cell.2013.08.044.
Qi, Shiqian, Do Jin Kim, Goran Stjepanovic, and James H. Hurley. 2015. "Structure of the Human Atg13-Atg101 HORMA Heterodimer: An Interaction

Hub within the ULK1 Complex." *Structure* 23 (10). Elsevier Ltd: 1848–57. doi:10.1016/j.str.2015.07.011.
Ragusa, Michael J, Robin E Stanley, and James H Hurley. 2012. "Architecture of the Atg17 Complex as a Scaffold for Autophagosome Biogenesis." *Cell* 151 (7). Elsevier Inc.: 1501–12. doi:10.1016/j.cell.2012.11.028.
Rao, Yijian, Marco G Perna, Benjamin Hofmann, Viola Beier, and Thomas Wollert. 2015. "The Atg1-Kinase Complex Tethers Atg9-Vesicles to Initiate Autophagy." *Nature Communications* 7. Nature Publishing Group: 1–13. doi:10.1038/ncomms10338.
Reggiori, F., and D. J. Klionsky. 2013. "Autophagic Processes in Yeast: Mechanism, Machinery and Regulation." *Genetics* 194 (2): 341–61. doi:10.1534/genetics.112.149013.
Reggiori, Fulvio, Katherine A. Tucker, Per E. Stromhaug, and Daniel J. Klionsky. 2004. "The Atg1-Atg13 Complex Regulates Atg9 and Atg23 Retrieval Transport from the Pre-Autophagosomal Structure." *Developmental Cell* 6 (1): 79–90. doi:10.1016/S1534-5807(03)00402-7.
Roseman, a. M. 2004. "FindEM - A Fast, Efficient Program for Automatic Selection of Particles from Electron Micrographs." *Journal of Structural Biology* 145 (1–2): 91–99. doi:10.1016/j.jsb.2003.11.007.
Rostislavleva, K., N. Soler, Y. Ohashi, L. Zhang, E. Pardon, J. E. Burke, G. R. Masson, et al. 2015. "Structure and Flexibility of the Endosomal Vps34 Complex Reveals the Basis of Its Function on Membranes." *Science* 350 (6257): aac7365-aac7365. doi:10.1126/science.aac7365.
Rui, Yan-Ning, Zhen Xu, Bindi Patel, Zhihua Chen, Dongsheng Chen, Antonio Tito, Gabriela David, et al. 2015. "Huntingtin Functions as a Scaffold for Selective Macroautophagy." *Nature Cell Biology* 17 (3): 262–75. doi:10.1038/ncb3101.
Russell, Ryan C, Ye Tian, Haixin Yuan, Hyun Woo Park, Yu-Yun Chang, Joungmok Kim, Haerin Kim, Thomas P Neufeld, Andrew Dillin, and Kun-Liang Guan. 2013. "ULK1 Induces Autophagy by Phosphorylating Beclin-1 and Activating VPS34 Lipid Kinase." *Nature Cell Biology* 15 (7). Nature Publishing Group: 741–50. doi:10.1038/ncb2757.
Sawa-Makarska, Justyna, Christine Abert, Julia Romanov, Bettina Zens, Iosune Ibiricu, and Sascha Martens. 2014. "Cargo Binding to Atg19 Unmasks Additional Atg8 Binding Sites to Mediate Membrane-Cargo Apposition during Selective Autophagy." *Nature Cell Biology* 16 (5): 425–33. doi:10.1038/ncb2935.
Sekito, Takayuki, Tomoko Kawamata, Rie Ichikawa, Kuninori Suzuki, and Yoshinori Ohsumi. 2009. "Atg17 Recruits Atg9 to Organize the Pre-Autophagosomal Structure." *Genes to Cells* 14 (5): 525–38. doi:10.1111/j.1365-2443.2009.01299.x.
Shaid, S, C H Brandts, H Serve, and I Dikic. 2013. "Ubiquitination and Selective Autophagy." *Cell Death and Differentiation* 20 (1): 21–30. doi:10.1038/cdd.2012.72.
Shang, L., S. Chen, F. Du, S. Li, L. Zhao, and X. Wang. 2011. "Nutrient Starvation Elicits an Acute Autophagic Response Mediated by Ulk1

Dephosphorylation and Its Subsequent Dissociation from AMPK." *Proceedings of the National Academy of Sciences* 108 (12): 4788–93. doi:10.1073/pnas.1100844108.
Shintani, Takahiro, Kuninori Suzuki, Yoshiaki Kamada, Takeshi Noda, and Yoshinori Ohsumi. 2002. "Apg2p Functions in Autophagosome Formation on the Perivacuolar Structure." *Journal of Biological Chemistry* 276 (32): 30452–60. doi:10.1074/jbc.m102346200.
Shirahama-Noda, Kanae, Shintaro Kira, Tamotsu Yoshimori, and Takeshi Noda. 2013. "TRAPPIII Is Responsible for Vesicular Transport from Early Endosomes to Golgi, Facilitating Atg9 Cycling in Autophagy." *Journal of Cell Science* 126 (Pt 21): 4963–73. doi:10.1242/jcs.131318.
Shoji-Kawata, Sanae, Rhea Sumpter, Matthew Leveno, Grant R. Campbell, Zhongju Zou, Lisa Kinch, Angela D. Wilkins, et al. 2013. "Identification of a Candidate Therapeutic Autophagy-Inducing Peptide." *Nature* 494 (7436). Nature Publishing Group: 201–6. doi:10.1038/nature11866.
Siddiqui, Waseem Ahmad, Amjid Ahad, and Haseeb Ahsan. 2015. "The Mystery of BCL2 Family: Bcl-2 Proteins and Apoptosis: An Update." *Archives of Toxicology* 89 (3): 289–317. doi:10.1007/s00204-014-1448-7.
Stack, J H, P K Herman, P V Schu, and S D Emr. 1993. "A Membrane-Associated Complex Containing the Vps15 Protein Kinase and the Vps34 PI 3-Kinase Is Essential for Protein Sorting to the Yeast Lysosome-like Vacuole." *The EMBO Journal* 12 (5): 2195–2204.
Stadel, Daniela, Valentina Millarte, Kerstin D. Tillmann, Jessica Huber, Bat Chen Tamin-Yecheskel, Masato Akutsu, Alik Demishtein, et al. 2015. "TECPR2 Cooperates with LC3C to Regulate COPII-Dependent ER Export." *Molecular Cell* 60 (1): 89–104. doi:10.1016/j.molcel.2015.09.010.
Stjepanovic, Goran, Sulochanadevi Baskaran, Mary G. Lin, and James H. Hurley. 2017. "Vps34 Kinase Domain Dynamics Regulate the Autophagic PI 3-Kinase Complex." *Molecular Cell* 67 (3). Elsevier Inc.: 528–534.e3. doi:10.1016/j.molcel.2017.07.003.
Stjepanovic, Goran, Christopher W. Davies, Robin E. Stanley, Michael J. Ragusa, Do Jin Kim, and James H. Hurley. 2014. "Assembly and Dynamics of the Autophagy-Initiating Atg1 Complex." *Pnas* 111 (35): 1407214111-. doi:10.1073/pnas.1407214111.
Suloway, Christian, James Pulokas, Denis Fellmann, Anchi Cheng, Francisco Guerra, Joel Quispe, Scott Stagg, Clinton S. Potter, and Bridget Carragher. 2005. "Automated Molecular Microscopy: The New Leginon System." *Journal of Structural Biology* 151 (1): 41–60. doi:10.1016/j.jsb.2005.03.010.
Sun, Qiming, Weiliang Fan, Keling Chen, Xiaojun Ding, She Chen, and Qing Zhong. 2008. "Identification of Barkor as a Mammalian Autophagy-Specific Factor for Beclin 1 and Class III Phosphatidylinositol 3-Kinase." *Proceedings of the National Academy of Sciences of the United States of America* 105 (49): 19211–16. doi:10.1073/pnas.0810452105.
Sun, Qiming, Wiebke Westphal, Kwun Ngok Wong, Irena Tan, and Qing Zhong. 2010. "Rubicon Controls Endosome Maturation as a Rab7 Effector." *Proceedings of the National Academy of Sciences of the United States of*

America 107 (45): 19338–43. doi:10.1073/pnas.1010554107.
Sun, Qiming, Jing Zhang, Weiliang Fan, Kwun Ngok Wong, Xiaojun Ding, She Chen, and Qing Zhong. 2011. “The RUN Domain of Rubicon Is Important for HVps34 Binding, Lipid Kinase Inhibition, and Autophagy Suppression.” *Journal of Biological Chemistry* 286 (1): 185–91. doi:10.1074/jbc.M110.126425.
Suzuki, Hironori, Takeshi Kaizuka, Noboru Mizushima, and Nobuo N Noda. 2015. “Structure of the Atg101-Atg13 Complex Reveals Essential Roles of Atg101 in Autophagy Initiation.” *Nature Structural & Molecular Biology* 22 (June): 1–11. doi:10.1038/nsmb.3036.
Suzuki, Hironori, Takuo Osawa, Yuko Fujioka, and Nobuo N Noda. 2017. “Structural Biology of the Core Autophagy Machinery.” *Current Opinion in Structural Biology* 43. The Author(s): 10–17. doi:10.1016/j.sbi.2016.09.010.
Suzuki, Kuninori, Takayoshi Kirisako, Yoshiaki Kamada, Noboru Mizushima, Takeshi Noda, and Yoshinori Ohsumi. 2001. “The Pre-Autophagosomal Structure Organized by Concerted Functions of APG Genes Is Essential for Autophagosome Formation.” *EMBO Journal* 20 (21): 5971–81. doi:10.1093/emboj/20.21.5971.
Suzuki, Kuninori, Yuka Kubota, Takayuki Sekito, and Yoshinori Ohsumi. 2007. “Hierarchy of Atg Proteins in Pre-Autophagosomal Structure Organization.” *Genes to Cells* 12 (2): 209–18. doi:10.1111/j.1365-2443.2007.01050.x.
Suzuki, Sho W., Hayashi Yamamoto, Yu Oikawa, Chika Kondo-Kakuta, Yayoi Kimura, Hisashi Hirano, and Yoshinori Ohsumi. 2015a. “Atg13 HORMA Domain Recruits Atg9 Vesicles during Autophagosome Formation.” *Proceedings of the National Academy of Sciences* 112 (11): 201421092. doi:10.1073/pnas.1421092112.
Tabata, Keisuke, Kohichi Matsunaga, Ayuko Sakane, Takuya Sasaki, Takeshi Noda, and Tamotsu Yoshimori. 2010. “Rubicon and PLEKHM1 Negatively Regulate the Endocytic/Autophagic Pathway via a Novel Rab7-Binding Domain.” *Molecular Biology of the Cell* 21 (24): 4325–37. doi:10.1091/mbc.E10.
Tan, Dongyan, Yiying Cai, Juan Wang, Jinzhong Zhang, Shekar Menon, and Hui-ting Chou. 2013. “The EM Structure of the TRAPPIII Complex Leads to the Identi Fi Cation of a Requirement for COPII Vesicles on the Macroautophagy Pathway,” 2–7. doi:10.1073/pnas.1316356110/-/DCSupplemental.www.pnas.org/cgi/doi/10.1073/pnas.1316356110.
Tang, Guang, Liwei Peng, Philip R. Baldwin, Deepinder S. Mann, Wen Jiang, Ian Rees, and Steven J. Ludtke. 2007. “EMAN2: An Extensible Image Processing Suite for Electron Microscopy.” *Journal of Structural Biology* 157 (1): 38–46. doi:10.1016/j.jsb.2006.05.009.
van Heel, M, G Harauz, E V Orlova, R Schmidt, and M Schatz. 1996. “A New Generation of the IMAGIC Image Processing System.” *Journal of Structural Biology* 116 (1): 17–24. doi:10.1006/jsbi.1996.0004.
Vanni, Stefano, Lydie Vamparys, Romain Gautier, Guillaume Drin, Catherine Etchebest, Patrick F J Fuchs, and Bruno Antonny. 2013. “Amphipathic Lipid Packing Sensor Motifs : Probing Bilayer Defects with Hydrophobic

Residues." *Biophysj* 104 (3). Biophysical Society: 575–84. doi:10.1016/j.bpj.2012.11.3837.
Wang, Chao Wen, John Kim, Wei Pang Huang, Hagai Abeliovich, Per E. Stromhaug, William A. Dunn, and Daniel J. Klionsky. 2001. "Apg2 Is a Novel Protein Required for the Cytoplasm to Vacuole Targeting, Autophagy, and Pexophagy Pathways." *Journal of Biological Chemistry* 276 (32): 30442–51. doi:10.1074/jbc.M102342200.
Wang, Juan, Saralin Davis, Shekar Menon, Jinzhong Zhang, Jingzhen Ding, Serena Cervantes, Elizabeth Miller, Yu Jiang, and Susan Ferro Novick. 2015. "Ypt1 / Rab1 Regulates Hrr25 / CK1 δ Kinase Activity in ER – Golgi Traffic and Macroautophagy" 210 (2): 273–85. doi:10.1083/jcb.201408075.
Wang, Juan, Shekar Menon, Akinori Yamasaki, Hui-Ting Chou, Thomas Walz, Yu Jiang, and Susan Ferro-Novick. 2013. "Ypt1 Recruits the Atg1 Kinase to the Preautophagosomal Structure." *Proceedings of the National Academy of Sciences of the United States of America* 110 (24): 9800–9805. doi:10.1073/pnas.1302337110.
Wang, Richard C., Yongjie Wei, Zhenyi An, Zhongju Zou, Guanghua Xiao, Govind Bhagat, Michael White, Julia Reichelt, and Beth Levine. 2012. "Akt-Mediated Regulation of Autophagy and Tumorigenesis through Beclin 1 Phosphorylation." *Science* 338 (6109): 956–59. doi:10.1126/science.1225967.
Webster, Christopher P, Emma F Smith, Claudia S Bauer, Annekathrin Moller, M Guillaume, Laura Ferraiuolo, Monika A Myszczynska, et al. 2016. "The C 9 Orf 72 Protein Interacts with Rab 1 a and the ULK 1 Complex to Regulate Initiation of Autophagy" 35 (15).
Wei, Yongjie, Zhenyi An, Zhongju Zou, Rhea Sumpter, Minfei Su, Xiao Zang, Sangita Sinha, Matthias Gaestel, and Beth Levine. 2015. "The Stress-Responsive Kinases MAPKAPK2/MAPKAPK3 Activate Starvation-Induced Autophagy through Beclin 1 Phosphorylation." *ELife* 4: 1–25. doi:10.7554/eLife.05289.
Wei, Yongjie, Zhongju Zou, Nils Becker, Matthew Anderson, Rhea Sumpter, Guanghua Xiao, Lisa Kinch, et al. 2013. "EGFR-Mediated Beclin 1 Phosphorylation in Autophagy Suppression, Tumor Progression, and Tumor Chemoresistance." *Cell* 154 (6). Elsevier: 1269–84. doi:10.1016/j.cell.2013.08.015.
Wen, Xin, and Daniel J. Klionsky. 2016. "An Overview of Macroautophagy in Yeast." *Journal of Molecular Biology* 428 (9). Elsevier Ltd: 1681–99. doi:10.1016/j.jmb.2016.02.021.
Wong, Pui-mun, Yan Feng, Junru Wang, Rong Shi, and Xuejun Jiang. 2015. "Regulation of Autophagy by Coordinated Action of MTORC1 and Protein Phosphatase 2A." *Nature Communications* 6. Nature Publishing Group: 1–11. doi:10.1038/ncomms9048.
Wu, Wenxian, Weili Tian, Zhe Hu, Guo Chen, Lei Huang, Wen Li, Xingli Zhang, et al. 2014. "ULK 1 Translocates to Mitochondria and Phosphorylates FUNDC1 to Regulate Mitophagy" 15 (5): 566–75.
Wurzer, Bettina, Gabriele Zaffagnini, Dorotea Fracchiolla, Eleonora Turco,

Christine Abert, Julia Romanov, and Sascha Martens. 2015. "Oligomerization of P62 Allows for Selection of Ubiquitinated Cargo and Isolation Membrane during Selective Autophagy." *ELife* 4 (September 2015): 1–28. doi:10.7554/eLife.08941.

Xu, Da-qian, Zheng Wang, Chen-Yao Wang, De-Yi Zhang, Hui-da Wan, Zi-long Zhao, Jin Gu, et al. 2016. "PAQR3 Controls Autophagy by Integrating AMPK Signaling to Enhance ATG14L-Associated PI3K Activity." *The EMBO Journal* 35 (5): 496–514. doi:10.15252/embj.201592864.

Yamamoto, Hayashi, Yuko Fujioka, Sho W. Suzuki, Daisuke Noshiro, Hironori Suzuki, Chika Kondo-Kakuta, Yayoi Kimura, et al. 2016. "The Intrinsically Disordered Protein Atg13 Mediates Supramolecular Assembly of Autophagy Initiation Complexes." *Developmental Cell* 38 (1). Elsevier Inc.: 86–99. doi:10.1016/j.devcel.2016.06.015.

Yamamoto, Hayashi, Soichiro Kakuta, Tomonobu M. Watanabe, Akira Kitamura, Takayuki Sekito, Chika Kondo-Kakuta, Rie Ichikawa, Masataka Kinjo, and Yoshinori Ohsumi. 2012a. "Atg9 Vesicles Are an Important Membrane Source during Early Steps of Autophagosome Formation." *Journal of Cell Biology* 198 (2): 219–33. doi:10.1083/jcb.201202061.

Yamamoto, Hayashi, Soichiro Kakuta, Tomonobu M Watanabe, Akira Kitamura, Takayuki Sekito, Chika Kondo-Kakuta, Rie Ichikawa, Masataka Kinjo, and Yoshinori Ohsumi. 2012b. "Atg9 Vesicles Are an Important Membrane Source during Early Steps of Autophagosome Formation." *The Journal of Cell Biology* 198 (2): 219–33. doi:10.1083/jcb.201202061.

Yeh, Yuh Ying, Kristie Wrasman, and Paul K. Herman. 2010. "Autophosphorylation within the Atg1 Activation Loop Is Required for Both Kinase Activity and the Induction of Autophagy in Saccharomyces Cerevisiae." *Genetics* 185 (3): 871–82. doi:10.1534/genetics.110.116566.

Yorimitsu, Tomohiro, and Daniel J. Klionsky. 2005. "Atg11 Links Cargo to the Vesicle-Forming Machinery in the Cytoplams to Vacuole Targeting Pathway." *Molecular Biology of the Cell* 16: 1593–1605. doi:10.1091/mbc.E04.

Young, Andrew R J, Edmond Y W Chan, Xiao Wen Hu, Robert Köchl, Samuel G Crawshaw, Stephen High, Dale W Hailey, Jennifer Lippincott-Schwartz, and Sharon a Tooze. 2006. "Starvation and ULK1-Dependent Cycling of Mammalian Atg9 between the TGN and Endosomes." *Journal of Cell Science* 119 (Pt 18): 3888–3900. doi:10.1242/jcs.03172.

Young, Lindsey N., Kelvin Cho, Rosalie Lawrence, Roberto Zoncu, and James H. Hurley. 2016. "Dynamics and Architecture of the NRBF2-Containing Phosphatidylinositol 3-Kinase Complex I of Autophagy." *Proceedings of the National Academy of Sciences*. doi:10.1073/pnas.1603650113.

Yuan, Hai-xin, Ryan C Russell, Kun-liang Guan, Hai-xin Yuan, Ryan C Russell, and Kun-liang Guan. 2013. "Nutrient Stress-Induced Autophagy Regulation of PIK3C3 / VPS34 Complexes by MTOR in Nutrient Stress-Induced Autophagy" 8627. doi:10.4161/auto.26058.

Zaffagnini, Gabriele, and Sascha Martens. 2016. "Mechanisms of Selective Autophagy." *Journal of Molecular Biology* 428 (9). The Authors: 1714–24.

doi:10.1016/j.jmb.2016.02.004.
Zalckvar, Einat, Hanna Berissi, Miriam Eisenstein, and Adi Kimchi. 2009. “Phosphorylation of Beclin 1 by DAP-Kinase Promotes Autophagy by Weakening Its Interactions with Bcl-2 and Bcl-XL.” *Autophagy* 5 (5): 720–22. doi:10.4161/auto.5.5.8625.
Zhong, Y., D. H. Morris, L. Jin, M. S. Patel, S. K. Karunakaran, Y.-J. Fu, E. a. Matuszak, H. L. Weiss, B. T. Chait, and Q.-J. Wang. 2014. “Nrbf2 Suppresses Autophagy by Modulating Atg14L-Containing Beclin 1-Vps34 Protein Complex Architecture and Reducing Intracellular Phosphatidylinositol-3 Phosphate Levels.” *Journal of Biological Chemistry* 289 (38): 3–8. doi:10.1074/jbc.M114.561134.
Zhong, Yun, Qing Jun Wang, Xianting Li, Ying Yan, Jonathan M. Backer, Brian T. Chait, Nathaniel Heintz, and Zhenyu Yue. 2009a. “Distinct Regulation of Autophagic Activity by Atg14L and Rubicon Associated with Beclin 1-Phosphatidylinositol-3-Kinase Complex.” *Nature Cell Biology* 11 (4): 468–76. doi:10.1038/ncb1854.
———. 2009b. “Distinct Regulation of Autophagic Activity by Atg14L and Rubicon Associated with Beclin 1–Phosphatidylinositol-3-Kinase Complex.” *Nature Cell Biology* 11 (4): 468–76. doi:10.1038/ncb1854.